

RADIOISOTOPE-POWERED SELF-RECIPROCATING CANTILEVER FOR MICRO POWER GENERATION

A Dissertation

Presented to the Faculty of the Graduate School

of Cornell University

in Partial Fulfillment of the Requirements for the Degree of

Doctor of Philosophy

by

Hui Li

August 2005

© 2005 Hui Li

ALL RIGHTS RESERVED

RADIOISOTOPE-POWERED SELF-RECIPROCATING CANTILEVER FOR MICRO POWER GENERATION

Hui Li, Ph.D.

Cornell University 2005

Micro electromechanical systems (MEMS) provide many devices in sub-millimeter size for sensing and actuation. However, the lack of size-compatible power supplies prohibits entire systems to be within the same scale. The same problem of battery scaling exists for micro electronic devices. Reported in this dissertation is a novel way of micro power generation with radioisotopes. Due to the high energy densities and long half-lives of selected radioisotopes, high energy density power sources with extremely long operation time are possible.

Conversion of direct charge collection to mechanical actuation is the main achievement. A cantilever with a conductive collector collects the emitted electrons from a Ni-63 beta source. Due to charge conservation, positive charges are left in the radioactive source. The resulting electrostatic force moves the cantilever toward the source. When the cantilever contacts the source, charges are neutralized and the spring force pulls the cantilever back to its initial position. This cycle repeats itself as long as the radioactive source is active. Therefore a self-reciprocating cantilever is realized. An electromechanical model is developed to characterize the cantilever and verified with experimental results. The factors that limit the energy conversion efficiency are discussed. Further, radio frequency (RF) pulse generation at the end of the reciprocation cycle is achieved using a dielec-

tric cantilever with metal electrodes, due to the excitation of dielectric waveguide mode. This RF pulse could be used for self-powered remote sensing and wireless communication. To generate electricity, a piezoelectric unimorph replaces the cantilever. At the end of the reciprocation, the sudden release of the unimorph excites its mechanical vibration, thereby generating electricity through the piezoelectric element.

The radioisotope-powered self-reciprocating cantilever provides a single platform for mechanical actuation, RF pulse generation and electrical power generation. Integration of all these functions holds great potential to enable self-powered autonomous systems.

BIOGRAPHICAL SKETCH

Hui Li was born in Jingshan, Hubei Province, China. He received his B.S. in physics from Tsinghua University, Beijing in 1997. He then received his M.A. in physics from Boston University in 1999. In the same year, he entered University of Wisconsin-Madison to pursue Ph.D. degree in electrical engineering. He got his M.S. in electrical engineering from University of Wisconsin-Madison in 2002 and transferred to Cornell University to continue his Ph.D. program.

To my parents
For all the love and support

ACKNOWLEDGEMENTS

I would like to express my sincere appreciation to my advisor, Professor Amit Lal. His creative ideas, patient guidance, continuous support and encouragement are essential to the completion of this work. His broad vision on the field of micro electromechanical systems and his enthusiasm toward research inspired me throughout all the years of my Ph.D. program.

I am grateful to Professor James Blanchard and Professor Douglass Henderson. Their expertise in engineering physics and their guidance are of great help to me. I am also grateful to Professor Rajit Manohar, Professor Michael Spencer and Prof. Edwin Kan for serving on my special committee and giving me helpful advices and inspiring suggestions.

I am grateful to many current and former colleagues for their friendship and indispensable help. I appreciate the discussion, working companion and collaboration with them. In particular, I would like to thank Il-Seok Son, Ville Kaajakari, Chung Hoon Lee, Hang Guo, Xi Chen, Yuqian Dong, Rajesh Duggirala, Shankar Radhakrishnan, Shyi-Herng Kan, Abhijit Sathaye and Serhan Ardanuc.

Mostly importantly I want to thank my parents and my brother for their endless love and support.

TABLE OF CONTENTS

1	Micro Power Generation	1
1.1	Lithium Batteries	1
1.2	Micro Fuel Cell	3
1.3	Micro Combustion Power Generation	6
1.4	Other Approaches	11
1.5	Why Radioisotopes?	12
2	Direct Charge Radioactive Power Generation	15
2.1	Radioactive decay	15
2.2	Nuclear Batteries	18
2.2.1	Direct Conversion Nuclear Battery	19
2.2.2	Junction-type Nuclear Battery	22
2.2.3	Contact-potential-difference Nuclear Battery	23
2.2.4	Double Conversion Nuclear Battery	25
2.3	Direct Conversion	26
3	The Self-Reciprocating Cantilever: Theory	27
3.1	Principle of Operation	27
3.2	Equivalent Circuit	29
3.3	Electromechanical Model	30
3.4	Operational Characteristics	33
3.5	Decay of the Radioisotope and Device Longevity	36
3.6	Radioisotope Selection	37
3.7	Summary	39
4	The Self-Reciprocating Cantilever: Experiment	41
4.1	Radioisotope Source	41
4.2	Cantilever	43
4.3	Setup	43
4.4	A Typical Distance versus Time Curve	44
4.5	Air-gap Capacitor Voltage	45
4.6	Mechanical and Electrical Energies	46
4.7	The Effect of Initial Distance	48
4.7.1	Normal Reciprocation	48
4.7.2	Pull-in	49
4.7.3	Air Breakdown	51
4.7.4	Cessation	52
4.7.5	Pseudo Continuous Reciprocation	53
4.8	Constant Current Approximation	54
4.9	Leakage Mechanisms	56
4.9.1	Radiation Configuration Factor	56
4.9.2	Secondary Electrons	57

4.9.3	Ionization	62
4.10	Efficiency and Energy Output	66
4.11	Scalability	69
4.12	Summary	71
5	Radio Frequency Pulse Generation	73
5.1	Radioactively Powered RF Pulse Generation: Theory	73
5.2	RF Pulse Generation: Experiment	76
5.3	Polymer Dielectric RF Pulse Generation	83
5.4	Summary	84
6	Radioactive Piezoelectric Micro Power Generation	85
6.1	Principle of Operation	85
6.2	Nuclear to Electrical Conversion Efficiency	87
6.3	Devices and Results	89
6.4	Summary	95
7	Conclusions	97
7.1	Self-reciprocating Cantilever	97
7.2	Future Research	98
A	Continuous-slowing-down Approximation Range	101
B	Radiation Configuration Factor for Two Parallel Rectangles	104
	Bibliography	107

LIST OF FIGURES

1.1	A comparison of energy densities of several battery technologies, some fuels and radioisotopes [29, 38].	12
2.1	Schematic of a direct conversion type nuclear battery. A radioisotope is one electrode. A collector collecting the charged particles from the radioisotope is the other electrode. The open circuit voltage can be very high due to the high energy carried by the charged particles.	21
2.2	Schematic of a junction type nuclear battery. Electron-hole pairs are generated as the charged particles enter the p-n junction. Under the influence of the depletion region a current is formed.	22
2.3	Schematic of a contact-potential-difference type nuclear battery. The two electrodes are made of different metals. The volume in between is some media irradiated by a radioisotope.	24
2.4	Schematic of a double conversion nuclear battery. Phosphor mixed with a radioisotope emits photons which are then converted into electricity by surrounding solar cells.	25
3.1	The self-reciprocation process with a beta source: (a) Electrons emitted from the radioisotope are collected by the anchored cantilever. Positive charges are left in the source because of charge conservation. (b) As more and more charges get collected, the electrostatic force becomes larger and pulls the cantilever toward the radioisotope. (c) Eventually the cantilever gets in contact with the source. Charges are neutralized through charge transfer. (d) The electrostatic force becomes almost zero as most of the charges are neutralized. The spring force of the cantilever retracts it back to its initial position and a new cycle begins.	28
3.2	Equivalent circuit of the self-reciprocating cantilever. The distance between the cantilever and the radioisotope is exaggerated. The emitted charges can be modeled as a current source. The resistor R represents leakage paths. The cantilever and the radioisotope form the capacitor C.	29
4.1	The experimental setup for measuring the current from the source is shown. Drawing is not to scale. The vacuum chamber is much larger than the source. The source is connected to a source-measurement unit of a Keithley 4200 semiconductor analyzer. The chamber is connected to the ground unit.	42
4.2	The experimental setup: a copper cantilever ($5\text{ cm} \times 5\text{ mm} \times 60\text{ }\mu\text{m}$) is placed at a controlled distance away from a $1\text{ mCi } ^{63}\text{Ni}$ ($4\text{ mm} \times 4\text{ mm}$) thin film source electroplated on a 1 mm thick aluminum plate.	44

4.3	Measured and calculated distance versus time curves for the sample cantilever actuated by the ^{63}Ni source. The initial gap is $118\ \mu\text{m}$. .	45
4.4	The calculated voltage across the cantilever and the radioisotope is plotted against the distance in between. The maximum voltage is $46\ \text{V}$	46
4.5	Energies stored in the cantilever are plotted against time with an initial gap of $118\ \mu\text{m}$ for the sample cantilever.	47
4.6	Measured and calculated reciprocation periods for the sample cantilever with different initial gaps.	49
4.7	The distance versus time curve is plotted for an initial gap of $1\ \text{mm}$ where pull-in happens.	50
4.8	The reciprocation period versus the initial gap and the pull-in deflection are plotted.	51
4.9	The elapsed time when air breakdown happens and the corresponding normalized deflection are plotted versus the initial gap.	52
4.10	The estimated breakdown voltage and corresponding electric field are plotted against the initial gap.	53
4.11	Shown is the the normalized pull-in deflection versus the initial gap.	55
4.12	On the left it illustrates the solid angle coverage decreases as the gap increases. On the right, it illustrates the calculation of radiation configuration factor.	57
4.13	The measured collector current under zero-bias condition is plotted together with the calculated value which takes into account only the radiation configuration factor.	58
4.14	The calculated collector current with the consideration of secondary electrons is plotted to compare with the measured value.	59
4.15	The collector current of collectors made of different metals but with the same size is measured.	61
4.16	Collection efficiency normalized against that of Cu is plotted versus atomic number.	61
4.17	The collector current under zero bias or $-5\ \text{V}$ is measured versus pressure at two locations.	63
4.18	Shown is the collector current versus bias voltage. Measurements are taken at two different gaps.	64
4.19	The total electron ionization cross sections of N_2 and O_2 are plotted. Data are from Reference [54].	65
4.20	The energy conversion efficiency and the current collection efficiency are plotted against initial gap.	67
4.21	Shown is a picture of a Si_3N_4 micro cantilever. Its dimensions are $500\ \mu\text{m} \times 300\ \mu\text{m} \times 1.7\ \mu\text{m}$. At the tip area of the cantilever a layer of $1\ \mu\text{m}$ Al is evaporated. Four polysilicon resistors form a Wheatstone bridge on the cantilever for monitoring the deflection. The measurement circuit is shown on the right side.	71

4.22	The distance versus time curve of the micro cantilever is shown. The deflection was measured by both the optical method and the output from the polysilicon resistors.	72
5.1	(a) The capacitance of the PZT cantilever builds up an electric field as the charges are built on the two electrodes. (b) The sudden shorting of the charge on one side results in a sudden release of the electric field and hence the voltage across the cantilever. This results in a displacement current that excites the dielectric RF mode of the PZT.	74
5.2	The PZT cantilever is connected to an oscilloscope for RF pulse detection with a coaxial cable.	75
5.3	The experimental setup for detecting the RF pulse generated by a radioisotope-powered PZT cantilever is shown.	76
5.4	The RF pulse obtained with a 2 feet long cable is shown. The closeup shows the initial pulse.	77
5.5	Shown is the frequency spectrum of the pulse in Figure 5.4. There are two frequency components, one is at 32.5 MHz , the other one is at 127.5 MHz	77
5.6	The pulse frequency varies as the cable length changes.	78
5.7	Shown is the setup to measured the resonance frequency of the system composed of the PZT cantilever, the coaxial cable and a capacitor which simulates the oscilloscope.	79
5.8	The resonance frequency of the system changes with the cable length, which is indicated by L	80
5.9	The oscillation frequency of the RF pulse also varies as the coaxial cable length changes.	80
5.10	The experimental setup for remotely detecting the RF pulse is shown. A small coil (8 turns, $\phi\ 1\text{ mm}$, 70 nH) is soldered to the PZT cantilever as an antenna. Another coil (100 turns, $\phi\ 6\text{ mm}$, $25\ \mu\text{H}$) is connected to the oscilloscope for detection.	81
5.11	A typical RF pulse remotely detected is shown. The signal frequency is 117.5 MHz and the peak-to-peak voltage is 59 mV	82
5.12	A typical RF pulse generated by the ethyl cyanoacrylate cantilever. The initial pulse frequency is 133 MHz and the peak-to-peak voltage is 6.9 V	83
5.13	The frequency of the RF pulse generated with the ethyl cyanoacrylate cantilever also varies with the coaxial cable length.	84
6.1	A schematic of the PZT unimorph driven by a radioisotope is shown. The two electrodes of the PZT piece are connected to an oscilloscope to measure the output.	86
6.2	The circuit configuration for the characterization of the micro power generator.	86

6.3	A picture of the experimental setup is shown. The cantilever is clamped by two ceramic pieces. The Ni-63 source is mounted on a linear stage for initial gap control. Two wires soldered to the PZT piece provide electrical connection for signal detection. The whole setup is put inside a vacuum chamber with a glass top. A microscope connected to a CCD camera is placed outside the chamber to monitor the device movement.	90
6.4	Measured output waveform of the micro power generator across $1\text{ M}\Omega$ resistive load is plotted. A closeup at 2 s shows the sinusoidal nature of the AC signal. The maximum peak-to-peak voltage is 3.4 V and the signal frequency is 19.6 Hz	91
6.5	The reciprocation period varies as the initial gap changes. The curve is fitted with the electromechanical model. When the initial gap becomes larger than 2 mm air breakdown happens.	92
6.6	The quality factor and the electrical energy output for different load resistances with the same cantilever at a fixed initial gap of 1 mm are plotted. As expected, the optimum load resistance is $1\text{ M}\Omega$. . .	93
6.7	As the initial gap increases, both the extracted electrical energy and the total energy conversion efficiency increase.	94
B.1	Shown is the configuration of two parallel rectangles.	104
B.2	Shown is the configuration of two coaxial parallel squares.	105
B.3	Shown is the configuration of two identical rectangles directly opposing to each other.	106

LIST OF TABLES

1.1	Specific powers of some radioisotopes, calculated based on the data from Ref. [38].	13
2.1	Listed are different ways of converting kinetic energy from radioisotopes into electricity.	20
3.1	Listed are some pure beta emitting radioisotope candidates. The first three columns are obtained from [38], while the activity density is derived from the specific activity. The ranges in Cu and Si are estimated for the emitted electrons with the maximum energy [49].	39
4.1	Experimental parameters	45
4.2	Some characteristics of the cantilever with an initial distance of $118\ \mu m$	48
4.3	Three cantilevers made of different materials but with same width and stiffness are compared at different initial gaps. Shown are the reciprocation periods.	62
4.4	The design parameters for better performance are listed. \uparrow means increase, \downarrow means decrease and - means irrelevant.	69
6.1	Summary of the test results of the large and the small devices. The large device offers better performance.	95
6.2	List is the comparison of two devices whose only difference is the mass of the collector. The initial distance is $3\ mm$. The one with a heavier collector has a lower resonance frequency and a higher efficiency.	95

Chapter 1

Micro Power Generation

Microelectromechanical systems (MEMS) have made great strides during last twenty years. Many devices are available for a variety of sensing and actuation functions. Although the size of MEMS devices is in sub-millimeter range, the power supplies for the devices do not scale accordingly. This same problem of battery scaling exists for micro electronic devices. Current chemical reaction based battery technology can not meet the requirements of compact size and high energy density. There exists great interest in finding alternative small size power supplies.

1.1 Lithium Batteries

Among all the battery technologies, such as lead-acid, zinc/air and alkaline batteries, lithium batteries currently offer the best performance in energy density (Wh/g). The state-of-the-art technology offers 590 Wh/kg (2.1 kJ/g) for non-rechargeable batteries ($Li/SOCl_2$ type) and 150 Wh/kg (0.54 kJ/g) for rechargeable Li-ion batteries [1]. Recently due to the reduction in size and power requirement of electronic devices, researchers have investigated thin film lithium batteries [2, 3, 4]. Thin film lithium batteries use thin film anode, electrolyte and cathode with a total thickness in the range of a few tens of micrometers [2]. The performance of thin film lithium batteries are area dependent since the current output depends on the area of the thin film. The energy density is about 1 mWh/cm^2 (3.6 J/cm^2) [2]. The power density is around 0.5 mW/cm^2 [3] and can be up to 30 mW/cm^2 with reduced maximum usable capacity of the battery [4, 5]. Research on materials for anode, cathode and electrolyte is still un-

dergoing to obtain higher capacity, higher output power and more recharge cycles. Better coatings or sealing of the battery to avoid lithium reacting with air is also necessary [5].

The theoretical energy density is 1471 Wh/kg for Li/SOCl_2 batteries and 410 Wh/kg for Li-ion batteries. Battery technology thus has its ultimate limitation. Because of the weight of the construction material, the practical energy density is much lower, which could be 50% less. Furthermore, the actual energy delivered by a practical battery, even under optimum discharge conditions, may only be 50 to 75 percent of the practical value [1]. “The upper limit is now being reached as most of the materials that are practical for use as active materials in batteries have already been investigated and the list of unexplored materials is being depleted” [1]. The scaling down in size and cost of micro electronics has far outpaced the scaling of the energy densities of batteries. To power portable devices and sensor nodes as long as possible, even larger energy density is desired [6, 7]. Furthermore, the power density of lithium batteries cannot catch up with the requirement of power intensive applications such as portable computing. Another limitation of lithium batteries is their working temperature range, for lithium-ion battery it is from -40°C to 65°C [1]. Therefore they are not appropriate for the applications where operation temperature is outside this range.

New micro power generation technologies which explore the high energy density of hydrogen which is 142 kJ/g [8], and hydrocarbon fuels, for example, 20 kJ/g of methanol [9], are undergoing. One major incentive of these research efforts is that due to the high energy density of the fuels, even at relatively low conversion efficiency, higher energy density and/or power density micro power sources are possible compared to battery technologies. Furthermore, micro processing technology

is used from the beginning to fabricate those micro power generation devices, which offers natural integration with micro electronics and MEMS devices.

1.2 Micro Fuel Cell

A fuel cell is an electrochemical device that converts the chemical energy of a fuel (hydrogen, methanol, gasoline, etc.) and an oxidant (air or oxygen) directly into electricity. The most common classification of fuel cells is by the type of electrolyte used in the cells and includes: 1. polymer electrolyte fuel cell, 2. alkaline fuel cell, 3. phosphoric acid fuel cell, 4. molten carbonate fuel cell, and 5. solid oxide fuel cell [8]. Micro fuel cells have been under extensive research recently [10, 11, 12] and two types of micro fuel cells have most of the attention: one is polymer electrolyte membrane fuel cell (PEMFC); the other one is direct methanol fuel cell (DMFC), which also uses polymer electrolyte.

PEMFCs use proton-conducting polymer membranes as electrolyte and hydrogen as fuel. Because of the solid state of polymer membranes, it offers the advantages of easy fabrication, easy integration with other components, no need to handle sealing or liquids, which including corrosive acids or bases. The operation principle is as following: hydrogen is oxidized at the anode, usually with the help of catalysts, to produce protons and electrons; the electrons are forced through the external circuit (the load) and the protons are transferred to the cathode through the electrolyte; oxygen is introduced to the cathode to react with the protons and the electrons coming back from the external circuit to form water.

Due to the potential energy barriers of the chemical reaction, a single cell of PEMFC offers a open-circuit voltage less than 1 V. Therefore, usually a series connection of cells is needed to achieve the desired working voltage. The micro

fuel cell reported by J. Wainright et. al, consisting of six cells with dimensions of $2.7 \times 1.8 \times 0.2 \text{ cm}^3$, had a output voltage of 3 V with maximum continuous power in the range of $3 \sim 15 \text{ mW}$ and peak power of $50 \sim 100 \text{ mW}$ under 10 ms pulse, depending on the relative humidity [12]. R. Hahn reported their micro fuel cell with a stable power output of 80 mW/cm^2 , where a single cell occupied an active area of 0.54 cm^2 [13]. Hydrogen storage is a challenge for micro PEMFCs. J. Wainright et. al tried to solve this by hydrogen generation via decomposition of sodium borohydride solutions and hydrogen storage using metal hydrides. Promising results were presented and further improvement was expected. An alternative way to provide hydrogen to the fuel cell is to use a reactor, also called reformer, to generate hydrogen from hydrocarbon fuels, such as methanol, with the help of catalysts [9, 10].

To avoid hydrogen storage problem, DMFCs are developed. DMFCs also use polymer membrane as electrolyte but they can directly use methanol as fuel without converting to hydrogen first. Methanol is fed into the anode where it reacts with water, under the help of certain catalysts, to produce electrons, protons and carbon dioxide. The electrons flow through an external circuit while the protons migrate through the polymer membrane electrolyte to the cathode. At the cathode, oxygen, the protons and the electrons coming back from the external circuit combine to form water. Open circuit voltage of a single cell is about 1 V so that stacking of multiple cells is necessary for practical applications. T. J. Yen et. al reported a micro DMFC with an effective cell area of 1.625 cm^2 that produced a maximum output power density of 47.2 mW/cm^2 at $60 \text{ }^\circ\text{C}$ and 14.3 mW/cm^2 at room temperature [11]. The micro DMFC reported by A. Blum et al. produced a maximum power density of 12.5 mW/cm^2 with an area of 6 cm^2 [14].

Other types of micro fuel cells have also been developed. The micro PEMFC fuel cells made by C. Rice et al. used formic acid as fuel and achieved 48.8 mW/cm^2 power output at $60 \text{ }^\circ\text{C}$ [15]. X. Chen et al. reported a micro solid oxide fuel cell that used Sm-doped CeO_2 thin film as electrolyte layer with a porous Ni anode and a $\text{La}_{0.5}\text{Sr}_{0.5}\text{CoO}_3$ thin film cathode [16]. It was operated using hydrogen as fuel over a temperature range of 480 to $570 \text{ }^\circ\text{C}$ with a maximum power density of about 110 mW/cm^2 at $570 \text{ }^\circ\text{C}$.

Although research on micro fuel cells has made significant achievements, many challenges exist, and improvements are needed [8]. The polymer membranes currently used are expensive. The thickness range and the ionic conductivity of the membranes are limited. Low resistivity membranes are needed, especially for high current density operation. Thinner membranes to improve power density, and lower cost can help to promote the use of micro fuel cells. Electrode performance also needs improvement for higher power output by increasing the efficiency of electrode chemical reactions. To help the electrochemical reactions, catalysts, usually Pt based, are commonly used on the electrodes, which can increase the fuel-cell cost. Low tolerance for carbon monoxide due to catalyst poisoning requires purification of hydrogen, particularly for those where fuel reformer is used. Catalysts with high tolerance for carbon monoxide and other impurities are under investigation. Research has also been done to improve electrode structure for higher current density with MEMS technology. Local heat dissipation can limit the performance for fuel cells which is more problematic for cell stacks. Water byproduct management is important for fuel cell operation, because high water content in the electrolyte is required for high ionic conductivity. The reported fuel cell performances as mentioned above varied with humidity. In extreme case a dry

proton-conducting membrane, after long time storage period, may render the fuel cell useless. For DMFCs, methanol cross-over, which means methanol crosses over the membrane from the anode to the cathode, is an issue because methanol can drastically poison the catalysts, and methanol also directly reacts with oxygen at the cathode resulting in fuel wastage.

Micro fuel cells are still under development. Many devices have been designed, fabricated and tested. Promising results are presented. However, reliability and life time test are rarely seen, and fuel storage is seldom discussed. Performance still needs improvement for targeted applications.

1.3 Micro Combustion Power Generation

Micro combustion generates heat that can be used to generate electrical and mechanical power. The main idea is to scale down a macro size combustor to millimeter or sub-millimeter scale, to burn hydrogen or hydrocarbon fuels.

The micro gas turbine engine reported by A. Epstein et al. is one of the most famous micro combustion engines [17]. The turbine is based on silicon and uses hydrogen or hydrocarbon fuels. The targeted performance is $10 \sim 50 \text{ W}$ with a volume less than 1 cm^3 and a consumption of 7 g of fuel per hour. A six-wafer combustion system has been developed for this micro engine [18]. The system achieved combustion efficiency over 90% and power density up to 1100 W/cm^3 with premixed hydrogen-air, and these numbers became 60% and 500 W/cm^3 with ethylene. Like its larger counterparts, the micro gas turbine outputs mechanical rotation and can be connected to an electric generator for electricity. The micro turbine has not yet been realized. However, cold devices (room temperature) have rotated at greater than 1 MRPM [19].

K. Fu et al. developed a small-scale rotary (Wankel type) engine [20]. The Wankel type is chosen because most of the components is planar, natural for MEMS fabrication. Also the rotor automatically controls the timing of intake and exhaust, eliminating the need for complex valve control system. Output from this engine is again mechanical rotation. A working prototype rotary engine was made of steel using electron discharge machining. Operating with hydrogen-air mixture as fuel, a electrical power output of 2.7 *Watts* was achieved with a displacement of about 350 mm^3 . Individual components of a silicon-based MEMS rotary engine were also fabricated [20, 21]. *SiC* coating on silicon parts were deposited on the locations where high temperature would be experienced by the engine. An electric generator will be integrated into the micro engine as the rotor also served as the generator rotor. The proposed goal is to generate 10 ~ 100 *mW* electrical power with the MEMS rotary engine [21].

Another approach was taken by T. Toriyama et al. where a resonant micro reciprocation engine was designed [22]. The micro engine has a pair of opposite-pistons supported by elastic springs that are reciprocated in resonance mode by receiving an impact force due to combustion in the chamber between the pistons. The pistons are connected to an electrical generator for electric power output. Hydrogen is the proposed fuel and a power of 40 *mW* is projected.

Instead of driving an electrical generator for electricity, the “ P^3 micro heat engine” developed by S. Whalen et al. uses piezoelectric effect for electrical power generation [23]. The micro engine consists of a cavity filled with a saturated, two-phase working fluid, with both top and bottom sealed by thin membranes. The top membrane has a thin film piezoelectric layer. Electricity is generated when the piezoelectric membrane is strained during the expansion of the working fluid when

the heat is conducted into the engine. The design of this engine focused on the membranes, not the combustor. Therefore, the P^3 engine could be used to take advantage of other temperature gradients. The engine was tested with a resistive heater that provided a power of 1.45 W , and it generated a peak output power of $0.8\text{ }\mu\text{W}$ with a load resistance of $14\text{ k}\Omega$.

The above engines all involve mechanical motion that requires moving parts to convert heat into electricity. Research has also been done on approaches that do not require moving parts to convert thermal energy into electricity. Both S. Schaevitz et al. [24] and C. Zhang et al. [25] reported combustion-thermoelectric power generators. The generators utilized thermopiles to convert the thermal energy from combustion to electricity and both put the thermopiles on membranes to minimize undesired thermal conduction. Schaevitz's device used a Si-Ge thermopile, and tests were done with combustion of hydrogen, ammonia and butane. The device was stable at temperatures up to $500\text{ }^\circ\text{C}$ with an output of about $75\text{ }\mu\text{W}$ at thermal efficiency of 0.02% . Zhang's device utilized a polysilicon-Pt thermopile and combustion test was done with hydrogen. The achieved power was about $1\text{ }\mu\text{W}/\text{thermocouple}$. C. Zhang et al. also reported a micro combustion based thermionic power generator [26]. In this design, an emitter made of BaO absorbs heat from the combustion chamber underneath to emit electrons that are collected by a collector positioned $10\text{ }\mu\text{m}$ away, and current is realized by connecting the emitter and the collector with a load. By using an on-chip resistive heater, the device generated a voltage in the range of $0.4 \sim 5.6\text{ mV}$ and $7 \sim 160\text{ }\mu\text{A}$ current across a $46.7\text{ }\Omega$ load, resulting in an efficiency less than 10^{-6} with a power level of about $1\text{ }\mu\text{W}$. Although combustion was demonstrated with the device, power generation by combustion was not achieved due to the complexity of the system.

The difficulty lied in the maintenance of good vacuum under high operating temperature which was required to make and keep the emitter active.

Thermophotovoltaic effect has been explored by W. M. Yang et al. for micro combustion power generation [27, 28]. Thermophotovoltaic devices use photovoltaic cells to convert heat radiation into electricity. The main components of Yang's device include a heat source, an emitter, a filter and a photovoltaic cell array. A cylindrical SiC combustor serves as the heat source and the emitter. The combustor is designed to keep an balance between maximizing heat radiation and sustaining stable combustion. SiC is used due to its high emissivity and capability to endure high temperature. The SiC emitter is a broadband emitter that, under the working temperature, has a significant proportion of low energy photons not able to generate charge carriers in the photovoltaic cells. To improve the overall efficiency, a dielectric filter made by alternating layers of silicon and silicon dioxide is used to reflect part of those photons back to the emitter and transmit the desired photons to the photovoltaic cells. Low band gap semiconductors are needed for themophotovoltaic energy conversion. GaSb, GaInAs and InGaAsSb are typical low band gap photovoltaic cell materials. Corresponding to the filter, a GaSb photovoltaic cell array with six cells is used. The test result showed an electrical power output of 1.02 W with a micro combustor of 0.113 cm^3 in volume when the hydrogen flow rate was 4.20 g/h and the H_2/air ratio was 0.9. The corresponding open circuit voltage, and short circuit current were 2.28 V and 0.59 A , respectively.

Significant research has been done in micro combustion power generation. However, most devices demonstrated are in the proof-of-concept stage. Challenges in micro-fluidics, chemical reactions at small scale, materials selection, fabrication of high-aspect-ratio structures and complex geometries, and assembly remain [29, 30].

Improving the performance of micro combustors attracts most research efforts. Small scale devices limit the time available for combustion reaction and quenching of the combustion by the wall of the device is possible. Therefore a small chemical reaction time is desired, which can be obtained by ensuring high combustion temperature, using stoichiometric mixtures, using high energetic fuels and employing catalytic combustion. This explains why lots of the reported devices use hydrogen as fuel, which may be a potential problem for real applications because of fuel storage. Also fuel pre-mixing is very important as inadequate mixing leads to low combustion efficiency. However pre-mixing requires time and extra processing volume, especially for liquid fuels. The surface-to-volume ratio increases as device size scales down, increasing the heat loss through the walls of combustors. Large surface heat loss not only lowers the combustor efficiency but also increases the chemical reaction time and narrows flammability limits by lowering reaction temperature. Due to the high temperature, around $1000\text{ }^{\circ}\text{C}$, involved, material constraints need to be considered. For silicon based system, 950 K is the wall temperature limit above which silicon begins to soften and lose its structural integrity [30]. For moving components an even lower temperature, below 900 K , is desired because of thermo-mechanical creep consideration. Other materials, such as SiC , Si_3N_4 and diamond can withstand higher temperature so that they may be more suitable for micro combustors.

For micro engines involving movable components, mechanical-wear is a serious challenge. The micro rotary engine also needs to solve the problem of leakage between the rotor apex tip seals and the housing, and over the rotor faces, which results in low compression ratio, and hence, low efficiency. Another important fact is that these micro combustion engines require complex fabrication process and

hand assembly which can result in low device yield.

1.4 Other Approaches

In addition to micro fuel cells and micro combustion power generation, other approaches also exist for micro power generation. Solar cell based light harvesting is one choice although this technology has been developed for a long time. In the “Smart Dust” project that attempted to create completely autonomous sensing and communication platforms in a cubic millimeter volume, solar cells were used for the power supply [31]. The advantages of solar cell are that no fuel is needed and the conversion efficiency is relatively high (can be up to 30% [32]). The obvious disadvantage is its operation depends on the availability and intensity of light. Another disadvantage is that the power out is area dependant, which is a potential limit for miniaturization. Furthermore, unit cell open circuit voltage is limited such that series connected multiple cells are generally necessary for applications.

Scavenging environmental vibrational energy for micro power generation is also under research where different ways of converting vibrational energy into electricity are explored [33, 34, 35, 36]. Electromagnet transduction is one method, where a cantilever or diaphragm assembled with magnets vibrates and nearby coils generate electrical output. Electrostatic generator is another way. It consists of an electrode on a cantilever or other movable structure facing the other electrode, which is fixed and has an electret, across a small gap or vise versa. The electret holds charges quasi-permanently so that the electrode on the cantilever has induction charges and generates output voltage when it moves. Piezoelectric effect is also used where a piezoelectric material converts the strain generated by vibrations into electricity. Although these approaches are appealing, currently the power lever is only in

nanowatts range, and the voltage output is too low for any practical purpose.

Biological chemical reactions can also be utilized to generate micro power. A bio-solar cell reported by K. B. Lam et al. uses the thylakoid photo system isolated from spinach cells to convert light into electricity [37]. It generated a peak power density of $5.4 \text{ pW}/\text{cm}^2$ at a voltage of $5.2 \text{ }\mu\text{V}$. Exploration of biological micro power generation may offer special advantage for biological applications.

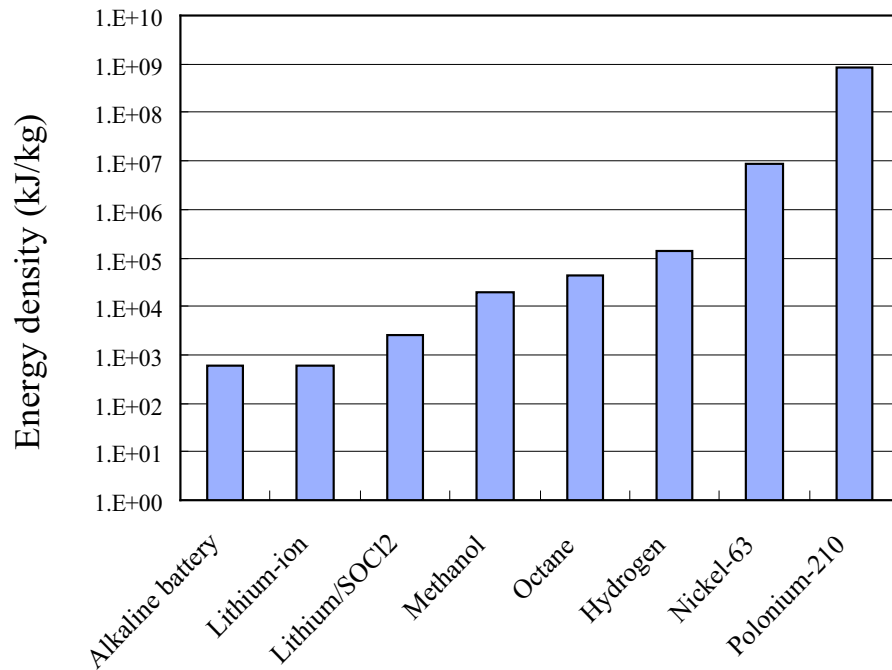


Figure 1.1: A comparison of energy densities of several battery technologies, some fuels and radioisotopes [29, 38].

1.5 Why Radioisotopes?

The potential for micro fuel cells and micro combustion power generation comes from the high energy densities of the fuels. Figure 1.1 shows a comparison of energy

Table 1.1: Specific powers of some radioisotopes, calculated based on the data from Ref. [38].

Radioisotope	Average energy (keV)	Half life ($year$)	Specific power (W/g)
^{63}Ni	17.4	100.2	0.0059
^{147}Pm	61.96	2.6	0.34
3H	5.7	12.3	0.33
^{210}Po	5304	0.379	142
^{238}Pu	5499	87.8	11

densities of several fuels, battery technologies and some radioisotopes. The energy densities of radioisotopes are calculated based on the kinetic energy of emitted charged particles. Radioisotopes clearly offer much larger energy densities than any other energy source. Therefore, if the energy from a radioisotope is utilized, a high energy density power source can be realized even at a low energy conversion efficiency. Furthermore, the high energy density of a radioisotope enables size-compatible power sources for micro devices. For both micro fuel cells and micro combustion power generators the volume of the fuel stored will determine how long the power supply can operate and fuel recharging may be required for long term operations. On the other hand, long term operation is readily achievable with the choice of some long half-life radioisotopes. Another advantage offered by radioisotopes is that nuclear decay is not affected by temperature or pressure so that power supplies capable of function under extreme temperature or pressure conditions are possible.

However, power output can be low from radioisotopes. The large energy den-

sities come from the integration over the half-lives of radioisotopes, which could be quite long. Table 1.5 shows the specific powers, in *Watt/gram*, of some radioisotopes calculated from the average energy carried by the emitted particles. Generally specific power tends to be small for a radioisotope with long half-life. To achieve high power output, large quantities of radioisotope can be used. However, this requires safety analysis from the point-of-view of accidental exposures to the environment. Therefore, low duty-cycle operation may be considered for appropriate applications to meet large power output requirement.

Chapter 2

Direct Charge Radioactive Power

Generation

Radioactivity was discovered by Henri Becquerel in 1896, when he found that a mixture of uranium salts emitted a mysterious penetrating radiation that passed through thin sheets of metal. A radioisotope is a radioactive isotope of an element. Radioisotopes emit energetic particles or photons at a rate governed only by the related nuclear decay process. The number of nuclear decays per unit time is called the activity of the radioisotope. The SI unit of activity is Becquerel (Bq), which means one decay per second. A commonly used unit is Curie (Ci), equivalent to 3.7×10^{10} decays per second.

Radioactivity has many applications in diverse areas, such as industry, agriculture, medical services. Power generation is one important field where nuclear power generators can perform more effectively than conventional power sources in many applications. Until very recently little research has been done in exploring radioactive micro power generation. Given the high energy densities of radioisotopes, it is promising to use radioactive power for MEMS and micro electronic devices.

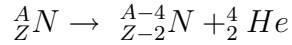
2.1 Radioactive decay

Radioactivity can be of different types [39, 40]:

1. Alpha decay

Alpha decay is characterized by the emission of an alpha particle in the

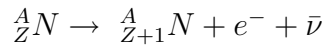
nuclear reaction. The reaction can be represented as:



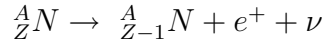
An alpha particle is a doubly ionized helium nucleus. The energy carried by an alpha particle is usually in the MeV range [38]. Because of their heavy masses and ionized state, alpha particles have a short range in materials compared to other radiations. Po-210, Am-241, Cm-242 are some examples of alpha emitting radioisotopes, or simply called alpha emitters.

2. Beta decay

A nuclear decay with a beta particle emission is called beta decay. Beta particles are essentially electrons or positrons. The one with electron emission is also called beta-minus decay, while for positron emission is called beta-plus decay. Beta-minus decay is represented as:



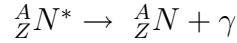
where $\bar{\nu}$ stands for antineutrino, and beta-plus decay as:



where ν represents neutrino. Most radioisotopes decay by beta emissions. The energy carried by an beta particle can be a few keV to about 1 MeV [38].

3. Gamma decay

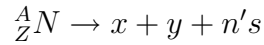
Gammas are electromagnetic radiations. A gamma ray may result from an excited nucleus in an alpha or beta decay. It can also be emitted by an nucleus stimulated by other means, such as neutron bombardment. Gammas have no mass or charge, so the nuclear species do not change in gamma decay. Gammas have very powerful penetration ability, and it is very difficult to shield against gamma radiations. Gamma decay can be represented as:



where “*” means an excited state.

4. Spontaneous fission

Very heavy elements sometimes fission spontaneously without neutron bombardment. It can be represented as:

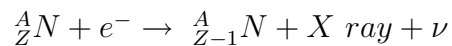


where x, y are fission fragments and n represents neutron. The process is very much like a neutron induced fission. Due to fact that spontaneous fission happens rarely and most of the released energy is retained in the fission fragments, it is not attractive for power generation.

5. Electron capture

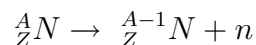
If there are too many protons in a nucleus and there is not enough energy to emit a positron, one of the orbit electrons, usually from K shell, is captured by a proton in the nucleus, forming a neutron and a neutrino. In the resulting electronic readjustments among the electron shells, X rays and Auger electrons are emitted. The energy associated with electron capture is low.

This decay can be represented as:



6. Neutron emission

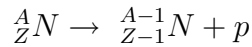
Neutron emission is a type of radioactive decay in which a neutron is simply ejected from a nucleus. It can be represented as:



Neutron emitter are very rare among radioisotopes. Some examples of radioisotopes which emit neutrons are beryllium-13 and carbon-14.

7. Proton emission

The radioactive decay in which a proton is emitted from a nucleus is called proton emission. Proton emission can occur from excited states in a nucleus following a beta decay; or can occur from the ground state of very proton-rich nuclei, in which case the process is very similar to alpha decay. It can be represented as:



Proton emission is not seen in naturally-occurring isotopes. Proton emitters can be produced via nuclear reactions, usually with a particle accelerator. Lithium-5 and nitrogen-11 are examples of proton emitters.

Among these radioactive decays, spontaneous fission, electron capture, neutron emission and proton emission happen rarely. Most of them occur very quickly within products of nuclear reactions, and are not often seen on Earth outside a nuclear reactor. Therefore, they are not suitable for micro power generation. For gamma decay, although there was some research on using it for power generation[41], due to the high penetration power, it is difficult to harness the energy carried by gamma rays and to provide good shielding for safety. Therefore, radioactive power generation usually either uses alpha decay or beta decay. It is noticed that majority of the radioisotopes decay through alpha or beta emission. The discussion that follows will focus on alpha and beta decays.

2.2 Nuclear Batteries

The large amount of kinetic energy carried by an emitted charged particle is the source of power generation. Usually power generation refers to electricity although for some applications other forms of energy such as heat, photons can also be

provided. Table 2.1 shows different ways of converting kinetic energy into electricity. At small scale, especially at MEMS scale, the surface to volume is very large, therefore heat loss is significant and it is not efficient to utilize those processes involving heat cycle. In fact, the conversions involve heat generation usually use large amount of activities, tens of Curies or even thousands of Curies, and the generators are large in size [39].

For the purpose to power MEMS devices and microelectronics, the means nuclear batteries use to generate electricity are more applicable. The first radioactive generator is actually a nuclear battery built by H. G. J. Moseley [47]. Nuclear batteries here refer to the radioisotopic power generators that do not use heat engines in the energy conversion process. Based on how nuclear batteries convert nuclear energy into electricity, nuclear batteries can be categorized into two groups. One is direct conversion nuclear battery. This type of nuclear battery makes the emitted charged particles do work against an impeding electrical field, hence converts the kinetic energy into electrical energy. The other type of nuclear battery uses the kinetic energy of the particles to generate some secondary effects for electrical power generation. It can be called secondary nuclear battery. In rare case, a nuclear battery may use the secondary effect to create another secondary effect which finally generates electricity. The kind of nuclear batteries will still be considered as secondary nuclear battery.

2.2.1 Direct Conversion Nuclear Battery

This type of nuclear battery directly collects the charges from a radioisotope source to generate electricity. Figure 2.1 gives a schematic of a direct conversion nuclear battery. Generally the radioisotope is placed as the central electrode and the

Table 2.1: Listed are different ways of converting kinetic energy from radioisotopes into electricity.

Conversion physical processes	Practical examples
Particle kinetic energy is converted into thermal energy by collisions, where particles are usually absorbed by certain material. Heat is then transformed into electricity by a dynamic heat engine.	Snap-2, 8 radioisotopic turbogenerators [39].
Kinetic energy of particles is first transformed into heat. Heat is then transformed into electricity by direct conversion processes, such as thermoelectric and thermionic conversion.	Snap-3B, 7 thermoelectric generators; Snap-13 thermionic generators [39].
The kinetic energy is converted into electricity directly by making the charged particles do work against an electrostatic field.	Direct conversion nuclear batteries [42, 43]
Electricity is obtained through some secondary effects, such as electron-hole pairs generation in semiconductors, gas ionization between dissimilar materials and a solar cell operated by the light emitted from a phosphor film activated by the particles.	Betavoltaic batteries [44, 45], Contact-potential-difference nuclear batteries [46].

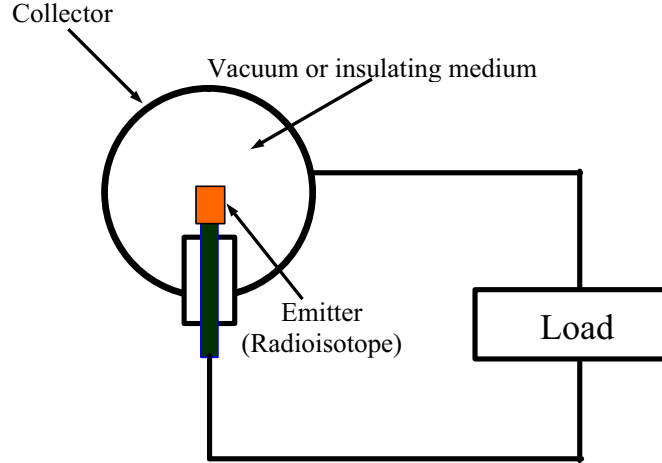


Figure 2.1: Schematic of a direct conversion type nuclear battery. A radioisotope is one electrode. A collector collecting the charged particles from the radioisotope is the other electrode. The open circuit voltage can be very high due to the high energy carried by the charged particles.

charged particles emitted are collected by the outer conducting electrode. The two electrodes form a capacitor and the volume in between is either vacuum or some dielectric material provided that the material will not absorb most of the charged particles. This type of battery was first demonstrated by Mosley in 1913 [48]. Because of the high energy carried by the charged particles, the voltage across the two electrodes can rise to several thousands of volts. Since the emitted particles have large energy compared to the voltage, the field produced by the voltage has little influence on the current although it tends to decrease the current. This type of nuclear battery behaves as a constant current source and the operating voltage depends on the load.

The current of a 1 *millicurie* beta emitting radioisotope is only 5.9 pA and 11.8 pA from an alpha emitter. Because there is no current multiplication process,

the current from this type of battery is very low. The battery is basically a capacitor so that it is only efficient at high operating voltage which greatly limits its applications.

2.2.2 Junction-type Nuclear Battery

Figure 2.2 shows the configuration of a junction-type nuclear battery. Charged particles pass through the depletion region of a p-n junction, generating many electron-hole pairs. Under the influence of the depletion region electric field, current and voltage are provided. Each electron-hole pair costs about 3 eV from the incident charged particles in a silicon p-n junction. For example, one β -particle from strontium-90 produces about 200,000 electron-hole pairs. Thus compared to the direct conversion nuclear battery, a much larger current can be obtained by this type of nuclear battery at the cost of lowering the output voltage, determined by the band gap of the semiconductor.

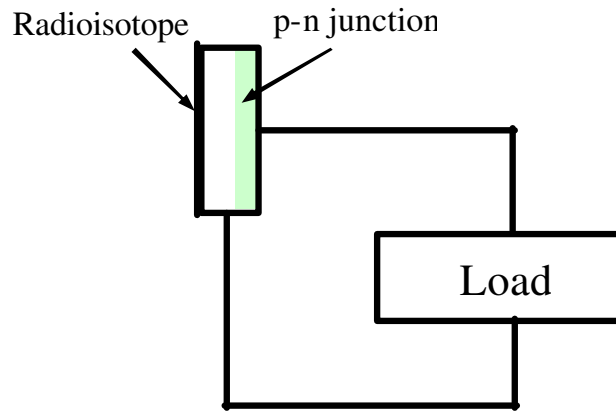


Figure 2.2: Schematic of a junction type nuclear battery. Electron-hole pairs are generated as the charged particles enter the p-n junction. Under the influence of the depletion region a current is formed.

The open-circuit voltage of a silicon junction-type nuclear battery is about several tenths of a volt [45, 48], so that a large number of cells have to be connected in series to provide an appropriate voltage. One important issue with junction-type nuclear battery is that when the energy of charged particles exceeds a certain threshold, about 200 *keV* for Si [48], the lattice structure of the junction will be damaged which eventually leads to the failure of the battery. Since for most radioisotopes the average energy carried by the emitted charged particles is larger than the threshold, this type of nuclear battery tends to have a short lifetime. While energy of the charged particles can be decreased by using a shield layer or other methods, with smaller energy the number of electron-hole pairs also decreases, which results in reduced power output and reduced efficiency. Alpha particle has a much larger size than beta particle and generally has a energy higher than 1 *MeV*, the battery will die very soon with an alpha source. So beta emitters are typically used for junction type batteries, which are usually called betavoltaic batteries.

2.2.3 Contact-potential-difference Nuclear Battery

The operating principle of contact-potential-difference (CPD) nuclear battery is illustrated in Figure 2.3. Two electrodes have to be made of different metals. The volume between the two dissimilar metals is irradiated by a radioisotope and the resulting ions are separated by the electrical field arising from the difference in contact potentials between the two electrodes. The open circuit voltage thus equals to the contact-potential difference, which is generally less than one volt. CPD-type nuclear battery has an open circuit voltage on the order of a volt was also reported [46]. The region between the two electrodes can be gas or the radioisotope

itself.

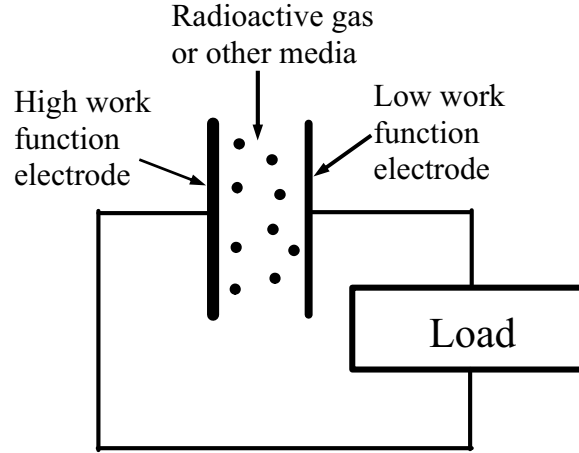


Figure 2.3: Schematic of a contact-potential-difference type nuclear battery. The two electrodes are made of different metals. The volume in between is some media irradiated by a radioisotope.

Tritium (3H) is a gaseous radioisotope, which offers the advantage that it can be mixed uniformly with some other gas. Therefore a large part of the beta particle energy is transformed into useful current. The CPD battery using tritium gives about 100 times the current from the beta source itself [48]. This is about half the theoretical current multiplication.

Although the current may be higher for a CPD nuclear battery than a direct conversion type nuclear battery, when a working gas is used, it is still small in absolute value. And for the ionization of the working gas to be efficient, the size of the CPD nuclear battery has to be large. Furthermore, the battery itself has a very high electrical impedance since the two electrodes form a capacitor.

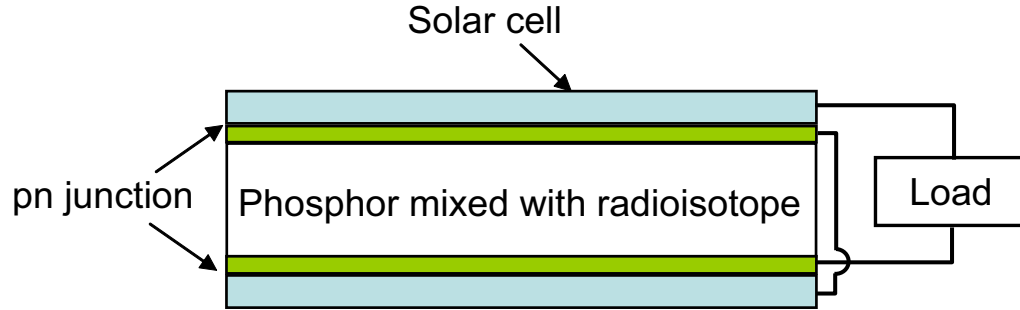


Figure 2.4: Schematic of a double conversion nuclear battery. Phosphor mixed with a radioisotope emits photons which are then converted into electricity by surrounding solar cells.

2.2.4 Double Conversion Nuclear Battery

In this type of nuclear battery radiation is partially absorbed in a phosphor to emit light. The light is then absorbed by surrounding solar cells to convert to electricity. Figure 2.4 illustrates the structure of a double conversion nuclear battery [39]. Since it takes two processes to achieve electricity, the efficiency of each has to be relatively high for a good overall efficiency. For the first conversion step, radioactive energy to light, the challenges are to achieve high absorption of emitted particles in the phosphor, to improve the conversion from nuclear energy to light and to minimize the light absorption in the phosphor. Because a solar cell is used, the performance of the solar cell is another limiting factor: the output voltage is limited and the power will be area dependant. Further, in order for the light to escape from the phosphor, the phosphor can not be made too thick. Therefore the solar cell is exposed to partial radiation which may result in damage and cause performance degradation.

2.3 Direct Conversion

Considering the operational principles of nuclear batteries, direct conversion offers the most straight forward way to convert nuclear energy into electricity. It also has the potential to achieve the best conversion efficiency [45]. In principle if the voltage across the collector and the radioactive source can reach the level corresponding to the average energy carried by the emitted particles, the conversion efficiency will approach 100%, although in reality all kinds of leakages will limit the ultimate conversion efficiency. Nevertheless the high voltage and low current nature of direct conversion nuclear batteries limits the applications and it is necessary to find a new approach. This dissertation presents a novel method of direct conversion which reduces the high-voltage, low-current barrier by using radioactive-mechanical-electrical cycle, resulting in high efficiency micro power generators.

Chapter 3

The Self-Reciprocating Cantilever:

Theory

Instead of simply miniaturizing a direct conversion nuclear battery, a new approach is taken to realize direct conversion of collected charges to mechanical movement. The realization of radioisotope-powered mechanical movement offers the opportunities to directly actuate a MEMS mechanical part.

3.1 Principle of Operation

The central idea lies in the direct conversion of collected charges into mechanical movement. The process of self-reciprocation can be divided into four steps:

1. A cantilever collects the emitted charged particles, namely α particles (He^{2+}) or β particles (e^- or e^+), from a radioisotope thin film source.
2. Because of charge conservation, charges of opposite sign are left in the source as it radiates charges into the cantilever. Therefore, an electrostatic force is generated between the cantilever and the radioisotope thin film. This force pulls the cantilever toward the source.
3. The cantilever eventually reaches the radioisotope thin film and the charges are neutralized via charge transfer.
4. Since the charges are neutralized, with the possibility that some residual charge may remain, the electrostatic force is nulled. The spring force on the

cantilever retracts it back to the initial position, maybe undergoing vibrations, and the cantilever begins to collect charges for the next cycle.

The cantilever will repeat this cycle as long as the radioisotope thin film is active. During the self-reciprocation process the cantilever acts as a *charge integrator* allowing energy to be stored and converted into both mechanical and electrical forms. Figure 3.1 illustrates this process with a beta source.

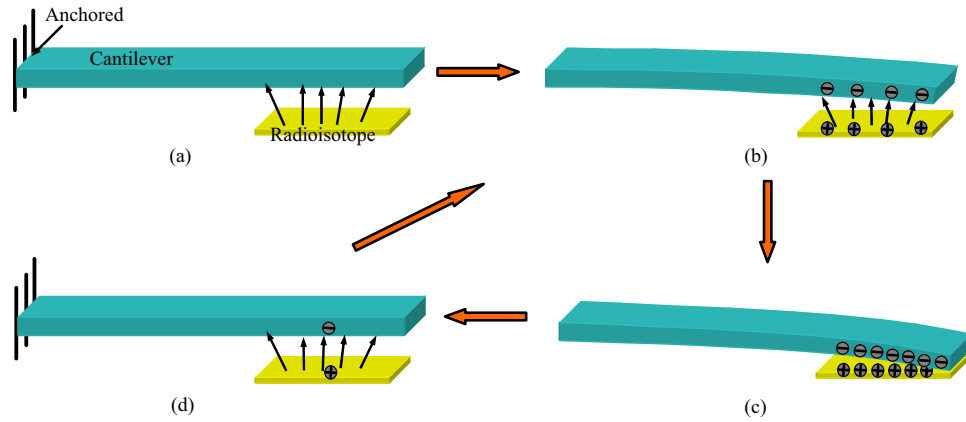


Figure 3.1: The self-reciprocation process with a beta source: (a) Electrons emitted from the radioisotope are collected by the anchored cantilever. Positive charges are left in the source because of charge conservation. (b) As more and more charges get collected, the electrostatic force becomes larger and pulls the cantilever toward the radioisotope. (c) Eventually the cantilever gets in contact with the source. Charges are neutralized through charge transfer. (d) The electrostatic force becomes almost zero as most of the charges are neutralized. The spring force of the cantilever retracts it back to its initial position and a new cycle begins.

3.2 Equivalent Circuit

Figure 3.2 shows the equivalent circuit of the self-reciprocation cantilever. There are three components: a current source, a resistor and a variable capacitor.

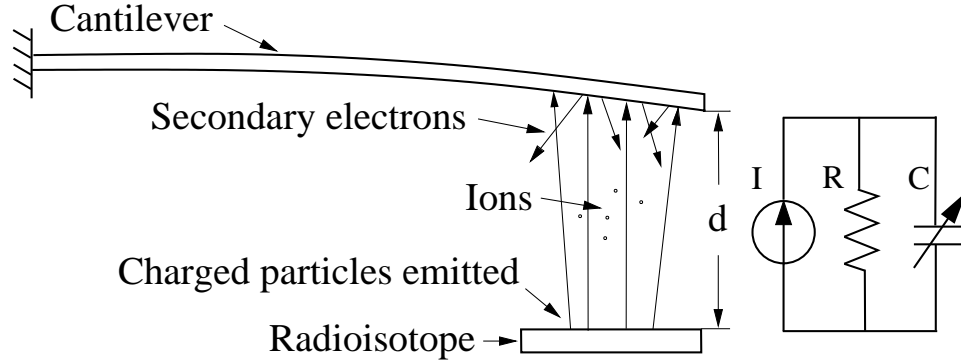


Figure 3.2: Equivalent circuit of the self-reciprocating cantilever. The distance between the cantilever and the radioisotope is exaggerated. The emitted charges can be modeled as a current source. The resistor R represents leakage paths. The cantilever and the radioisotope form the capacitor C .

The radioisotope thin film is modeled as a current source with the current I determined by the activity N of the radioisotope as:

$$I = 1.6 \times 10^{-19} \times 3.7 \times 10^7 \times N \quad (3.1)$$

The unit for the activity N is millicurie (mCi). A beta emitter is assumed. For an alpha source, I will be doubled.

The resistor represents all the possible leakage paths. There are at least three possible mechanisms contributing to the leakage.

1. There are naturally generated ions in the environment which may neutralize part of the charges on either the cantilever or the radioisotope thin film.

2. The energy of the emitted beta particles is high enough that they may ionize the gas molecules around. Under the electric field generated by the charges in the cantilever and the source, those ions will form a leakage current.
3. Secondary electrons including backscattered electrons may emitted from the cantilever when beta particles hit the cantilever. Those secondary electrons can form a leakage current with a polarity opposite to the emitted current.

The cantilever and the radioisotope thin film electrodes form the air-gap capacitor. As the distance in between keeps changing, the capacitance is variable.

3.3 Electromechanical Model

Charge conservation results in:

$$\alpha I - \frac{V}{R} - \epsilon_0 A \frac{\partial}{\partial t} \left(\frac{V}{d} \right) = 0 \quad (3.2)$$

The symbols in the above equation are:

I : the total emitted current from the radioisotope

α : collection efficiency

V : the voltage across the source and the cantilever

R : the equivalent leakage resistance

A : the area of the capacitor

ϵ_0 : the permeability of vacuum

t : the time

d : the distance between the cantilever and the source

The first term is the emitted current; the second is the leakage current and the third is the displacement current. The parameter α is an empirical coefficient

describing the portion of the total emitted current that gets collected by the cantilever. There are at least three reasons for imperfect charge collection (i.e., $\alpha < 1$). First, the charged particles emitted from the source have an angular distribution and only the particles that fall in the solid angle formed by the intersection of the radioisotope thin film and the cantilever are collected. Secondly, some high energy particles can travel through the cantilever. Thirdly, when secondary electrons are emitted from the cantilever, positive charges are left in the cantilever, reducing the net negative charges.

With the assumption that the cantilever moves very slowly, which is verified by experiments, the cantilever's inertia can be ignored. In this quasi-static approximation, the electrostatic attraction force acting on the cantilever is exactly balanced by the spring force of the cantilever. This can be written as:

$$k(d_0 - d) = Q\mathcal{E} \quad (3.3)$$

where the symbols are:

k : the spring constant

d_0 : the initial distance

d : the distance between the cantilever and the radioisotope thin film

Q : the total charges on the cantilever

\mathcal{E} : the electric field

The electric field on the electrodes can be approximated as $\mathcal{E} = Q/2\epsilon_0 A$ by assuming a uniform field, because the gap between the source and the cantilever and the angle of approach between the cantilever and the source are small, allowing the approximation that an average gap d exists. Also due to the same uniform field argument, the capacitor can be modelled as a parallel plate capacitor C and

the charge on it is:

$$Q = CV = \frac{\epsilon_0 AV}{d} \quad (3.4)$$

Substitute Equation 3.4 into Equation 3.3:

$$k(d_0 - d) = \frac{Q^2}{2\epsilon_0 A} = \frac{1}{2}\epsilon_0 A \frac{V^2}{d^2} \quad (3.5)$$

This equation can be rewritten as:

$$V = \sqrt{\frac{2k}{\epsilon_0 A}} \sqrt{d_0 - d} \quad (3.6)$$

Substituting Equation 3.6 into Equation 3.2 results in:

$$\frac{\partial d}{\partial t} = \frac{2}{\epsilon_0 R A} (d_0 - d)d - \frac{\sqrt{2}\alpha I}{\sqrt{\epsilon_0 k A}} \sqrt{d_0 - d} \quad (3.7)$$

This equation can be solved numerically to compare with experimental results given that R is known. Since R is a strong function of d , an analytical solution to the equation is difficult. At atmospheric pressure, the collected charges can easily be neutralized by ionized and polarized air molecules. This will reduce R to a small value, resulting in negligible $\partial d/\partial t$ as observed in experiments done in air. To obtain a large R , vacuum operation is required. Under the experimental condition where the pressure is between 3×10^{-6} Torr to 50 mTorr, R is found to be on the order of 10^{15} to 10^{14} Ω . This result allows the elimination of the first term on the right hand side of Equation 3.7 and it becomes:

$$\frac{\partial d}{\partial t} = -\frac{\sqrt{2}\alpha I}{\sqrt{\epsilon_0 k A}} \sqrt{d_0 - d} \quad (3.8)$$

which can be solved to yield:

$$d = -\left(\frac{\alpha I t}{\sqrt{2\epsilon_0 k A}} + \beta\right)^2 + d_0 \quad (3.9)$$

where β is a constant of integration. This simplification in effect assumes perfect vacuum.

3.4 Operational Characteristics

Equation 3.9 gives the analytical solution of how the distance between the cantilever and the radioisotope thin film changes with respect to time. At $t = 0$, it leads to:

$$d_0 - d = \beta^2 \quad (3.10)$$

This shows that at time 0, the cantilever may not be at its original position and the offset is β^2 . At the beginning of the very first cycle the cantilever is at its original position. But when the cantilever is released at the time that the charges are neutralized, it may not go back to the exact original position. The reason is that there may be residual charge left on the cantilever or the source, or there is plastic strain on the cantilever. Therefore, β in Equation 3.9 is for modeling the possible residual charge or plastic strain.

The movement of the cantilever which has a length of a few centimeters is in the range of tens of micrometers to a few millimeters. So it is unlikely that there will be plastic strain on the cantilever. Assuming the amount of residual charge is Q_0 , with uniform electric field assumption, combining Equation 3.5 and 3.10 results in

$$Q_0 = \beta \sqrt{2\epsilon_0 k A} \quad (3.11)$$

With Equation 3.11, the amount of residual charge can be estimated once β is known, assuming linear region of operation.

The period of the reciprocation can also be calculated with this model. Letting $d = 0$ in Equation 3.9 gives:

$$T = (\sqrt{d_0} - \beta) \sqrt{2\epsilon_0 k A / \alpha I} \quad (3.12)$$

Generally the charge neutralization is quite complete so that there is little residual

charge left, that is, β can be ignored. Then the reciprocation cycle time can be simply estimated as

$$T = \frac{\sqrt{2\epsilon_0 k A d_0}}{\alpha I} \quad (3.13)$$

When the cantilever is released, the spring force of the cantilever may be used to drive other moving structures. It can be calculated using:

$$F = k(d_0 - d) \quad (3.14)$$

The maximum force output will be achieved at $d = 0$ and it is:

$$F_{max} = k d_0 \quad (3.15)$$

As there are charges stored in the variable capacitor, there should be voltage across it. This voltage can be determined by Equation 3.6, which also reveals that the voltage has a maximum. Taking differential on both sides of Equation 3.6 and letting $\partial V / \partial d = 0$ results in:

$$\frac{\partial V}{\partial d} = \sqrt{\frac{2k}{\epsilon_0 A}} \left(\sqrt{(d_0 - d)} - \frac{d}{2\sqrt{d_0 - d}} \right) = 0 \quad (3.16)$$

Solving this yields $d = 2d_0/3$. The maximum voltage during reciprocation can then be obtained by substituting this d into Equation 3.6. The result is: the maximum voltage $V_{max} = \sqrt{8kd_0^3/27\epsilon_0 A}$ and it appears when $d(t) \equiv d_{V_m} = 2d_0/3$.

The reciprocation is also a process during which nuclear energy is converted into electrical and mechanical energy. The energy stored in the cantilever per cycle is composed of two parts. One is the mechanical energy:

$$E_M = \frac{1}{2} k (d_0 - d)^2 \quad (3.17)$$

The other is the electrical energy:

$$E_E = \frac{1}{2} C V^2 \quad (3.18)$$

Substitute $C = \epsilon_0 A/d$ and Equation 3.6 into the equation above:

$$E_E = (d_0 - d)d \quad (3.19)$$

The mechanical energy reaches its maximum $E_{Mmax} = kd_0^2/2$ when d becomes zero, i.e., when the cantilever is released. The electrical energy has its maximum $E_{Emax} = kd_0^2/4$ when $d = d_0/2$, which is found by taking $\partial E_E/\partial d = 0$.

The total energy emitted by the radioisotope in one cycle can be calculated as:

$$E_r = NE_e T \quad (3.20)$$

where N is the activity, E_e is the average energy of the emitted electrons and T is the period. Since the electrical energy becomes zero at the end of the cycle as from Equation 3.19, the energy output is the maximum mechanical energy. Therefore the *energy efficiency*, η , of the device for one cycle can be calculated as:

$$\eta = \frac{E_{Mmax}}{E_r} = \frac{kd_0^2}{2E_r} \quad (3.21)$$

substituting Equation 3.20 and 3.13 into the above equation gives

$$\eta = \frac{\alpha q}{E_e} \sqrt{\frac{kd_0^3}{8\epsilon_0 A}} \quad (3.22)$$

where q is the charge carried by each particle and $I = qN$ is used.

The conversion efficiency can be maximized by designing the device such that the peak voltage across the capacitor formed by the source and the cantilever, V_{max} , equals to the average electron energy. This gives

$$V_{max} = \sqrt{\frac{8}{27} \frac{kd_0^3}{\epsilon_0 A}} = \frac{E_e}{q} \quad (3.23)$$

Combining Equation 3.23 and 3.22, it results in

$$\eta_{max} = \frac{\sqrt{27}}{8} \alpha \quad (3.24)$$

To obtain the upper limit of η , assuming a 100% α , the maximum possible η is 65%.

3.5 Decay of the Radioisotope and Device Longevity

The decay of the radioisotope has not yet been taken into account. For short term analysis, the decay of a long half-life ($> 1 \text{ year}$) radioactive source can be ignored because the reciprocation period (usually in minutes or seconds) is much shorter in scale. While for a short half-life source, it is necessary to consider the decay since the activity of the source may significantly change during one cycle. On the other hand, for long term operation, decay has to be taken into account no matter what the half-life of the radioisotope is.

Assuming that the cantilever has been working for n cycles and the total time is t_n , for cycle $n + 1$, Equation 3.8 needs to be modified as:

$$\frac{\partial d}{\partial t} = -\frac{\sqrt{2}\alpha I_0 e^{-\gamma(t_n+t)}}{\sqrt{\epsilon_0 k A}} \sqrt{d_0 - d} \quad (3.25)$$

where I_0 is the current from the radioisotope at the very beginning $t = 0$ and γ is the decay constant where at time t the activity of the radioisotope becomes $e^{-\gamma t}$ of the original activity. This equation results in:

$$d = -\left[\frac{\alpha I_0 e^{-\gamma t_n}}{\gamma \sqrt{2\epsilon_0 k A}} (1 - e^{-\gamma t}) + \beta\right]^2 + d_0 \quad (3.26)$$

The cycle time of cycle $n + 1$ is:

$$T_{n+1} = \frac{-1}{\gamma} \ln\left(1 - \frac{\gamma(\sqrt{d_0} - \beta)\sqrt{2\epsilon_0 k A}}{\alpha I_0 e^{-\gamma t_n}}\right) \quad (3.27)$$

If the cantilever is designed such that it reciprocates at a time scale much smaller than the half-life of the radioisotope, i.e., $\gamma(\sqrt{d_0} - \beta)\sqrt{2\epsilon_0 k A}/(\alpha I_0 e^{-\gamma t_n}) \ll 1$, Taylor expansion, $\ln(1 + z) \approx z$ for $z \ll 1$, can be used for the right hand side of Equations 3.27:

$$T_{n+1} = \frac{(\sqrt{d_0} - \beta)\sqrt{2\epsilon_0 k A}}{\alpha I_0 e^{-\gamma t_n}} \quad (3.28)$$

This essentially means that the reciprocation starting at t_n is determined by the activity at the beginning of the cycle.

In conclusion, Equation 3.26 and 3.27 can be used for long term operation and Equation 3.9 is good enough for short term analysis, where time scale is based on the half-life of the specific radioisotope used. As the radioisotope decays, the reciprocation cycle will be longer. The device lifetime is determined by the half-life of the radioisotope, given the material of the cantilever can sustain the operation.

3.6 Radioisotope Selection

Many radioisotopes emit α or β particles [38]. To make a choice, the following criteria need to be considered: safety, energy, activity and half-life.

Safety is always a great concern when using radioisotopes. Because the strong penetration ability of gamma rays, one wants to use a radioisotope which emits only α or β particles without any gamma emission. Those radioisotopes are called pure alpha or beta emitters. Furthermore, the lower the energy of the charged particles, the safer the radioisotope is. From the operation principle of direct charge collection, the amount of collected charges is the main concern while the energy of charged particles is less important. Although the charged particle has to have enough kinetic energy to overcome the electric field generated by the collected charges, the average energy of particles ($> 1 \text{ keV}$ for all of the radioisotopes) is more than enough. Since the energy stored in the structure comes from the work done by those charged particles to overcome the electric field across the source and the collector, it is easier to achieve higher efficiency with a lower energy source. One more concern is that in order to catch the charged particles, the collector has to be thick enough, otherwise the particles may pass through it and no charges will

be collected. Therefore it is preferred to use a low energy source. Alpha particle generally has a kinetic energy more than 1 MeV and it posts more safety hazard since its size is large and it carries two positive charges. So only low energy pure beta emitters are considered in the experiments.

Table 3.1 lists some pure beta emitter candidates. The specific activity is the amount of activity per unit mass of a radioisotope. With a larger specific activity, a radioisotope can offer higher activity at the same amount. Since a higher activity means more current, it is desired that the radioisotope has a large specific activity, which helps when scaling to MEMS scale. The ranges in Cu and Si are intended to demonstrate the magnitude of thickness for a metal collector or a Si collector. The small maximum range in Si shows the feasibility of safe handling with silicon based devices, especially MEMS devices. Reference [49] gives a table for estimating the travel range of electrons inside different materials. With the continuous-slowing-down approximation (CSDA) range of electron in a material from the table, the range is then calculated as:

$$Range = \frac{CSDA\ range}{Density\ of\ the\ material} \quad (3.29)$$

Appendix A gives the explanation of CSDA range.

The half-life of the radioisotope directly affects the shelf life of the cantilever. Depending on the specific application, different radioisotope may be used to make the device have a lifetime meeting the design requirement. For long term operation, a long half-life radioisotope is the choice.

Additional properties include easy access and safe storage. With all those considerations in mind, *nickel-63* is a strong candidate. It is a pure beta emitter. The average energy of the beta particles is 17.4 keV and the maximum is at 66.9 keV [38]. The electrons can not go through the outmost layer of human

Table 3.1: Listed are some pure beta emitting radioisotope candidates. The first three columns are obtained from [38], while the activity density is derived from the specific activity. The ranges in Cu and Si are estimated for the emitted electrons with the maximum energy [49].

Radio- isotope	Average energy (<i>keV</i>)	Half life (<i>year</i>)	Specific activity (<i>Ci/g</i>)	Activity density (<i>Ci/mm</i> ³)	Maximum range in Cu (<i>μm</i>)	Maximum range in Si (<i>μm</i>)
⁶³ <i>Ni</i>	17.4	100.2	56.8	0.506	14	30
³² <i>Si</i>	68.8	172.1	64.9	0.151	107	350
⁹⁰ <i>Sr</i>	195.8	28.8	138	0.35	332	1100
¹⁰⁶ <i>Ru</i>	10.03	1.06	3300	40.8	5	15
³² <i>P</i>	694.9	0.04	285700	520	1344	3200

skin [50] even with the maximum energy, so it is a very safe source. It is a metal so that when the cantilever touches the source charge neutralization happens easily. Furthermore, nickel is one of the metals commonly used in MEMS devices, so the integration of nickel-63 with MEMS processing should not cause additional technical problems.

3.7 Summary

The operation principle of a self-reciprocating cantilever which realizes direct charge collection to mechanical actuation is presented. An electromechanical model is developed to characterize the cantilever. The bending of the cantilever, the volt-

age across the air-gap capacitor, the reciprocation period and the energy output can be calculated based on the model. It is found that the energy conversion efficiency has a upper limit of 65%. The effect of the radioisotope decay on the reciprocation period is also determined. Finally the radioisotope selection is discussed and Ni-63 becomes the choice.

Chapter 4

The Self-Reciprocating Cantilever:

Experiment

To verify the operation principle and the electromechanical model, cantilevers are fabricated and a series of experiments have been conducted.

4.1 Radioisotope Source

The Ni-63 radioisotope source is purchased from Isotope Products Laboratory (IPL). It is a $1\text{ cm} \times 1\text{ cm}$ ^{63}Ni thin film electroless-plated onto a same size $100\text{ }\mu\text{m}$ thick Ni plate. The activity of the source is claimed to be 4 mCi . Another source made by NRD LLC is also used occasionally. It is a $4\text{ mm} \times 4\text{ mm}$ ^{63}Ni thin film electroplated on a $2.5\text{ cm} \times 2.5\text{ cm} \times 1\text{ mm}$ Al plate. The claimed activity is 1 mCi .

Unfortunately, the company does not measure the activity directly, and the activity is estimated by calculating how much Ni-63 is plated onto the base plate. Due to *self absorption* the claimed activity may not equal to the amount of activity coming out of the source. Self-absorption comes from the fact that the electrons emitted have a finite range in Ni-63 itself, which has a maximum of $15\text{ }\mu\text{m}$. Therefore not all the electrons emitted may come out of the surface, especially those emitted from the atoms far away from the surface, and it also depends on which angle the electron travels at. It is then necessary to characterize the source itself. A simple approach is taken for this purpose: to measure the current coming out of the source. The source is put inside a vacuum chamber and placed near one

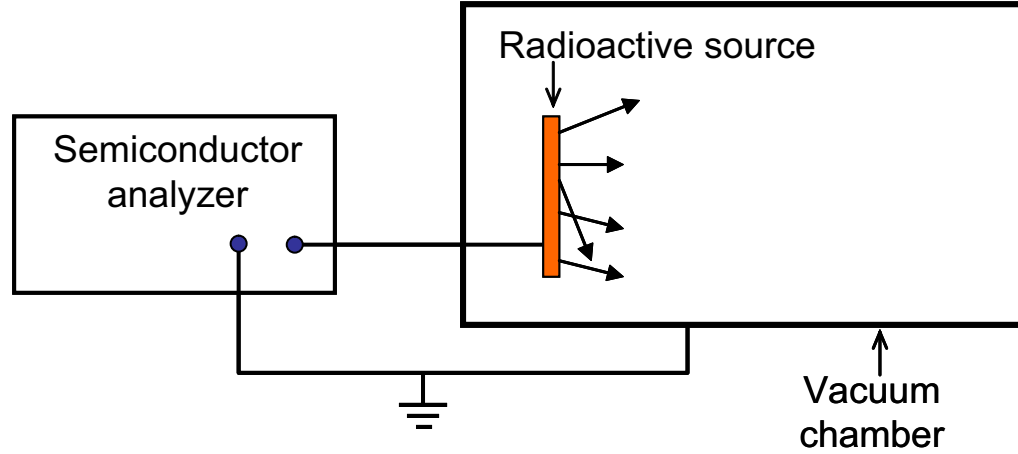


Figure 4.1: The experimental setup for measuring the current from the source is shown. Drawing is not to scale. The vacuum chamber is much larger than the source. The source is connected to a source-measurement unit of a Keithley 4200 semiconductor analyzer. The chamber is connected to the ground unit.

side of the chamber, facing the opposite side. This is to prevent the backscattered electrons and secondary electrons generated at the chamber wall from coming back to the source. The pressure is generally kept at $1.2 \times 10^{-6} \text{ Torr}$. A Keithley 4200 semiconductor analyzer is used to measure the current. The chamber is connected at ground and the source is hold at zero bias voltage. Figure 4.1 illustrated the measurement setup. The measured current from the IPL source is 5.75 pA . This is equivalent to about 1 mCi based on Equation 3.1, while the claimed activity is 4 mCi . There is obvious difference between the claimed activity and the measurement result. Therefore the activity claimed by the company will be called *nominal activity* and the measured activity will be called *effective activity*.

4.2 Cantilever

Copper cantilevers are used for the experiments. The thickness is determined with the consideration to capture most of the electrons hitting the cantilever. The range in copper for the electrons with maximum energy from a Ni-63 source is 14 μm . Therefore as long as the thickness of the copper cantilever is more than 14 μm it should be able to capture the highest energy electrons. In the experiments thickness in the range of 50 to 125 μm have been used to achieve different stiffness for the cantilever. One concern is that any surface asperity on the cantilever may amplify electric fields, and introduce discharging before the cantilever touches the radioisotope. To avoid this and to make the cantilever and the radioisotope thin film a parallel plate capacitor, polishing with sandpaper and flattening with a blade are used when necessary.

4.3 Setup

Figure 4.2 shows a picture of the experimental setup along with a schematic. The setup is placed inside a vacuum chamber. The cantilever is clamped by two Teflon pieces which is fixed inside the chamber. Teflon is used for electrical insulation purpose. Ceramic pieces are also used for better clamping. The radioisotope source is clamped by two glass slides which also provide electrical insulation. The slides are mounted on a Teflon base which itself is mounted on a linear stage. With the linear stage the initial distance between the radioisotope source and the cantilever can be adjusted. The two glass slides were replaced later by two Teflon pieces to protect the radioactive source since scratch of the source surface will introduce contamination. The chamber has a glass top so that the movement of the cantilever

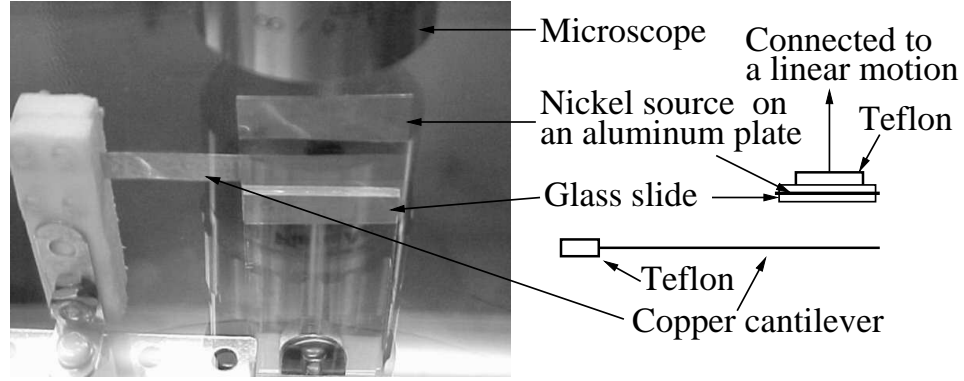


Figure 4.2: The experimental setup: a copper cantilever ($5\text{ cm} \times 5\text{ mm} \times 60\text{ }\mu\text{m}$) is placed at a controlled distance away from a $1\text{ mCi } ^{63}\text{Ni}$ ($4\text{ mm} \times 4\text{ mm}$) thin film source electroplated on a 1 mm thick aluminum plate.

can be monitored by a CCD camera outside the chamber. The CCD camera is connected to a VCR to record the reciprocation process for future analysis. A turbo pump together with a diaphragm roughing pump provides a vacuum up to $1.2 \times 10^{-6}\text{ Torr}$.

4.4 A Typical Distance versus Time Curve

Figure 4.3 shows a typical distance versus time curve. The solid line is a fitting done with the electromechanical model. Table 4.1 gives the experimental parameters and The IPL source is used. The cantilever tested will be referred as the sample cantilever later.

From the fitting, α and β of Equation 3.9 can be determined. The results for the particular example are $\alpha = 90.5\%$ and $\beta = 0.012\text{ }\mu\text{m}^{-1/2}$. The amount of residual charge calculated with β , according to Equation 3.11 is $2.9 \times 10^{-13}\text{ Coulombs}$, which is about 0.1% of the total amount emitted.

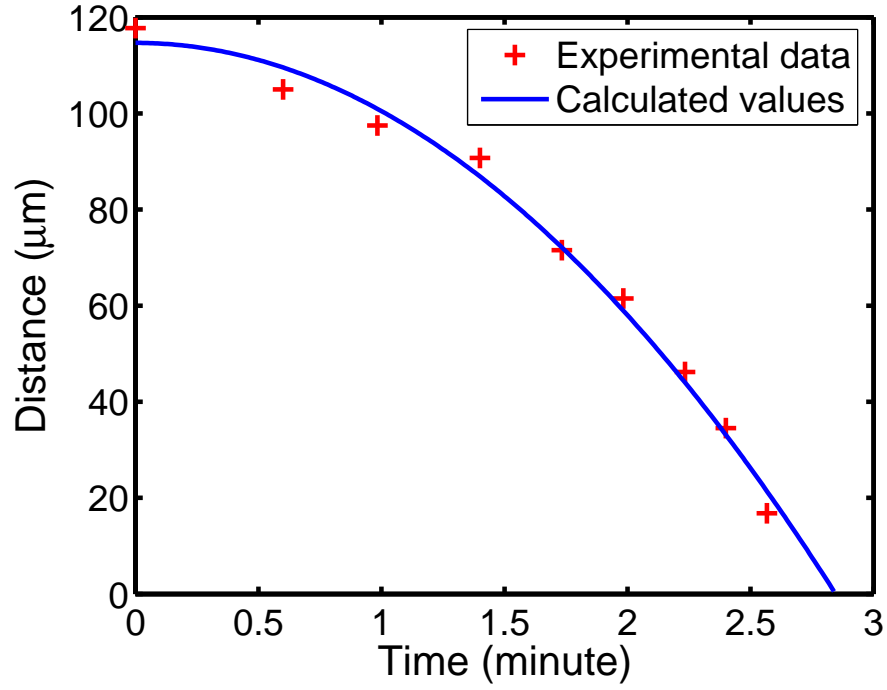


Figure 4.3: Measured and calculated distance versus time curves for the sample cantilever actuated by the ^{63}Ni source. The initial gap is $118\ \mu\text{m}$.

Table 4.1: Experimental parameters

Pressure	$2.25 \times 10^{-6} \text{mTorr}$
Cantilever dimensions	$4\ \text{cm} \times 3\ \text{mm} \times 90\ \mu\text{m}$
Spring constant	1.17N/m
Initial distance	$118\ \mu\text{m}$
Period	$2\ \text{minutes}\ 41\ \text{seconds}$

4.5 Air-gap Capacitor Voltage

The voltage across the air-gap capacitor formed by the cantilever and the radioisotope source varies as the cantilever moves toward the radioisotope thin film, which

can be calculated using Equation 3.6. Figure 4.4 shows this change.

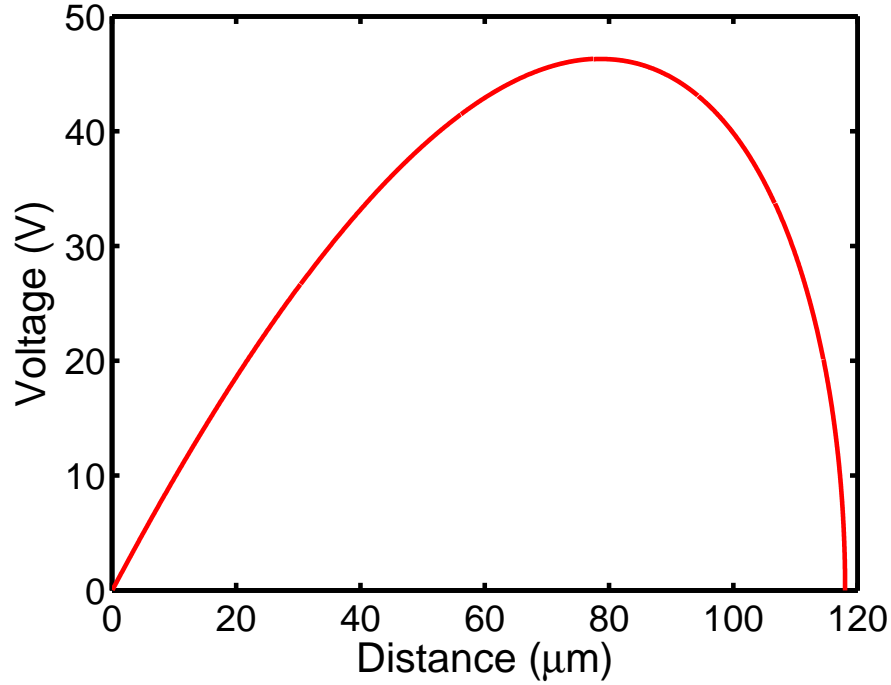


Figure 4.4: The calculated voltage across the cantilever and the radioisotope is plotted against the distance in between. The maximum voltage is 46 V.

The maximum voltage across the air-gap capacitor is only 46 V with this particular experimental setup. This clearly tells that most of the kinetic energy of the emitted electrons has not be harvested, which leads to a low energy conversion efficiency.

4.6 Mechanical and Electrical Energies

The energies stored in the system includes mechanical energy and electrical energy. Equation 3.17 and 3.19 are used to obtain Figure 4.5. The total energy is just the sum of the mechanical and the electrical energy. As seen from Figure 4.5,

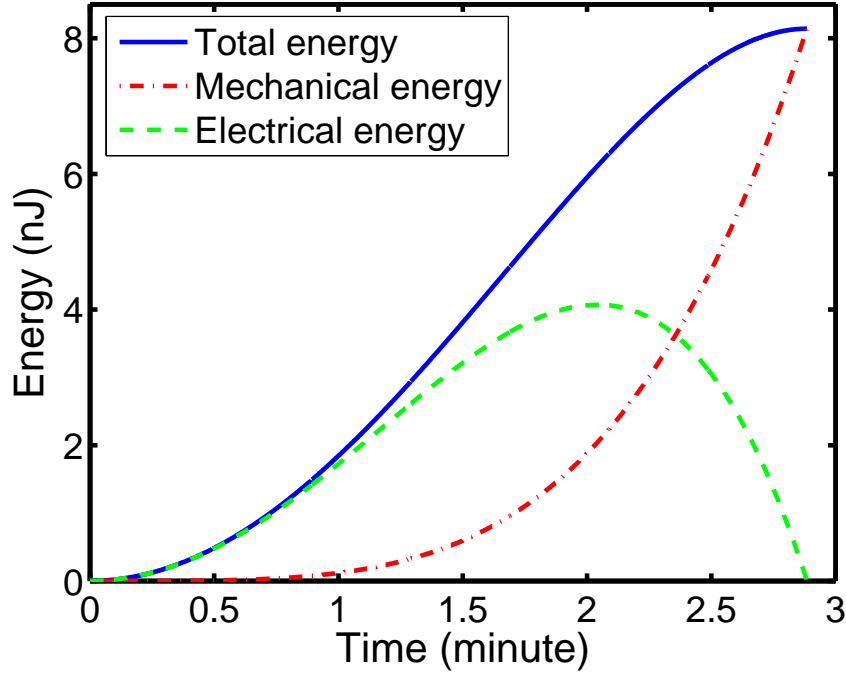


Figure 4.5: Energies stored in the cantilever are plotted against time with an initial gap of $118 \mu m$ for the sample cantilever.

the mechanical energy keeps increasing during one reciprocation cycle, while the electrical energy first reaches its maximum and then begins to decrease. The electrical energy becomes zero at the end since all the charges are neutralized.

The force output can be determined according to Equation 3.15. All the results are listed in Table 4.2.

The energy efficiency of the cantilever based on the effective activity, according to Equation 3.21, is:

$$\eta = \frac{8.15 \times 10^{-9}}{17 \times 10^3 \times 0.3 \times 5.75 \times 10^{-12} \times 161} = 0.17\% \quad (4.1)$$

As expected, the energy efficiency is low despite a high α . This is because the cantilever only collects the charges without utilizing most of the kinetic energy of

Table 4.2: Some characteristics of the cantilever with an initial distance of $118 \mu m$.

Force output	0.14 mN
Energy output (maximum mechanical energy)	8.15 nJ
Maximum electrical energy	4.07 nJ
Highest voltage	46 V

the emitted particles. Although part of the kinetic energy is consumed to conquer the electric field built between the cantilever and the radioisotope thin film, it is a tiny portion since the voltage across the capacitor is very low.

4.7 The Effect of Initial Distance

Intuitively different initial distance will result in different reciprocation period. A series of experiments with different initial distances ranging from $45 \mu m$ to 6 mm are conducted to investigate the effect of initial gap on the reciprocation process. The sample cantilever is used and the vacuum is maintained at $2.25 \times 10^{-6} \text{ Torr}$. Depending on the initial gap, the operation of the cantilever can be categorized into different regimes.

4.7.1 Normal Reciprocation

When the initial gap are not so large that pull-in would happen, which will be discussed next, the cantilever reciprocates as predicted by the electromechanical model. Figure 4.6 shows how the reciprocation periods vary with different initial gaps between $50 \mu m$ and $160 \mu m$. The circles are experimental data and the

solid line is the fitting curve with Equation 3.13. In Figure 4.6 a good fit is observed within certain range, specifically $50\ \mu m$ to $120\ \mu m$. At a larger initial gap inconsistency begins. This shows the relative invariance of α in certain gap range and dependency of α on the initial distance. The fitting also proves the validity of the electromechanical model. Therefore once α is determined with one initial distance, Equation 3.13 can be used to estimate the reciprocation period with a different initial gap provided the difference is not too much.

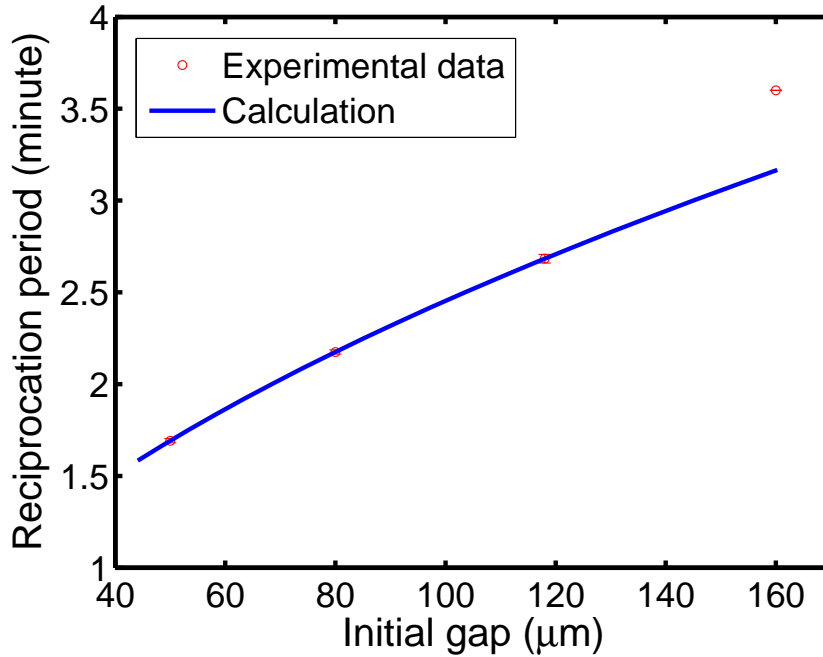


Figure 4.6: Measured and calculated reciprocation periods for the sample cantilever with different initial gaps.

4.7.2 Pull-in

As the initial gap keeps increasing, instead of slowly bending all the way down to the source until making contact eventually, pull-in happens. The cantilever

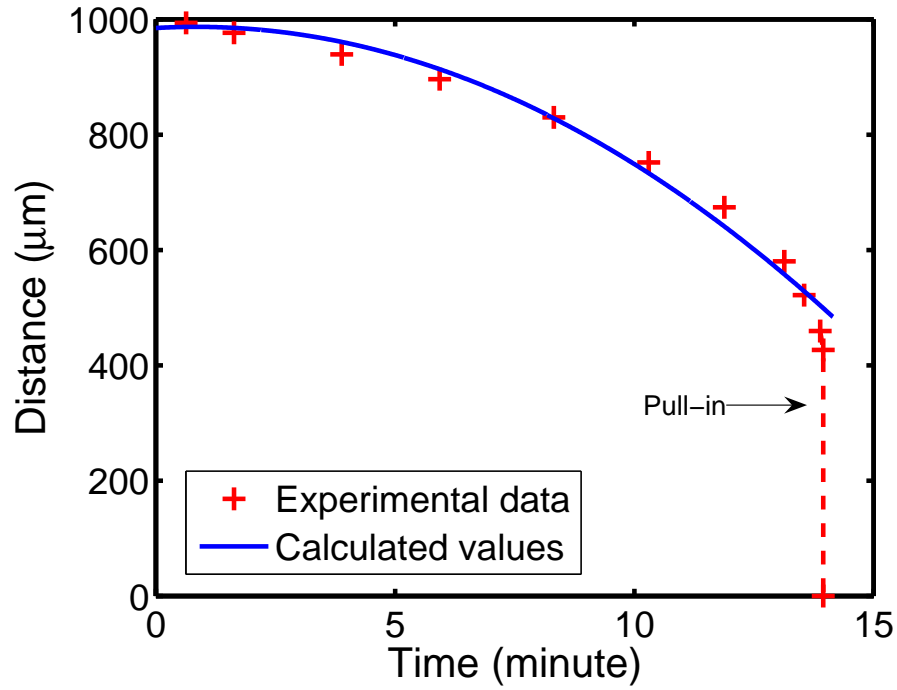


Figure 4.7: The distance versus time curve is plotted for an initial gap of 1 mm where pull-in happens.

bends to certain position then snaps into the source. For the sample cantilever, pull-in is observed starting with an initial gap of 200 μm until the gap increases to 2.5 mm . Figure 4.7 shows a d versus T curve where pull-in happens with an initial gap of 1 mm . Amazingly the fitting with the model is still very good, as illustrated in the figure, until the point where the pull-in happens. This tells that the charge accumulation mechanism is the same as the normal reciprocation. The reciprocation period versus the initial gap and the pull-in deflection, i.e., the deflection of the cantilever when pull-in happens, are plotted in Figure 4.8. Due to pull-in the cantilever is able to travel more distance than if there is no pull-in, given the same time. Since larger deflection means more energy output, pull-in helps efficiency.

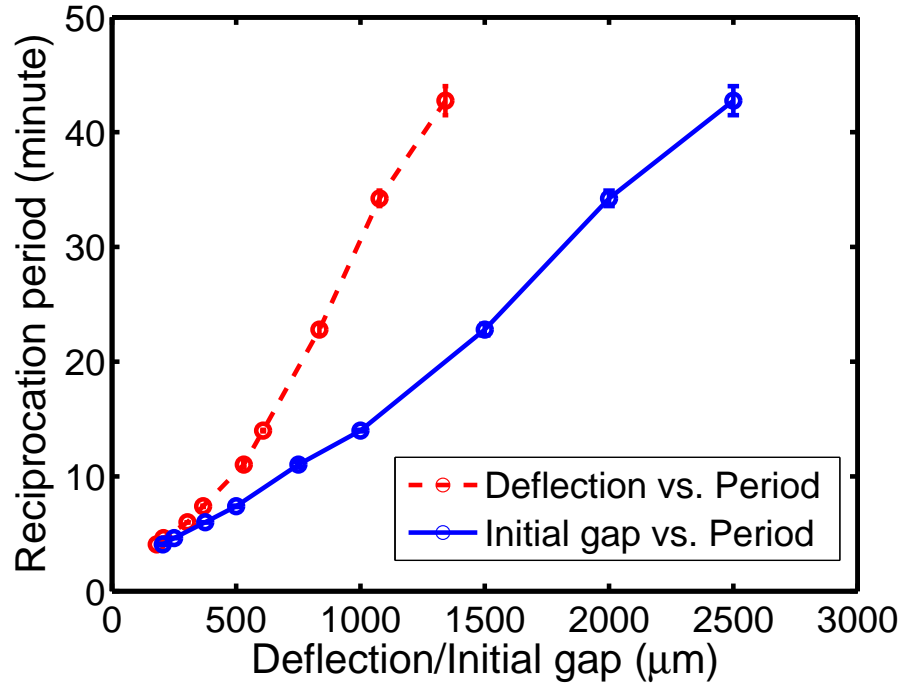


Figure 4.8: The reciprocation period versus the initial gap and the pull-in deflection are plotted.

4.7.3 Air Breakdown

The initial gap is further increased. In this regime, air breakdown happens. It is observed that the cantilever moves to certain position first then either virtually stops there for quite a while or moves significantly slower than before, then suddenly the cantilever is released. Since the cantilever moves toward its initial position instead of toward the source, an air breakdown must happen to cause charge neutralization. In this situation, incomplete discharge becomes more noticeable, which can be identified by the position of cantilever after breakdown. For this cantilever, air breakdown happens with an initial gap between 3 *mm* and 5 *mm*. Figure 4.9 plots the normalized deflection and time versus the initial gap. Normal-

ized deflection is d/d_0 with d being the deflection where the breakdown happens. Figure 4.10 plots the estimated breakdown voltage and corresponding electric field. No obvious relationship can be identified except it seems at 4 and 5 mm initial gaps the breakdown voltages and electric fields are close to each other. This may be the result of the random nature of air breakdown.

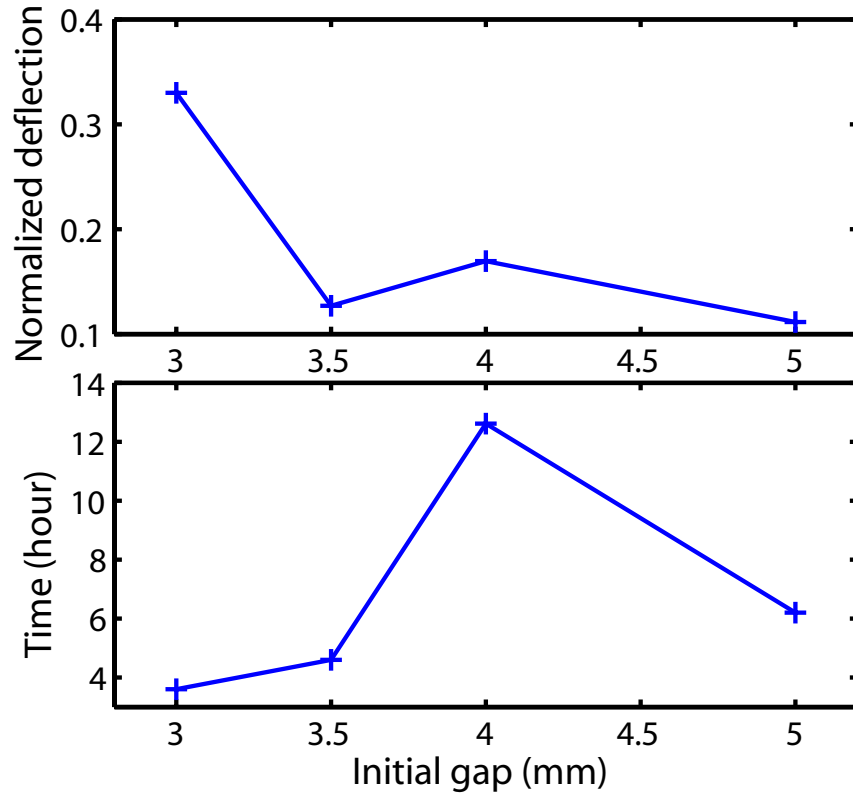


Figure 4.9: The elapsed time when air breakdown happens and the corresponding normalized deflection are plotted versus the initial gap.

4.7.4 Cessation

With an even larger gap, the cantilever will simply stop at certain position and stay there. No air breakdown happens even after a long time. At the initial gap of

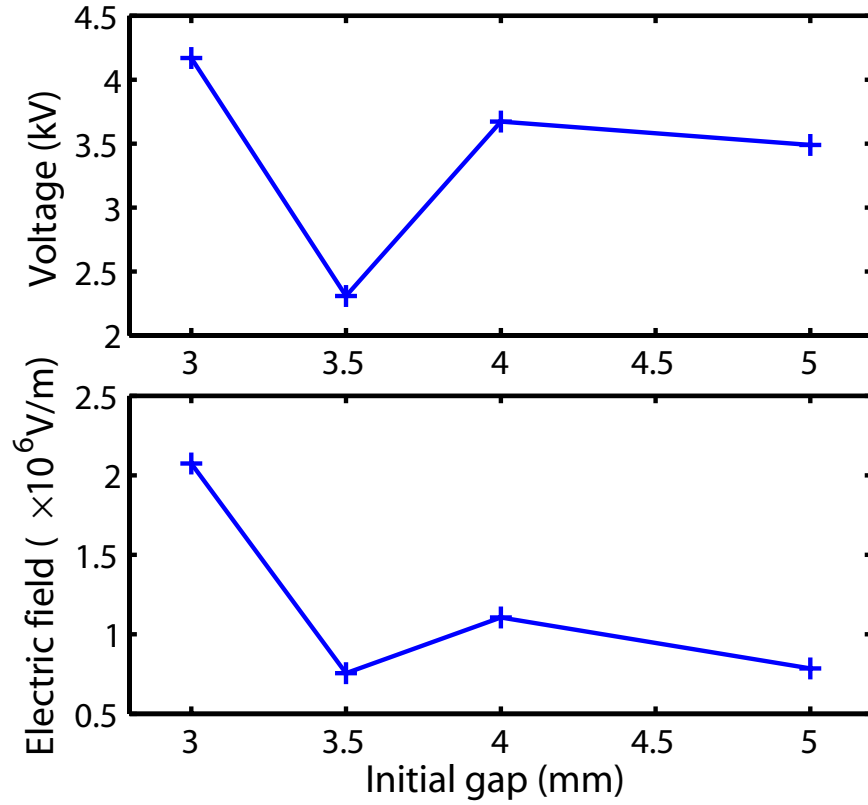


Figure 4.10: The estimated breakdown voltage and corresponding electric field are plotted against the initial gap.

6 mm, the sample cantilever moved about $185 \mu\text{m}$ in the first 2 hours and moved about another $70 \mu\text{m}$ in the following 6 hours. Then it stopped there. Within 16 hours, no further movement or other phenomenon was observed. At the stop position, the estimated voltage is 1.8 kV . Further increasing the gap results in even smaller movement with cessation.

4.7.5 Pseudo Continuous Reciprocation

In principle if the source can provide sufficient current, immediately after the cantilever is released a following reciprocation could happen so that a continuous

operation is realized. However given the source available such an operation has never been observed even with a very small initial gap. What has been observed is that the cantilever may vibrate when it is released. If the vibration can sustain long enough so that a reciprocation happens again before the vibration stops, a continuous vibration of the cantilever can be observed. For the reciprocation process it is still a normal reciprocation.

4.8 Constant Current Approximation

To obtain Equation 3.9 and other equations to characterize the cantilever in Section 3.4, an infinite R is assumed. This is equivalent to take R as infinity in Equation 3.2, which can be now written as

$$\alpha I - \epsilon_0 A \frac{\partial}{\partial t} \left(\frac{V}{d} \right) = 0 \quad (4.2)$$

Since a constant α is also assumed for a given initial distance, this equation shows a constant current driving scheme. Although not all the current from the source is collected, the effective collected current αI is a constant. So the electromechanical model takes an mean constant current approximation. All the leakages, including ionization, air gap leakage, secondary electrons and backscattered electrons, are including in the α parameter. The gross effect of these leakages gives a constant current. The good fit of the model to the experiment results proves the validity of the constant current approximation.

For an ideal parallel plate electrostatic actuator under constant current driving, no pull-in is expected. However for a real parallel plate device because of parasitic capacitance, pull-in can happen when the cantilever deflection reaches x_{pi} [51]:

$$x_{pi} = \frac{d_0}{3} \left(1 + \frac{C_0}{C_p} \right) \quad (4.3)$$

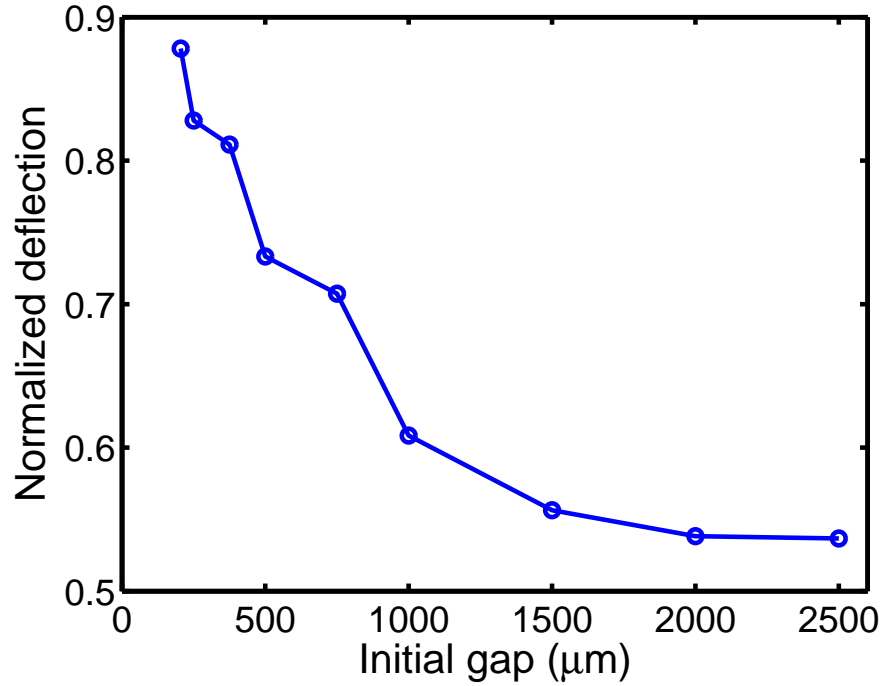


Figure 4.11: Shown is the the normalized pull-in deflection versus the initial gap.

where C_0 is the parallel-plate capacitance, and C_p is the parasitic capacitance, which for the cantilever mainly comes from the fringing field capacitance. When the initial gap d_0 becomes larger, relatively to C_0 , C_p increases. Therefore pull-in will happen at a relatively smaller deflection. This is verified by Figure 4.11 which shows the normalized pull-in deflection x_{pi}/d_0 versus the initial gap.

Apparently if the constant current approximation is valid at any initial gap, the cantilever would not stop after certain movement as observed in air breakdown and cessation cases. For those regimes, the current collected must be decreasing when the cantilever bends. Eventually the current collected is in balance with the leakage so that the cantilever stops. For power generation a cantilever should not operate in these regimes since most of the energy is lost due to leakage.

4.9 Leakage Mechanisms

It is preferred to collect as many charges as possible to achieve shorter reciprocation cycle and higher conversion efficiency. However due to leakage not all the charges are collected. There are several mechanisms contribute to the leakage as discussed below.

4.9.1 Radiation Configuration Factor

Due to the random nature of nuclear decay process, the angle distribution of the electron emission is uniform. Although a plate source as used in the experiments may alter this distribution a little due to self absorption it is fairly accurate to assume a uniform distribution of the emitted electrons in the semi-sphere space on the radioactive side of the source plate. Given the setup of the cantilever and the source, as the cantilever moves away from the source, less solid angle is covered by the cantilever which results in current loss. This is illustrated on the left side of Figure 4.12. The loss from only this geometric effect can be calculated using radiation configuration factor, also called view factor. The radiation configuration factor F_{12} is defined as the fraction of diffusely radiated energy leaving surface 1 that is incident on surface 2. It can be calculated as illustrated on the right side of Figure 4.12 [52]:

$$F_{12} = \frac{1}{A_1} \int_{A_1} \int_{A_2} \frac{\cos\theta_1 \cos\theta_2}{\pi r^2} dA_2 dA_1 \quad (4.4)$$

where A_1 , A_2 are the two surfaces. For two rectangular surfaces, such as the cantilever and the radioisotope source, an analytical form is available for the view factor calculation and is presented in Appendix B.

The current collected by the sample cantilever, which will be referred as *col-*

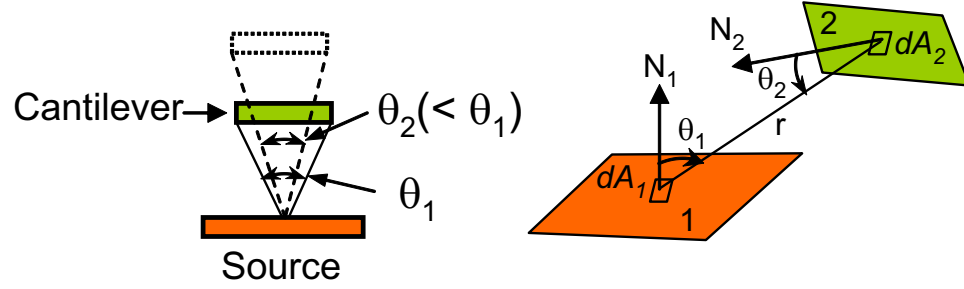


Figure 4.12: On the left it illustrates the solid angle coverage decreases as the gap increases. On the right, it illustrates the calculation of radiation configuration factor.

lector current, was measured with a Keithley 4200 semiconductor analyzer. The current measurement was done under zero bias condition that is similar to the radioactive source current measurement, i.e., the source and the chamber is grounded and the collector is hold at zero bias voltage. In this way the effect of ionization current should be minimized. Figure 4.13 shows the collector current keeps decreasing as the distance between the source and the cantilever increases. The calculated curve is based on the view factor only. It follows the trend very well. The current measured includes the effect of secondary electrons, which explains the difference from the calculated value.

4.9.2 Secondary Electrons

When the electrons hit the surface of the cantilever, secondary electrons including backscatter electrons will generate. The real secondary electrons which comes out from the cantilever surface will be called true secondary electrons later. The backscattered electrons become a leakage current since they have enough energy to go back to the source. The true secondary electrons also contribute a leakage

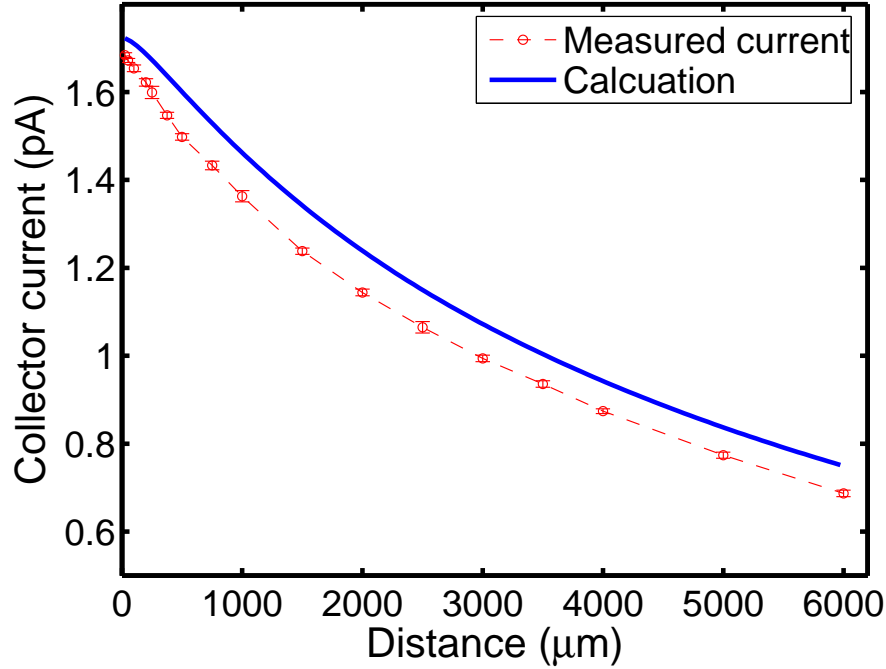


Figure 4.13: The measured collector current under zero-bias condition is plotted together with the calculated value which takes into account only the radiation configuration factor.

current, especially when a voltage builds up across the capacitor to attract them back to the source. Even under zero bias, those secondary electrons that have enough energy to reach the source contribute to the leakage. In the collector current measurement, the current is 0.687 pA at a 6 mm gap. However the expected current is $5.75 \times 0.13 = 0.748 \text{ pA}$, where 0.13 is the view factor and 5.75 pA is the source current. The difference should mainly result from the secondary electrons, as the view factor has been taken into account and there should be little ionization current under zero bias. Therefore, the estimated secondary electron leakage current is $(0.748 - 0.687)/0.748 = 8.2\%$ of the expected value. In Figure 4.13 the calculated collector current is plotted without considering the secondary elec-

trons. The recalculated current is plot together with the measurement result in Figure 4.14. It can be seen the predicted value now is closer to the measurement. There is still some difference, especially at small gaps. This might be caused by the secondary electrons generated at the source surface, which then reach the collector and compensate the leakage.

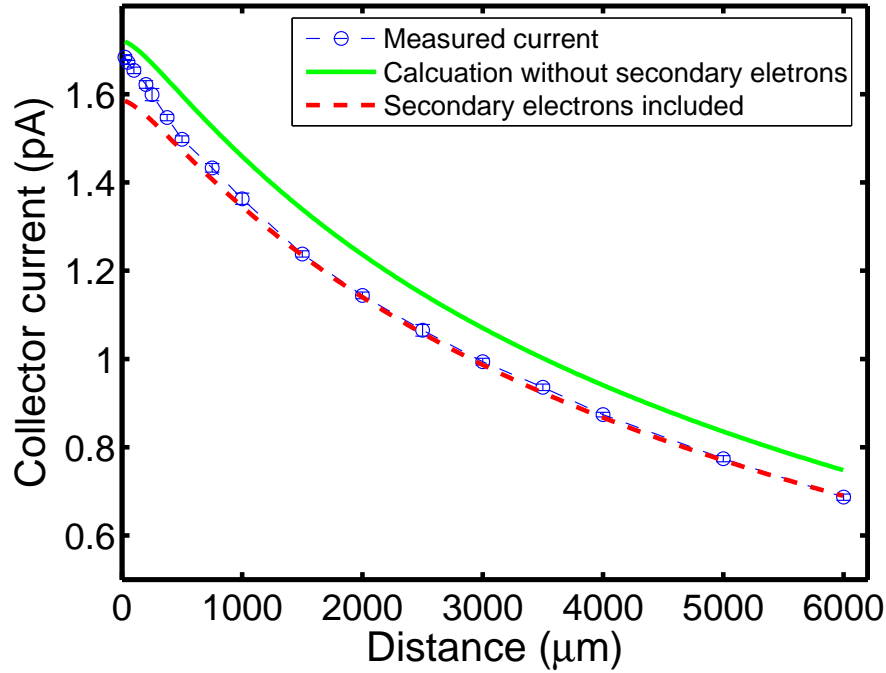


Figure 4.14: The calculated collector current with the consideration of secondary electrons is plotted to compare with the measured value.

Since different materials have different secondary electron yields, it would be beneficial to use a material that generates less secondary electrons. For backscattered electrons it is sort of straightforward since generally lighter atoms generate less backscattered electrons until the atom number gets really big, where under most circumstances such materials are rarely available. It is more complicated with true secondary electron generation since true secondary electron yield depends on

the energy of the incident electron, and electrons emitted from a beta sources is not mono-energetic but have a wide energy spectrum. However, secondary electron yield of most metals usually has its maximum around several hundreds of eV and drops significantly at high incident energy [53]. Considering that the average energy of Ni-63 is 17 *keV*, the percentage of electrons with energy less than 1 *keV* should be very small. It is reasonable to argue that the true secondary electrons should not play a major role in the leakage.

Experiments have been done to investigate the performance of different metals. First, collectors of different metals with the same size were made for zero bias current measurement. The result is plotted in Figure 4.15. With Au and W collectors the currents are significantly lower than with other metals. This should mainly be due to the large portion of backscattered electrons generated. Further, cantilevers with the same dimensions were fabricated and tested at the same initial distance of 15 μm with the NRD source. The extracted α that reflects the current collection efficiency is normalized against the α of copper and plotted versus atomic number in Figure 4.16. Again Au is poor in performance. However it is interesting to notice that although zero bias current favors Al, the actual performance of Al is worse than Cu. This implies that the fine detail of generated secondary electrons affects other leakage mechanism and causes the inconsistency. Based on the two results, Cu is a good choice for collector as it performs well and easy to obtain and process.

One more experiment was done with three cantilevers and the results are listed in Table 4.3. The cantilevers have the same stiffness and same width so that the reciprocation period will directly reflect the charge collection. The second column of Table 4.3 shows the reciprocation periods of the Cu and Al cantilevers

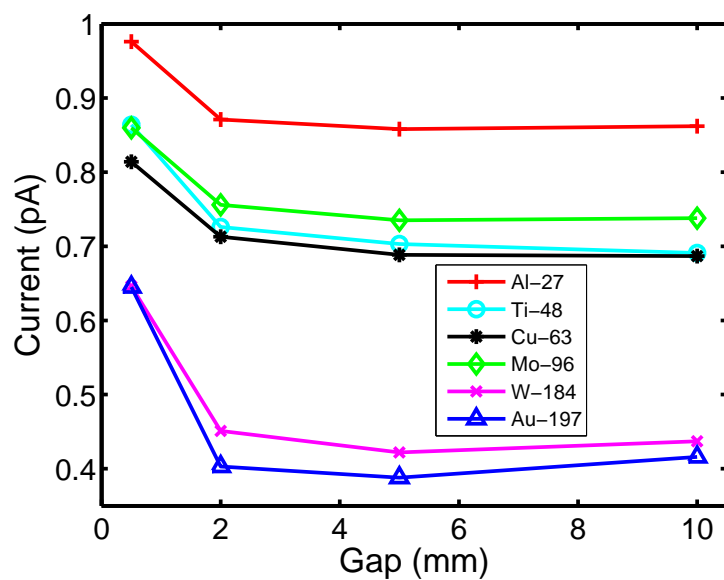


Figure 4.15: The collector current of collectors made of different metals but with the same size is measured.

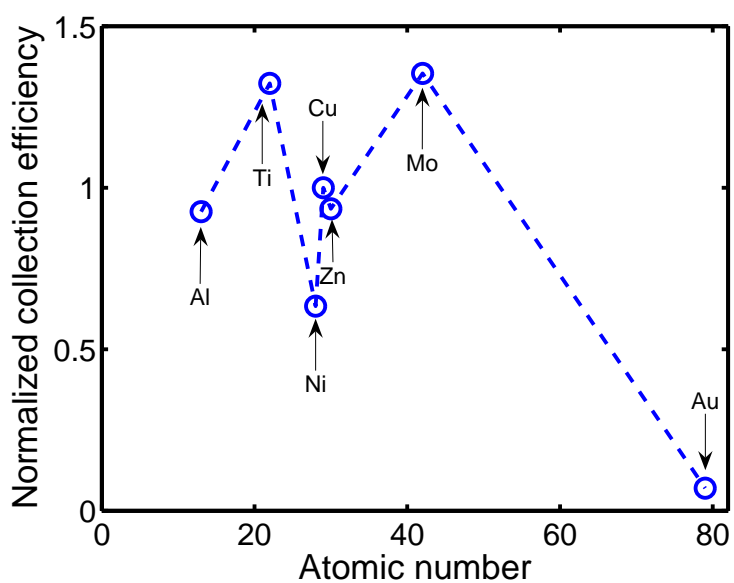


Figure 4.16: Collection efficiency normalized against that of Cu is plotted versus atomic number.

Table 4.3: Three cantilevers made of different materials but with same width and stiffness are compared at different initial gaps. Shown are the reciprocation periods.

Material	$d_0 = 100 \mu m$	$d_0 = 500 \mu m$	$d_0 = 3 mm$
Al	3.4 minutes	10.1 minutes	
Cu	3.3 minutes	8.8 minutes	2.05 hours
Si		5.2 minutes	2.02 hours

at an initial gap of $100 \mu m$. Cu performances slightly better than Al. When the gap becomes $500 \mu m$, it is seen that Cu is better than Al and Si is better than Cu. However when the gap further increases to $3 mm$, there is no much difference between Si and Cu. This can be explained that at larger gaps the ionization current dominates the leakage because higher voltage is generated and larger gaps provide more space for ionization. These results show that for small gaps, different materials performance differently, but for large gaps the difference becomes smaller. Nevertheless it is always better to use a material that generates less secondary electrons.

4.9.3 Ionization

The emitted electrons, backscattered electrons and secondary electrons can all ionize the air between the gap. Also the air has some naturally generated ions. Those ions collides with air molecules and may generate more ions. Because of this avalanche effect ionization current can be significant. The situation becomes worse when voltage builds up across the air-gap capacitor. Usually many generated ions

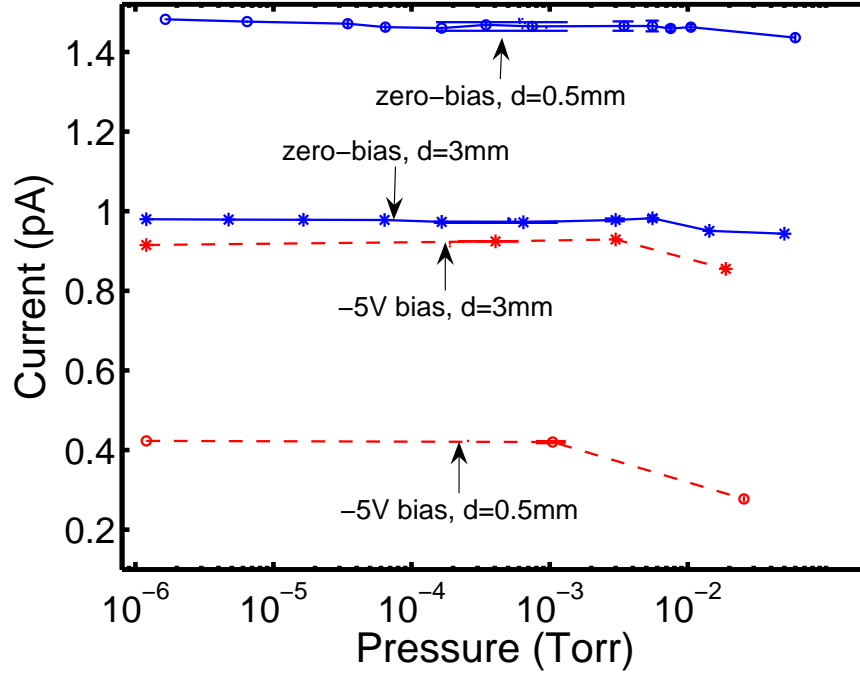


Figure 4.17: The collector current under zero bias or -5 V is measured versus pressure at two locations.

recombine quickly. But if there is an electric field, the positive ions and electrons move in opposite directions and can gain more energy on the way. Therefore the avalanche effect becomes more significant. Under the voltage electrons will go to the source and positive ions to the cantilever, which generate a leakage current.

Figure 4.17 shows the measured collector current under different pressure at two different gaps. Zero-bias and a bias of -5 V are used. It can be seen that the zero-bias current drops as the pressure increases, while the decrease is very small in the pressure range of $1 \times 10^{-6} \sim 1 \times 10^{-3}\text{ Torr}$. The decrease is expected since the higher the pressure, the more the electrons act with the air molecules resulting in more loss. The -5 V biased current illustrates how much ionization leakage can be. As seen from the figure, even at such a low bias, a great portion of current is

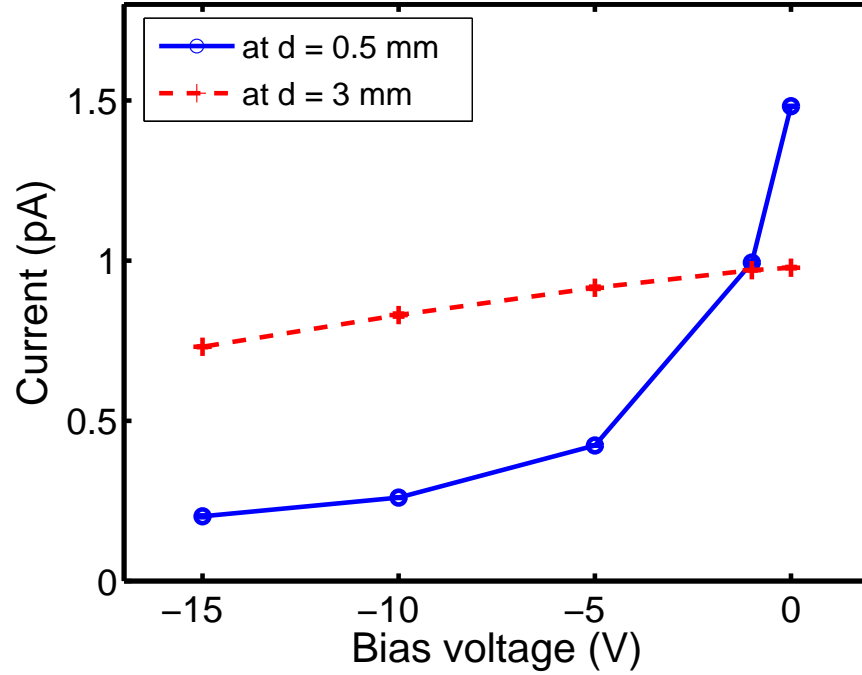


Figure 4.18: Shown is the collector current versus bias voltage. Measurements are taken at two different gaps.

lost. Figure 4.18 shows the current measurement done under $P = 1.2 \times 10^{-6} \text{ Torr}$ with different bias voltages and at two locations. The current drops as voltage increases. This should be due to the fact that more ionization current is collected with a higher bias voltage. It also illustrates that at the voltage level used a larger gap has smaller ionization leakage. This may result from the fact that at a larger gap ions have more chances to recombine so that less leakage is generated.

Figure 4.19 shows the total electron ionization cross sections of N_2 and O_2 [54] versus incident electron energy. They are very close to each other so N_2 data will be used for air. The cross section of N_2 has a maximum of 2.6 \AA^2 at 95 eV and at 17 keV it is 0.085 \AA^2 . The number of ionized molecules between the source and

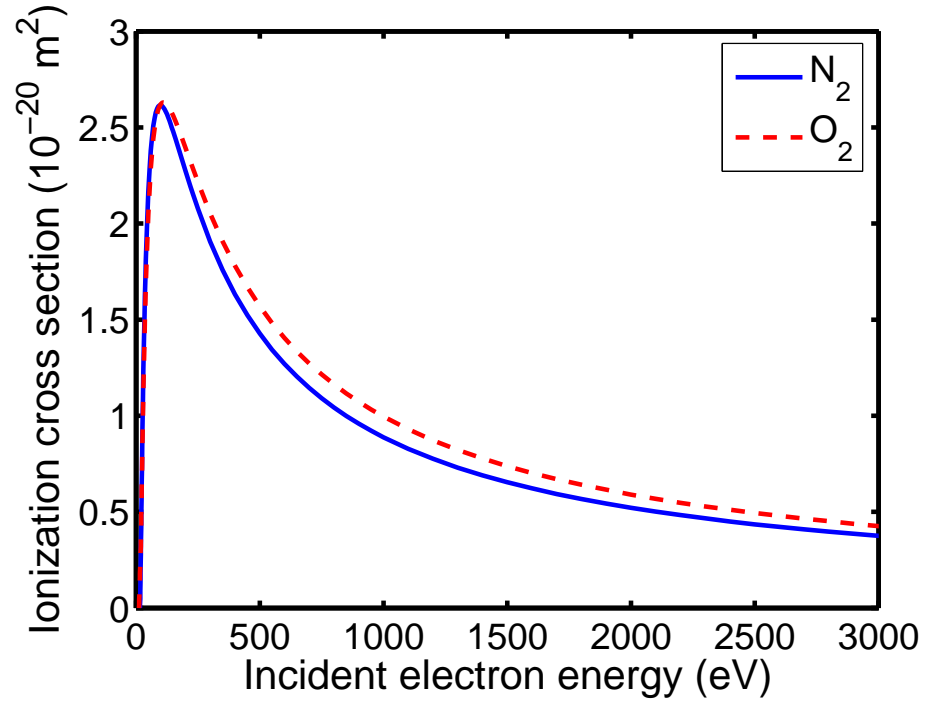


Figure 4.19: The total electron ionization cross sections of N_2 and O_2 are plotted. Data are from Reference [54].

the cantilever per second, n_i , can be calculated as

$$n = \sigma N n_{air} d \quad (4.5)$$

where σ is the ionization cross section, N is the effective activity of the source, n_{air} is the number density of air, and d is the gap. n_{air} can be calculated using:

$$n_{air} = \frac{P}{kT} \quad (4.6)$$

with P being the pressure, T the temperature and k the Boltzmann constant. It is assumed that σ does not change while the electron travels through the gap, which will be justified later. At $P = 2.25 \times 10^{-6} \text{ Torr}$ and room temperature, with 17 keV electrons, n_i is calculated to be 7/s. Even with the maximum σ it

only generates 201/s. Those numbers, which justify the use of a fixed σ , are much smaller compared to the leakage observed from the experiments. This implies that the avalanche effect must take place.

Besides leakage, another disadvantage of ionization is that it helps the breakdown. As shown in Figure 4.9 and 4.10, the observed air breakdown happened at only 2.3 kV at a gap of 3 mm for the $d_0 = 3.5$ mm case while the pressure is at 2.25×10^{-6} Torr. According to the Paschen curve [55], the breakdown voltage is too small for such pressure and gap. Ordinarily the air breakdown relies on naturally generated ions, which have a density of $9.5 \text{ cm}^{-3}\text{s}^{-1}$ in atmosphere [55]. Since now the radioisotope is an ionization source, extra ions are generated and the air breakdown becomes easier.

4.10 Efficiency and Energy Output

The efficiency also varies as the initial gap changes. Figure 4.20 illustrates this. Generally a larger distance offers higher efficiency as Equation 3.22, which is rewritten below, predicts.

$$\eta = \frac{\alpha q}{E_e} \sqrt{\frac{k d_0^3}{8 \epsilon_0 A}} \quad (4.7)$$

However Equation 4.7 also has α in it. As distance increases α tends to decrease, as the dashed line shows. After certain distance, 3 mm for the sample cantilever, where the air breakdown begins to happen, α becomes low enough to offset the advantage offered by the large distance, which means high voltage, so that the efficiency begins to drop.

The energy output from the cantilever is $k d_0^2/2$. Hence, to obtain a higher output a stiffer cantilever, i.e., larger k , or a larger initial gap can be used. And it is preferred to start at a larger initial gap due to the quadratic relationship.

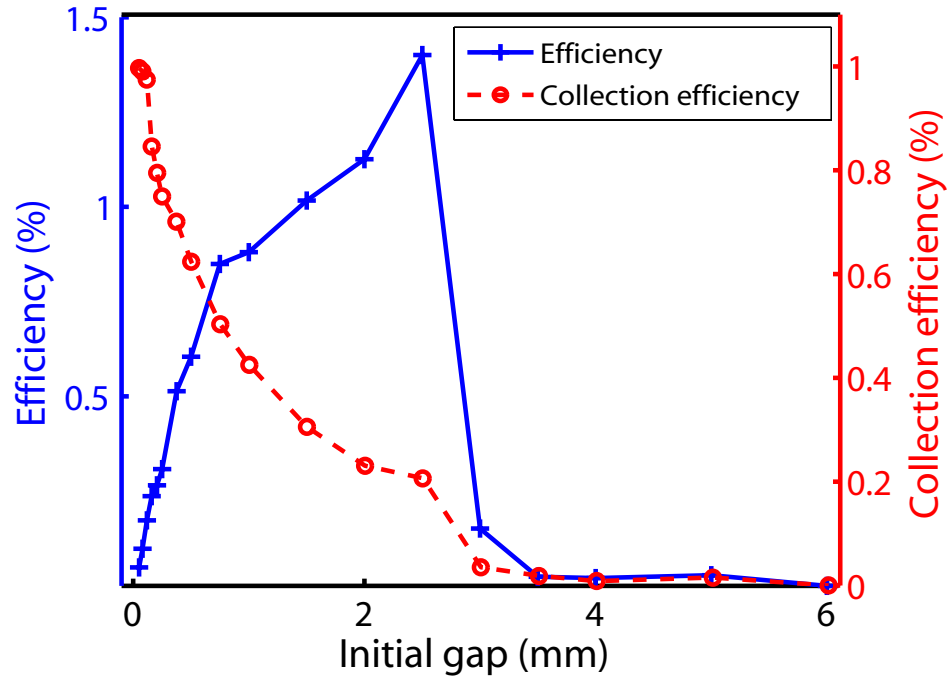


Figure 4.20: The energy conversion efficiency and the current collection efficiency are plotted against initial gap.

Equation 4.7 also shows a larger k or larger d_0 helps to obtain a higher efficiency and a larger d_0 is more advantageous since the efficiency is proportional to $d_0^{3/2}$ but only to $k^{1/2}$. In conclusion, while increasing the stiffness of the cantilever or increasing the initial gap results in both larger energy output and better efficiency, increasing the initial gap is more effective. However, for a given device there is a tradeoff between the energy output and the reciprocation cycle. Because although larger initial gap or stiffness results in higher energy output, it also takes longer for the reciprocation.

From Equation 4.7 it is also seen that for better efficiency a larger α is desired. This is because as more electrons are collected the efficiency is higher. A smaller source area benefits the efficiency as well. An interesting observation is that a

radioisotope source emitting lower average energy electrons offers better efficiency. This is due to the fact that it is easier to generate a small voltage across the air-gap capacitor than a high voltage.

The average power P of the cantilever is:

$$P = \frac{kd_0^2}{2T} \quad (4.8)$$

Substituting Equation 3.13 for T gives

$$P = \alpha I \sqrt{\frac{kd_0^3}{8\epsilon_0 A}} \quad (4.9)$$

For a given source, a higher efficiency results in a higher average power. Since I is area dependant, a larger source area also helps to increase the average power. Equation 4.9 unveils another fact that for a given size source, a larger current will offer better average power. This means a larger unit area current, i.e, larger unit area activity. Therefore a different radioisotope with a larger specific activity can be used, or improve the source manufacture so that a higher activity-area-density is obtained.

Minimizing leakages is essential for achieving high efficiency. Vacuum pressure is very important for this purpose. Higher vacuum is always beneficial. To compensate the radiation configuration factor, large collectors can be used. However if the reciprocation period needs to be kept the same, the collector should be placed only near the tip of the cantilever so that the stiffness will not be altered significantly. The material of the cantilever or the collector should be chosen to minimize the secondary electron effect. Besides improving the vacuum, a gas hard to ionize may be used as a fill-in gas for less ionization.

As a summary, Table 4.4 lists some design parameters for better performance of the cantilever.

Table 4.4: The design parameters for better performance are listed. \uparrow means increase, \downarrow means decrease and - means irrelevant.

Performance	Cantilever stiffness (k)	Initial gap (d_0)	Electron energy (E_e)	Radioisotope specific activity	Source area (A)
Larger force output	\uparrow	\uparrow	-	-	-
More energy output	\uparrow	\uparrow	-	-	-
Shorter cycle	\downarrow	\downarrow	-	\uparrow	\uparrow
Higher efficiency	\uparrow	\uparrow	\downarrow	-	\downarrow
Higher average power	\uparrow	\uparrow	-	\uparrow	\uparrow

4.11 Scalability

The electromechanical model does not predict there is a size limitation of the cantilever. Scalability of the device is feasible. The spring constant of a cantilever can be calculated as:

$$k = \frac{EWH^3}{4L^3} \quad (4.10)$$

where E is the Young's modulus of the material, L, W, H are the length, width and height respectively. The radioisotope has the same width as the cantilever to be consistent with the parallel plate capacitor approximation. So the area A can be written as:

$$A = WL_s \quad (4.11)$$

where L_s refers to the length of the radioisotope. Combining Equation 3.13, 4.10 and 4.11, it results in:

$$T = \frac{\sqrt{2\epsilon_0 d_0 k/A}}{\alpha I/A} = \sqrt{\frac{\epsilon_0 d_0 E H^3}{2L_s L^3}} / \alpha i \quad (4.12)$$

with i being the current density of the radioisotope thin film. So once the radioisotope and the material of the cantilever are chosen, the dimensions of cantilever and the size of the radioisotope source can be designed to achieve a reasonable reciprocation period. For example, a silicon cantilever with dimensions $500 \mu m \times 100 \mu m \times 2 \mu m$ can finish one cycle in about 7 minutes with a $200 \mu m \times 100 \mu m$ ^{63}Ni source for an initial distance of $2 \mu m$. This is assuming the same unit area activity ($0.01 \text{ mCi}/mm^2$) of the ^{63}Ni source used in the experiment. One issue is that $2 \mu m$ thick silicon is not thick enough to capture most of the electrons. A solution to it is to electroplate a metal layer at the tip of the cantilever that is thick enough for electron capture. The added mass should not affect the spring constant much since the metal layer is placed at a location of low strain. If the activity per unit area is increased by a factor of 10, which is possible because given the specific activity of ^{63}Ni it theoretically can be $7 \text{ mCi}/mm^2$, and the spring constant is decreased by reducing polysilicon thickness or increasing length, one should get much shorter reciprocation. For example, using a cantilever with dimensions of $1 \text{ mm} \times 100 \mu m \times 1 \mu m$ and a $200 \mu m \times 100 \mu m$ source with a unit area activity of $0.1 \text{ mCi}/mm^2$, one should obtain a reciprocation period of 5 seconds for a $2 \mu m$ gap. Even though the output mechanical energy is only 9.5 fJ , it is important to remember that the same energy would be required to move this cantilever by any other means.

A micro scale cantilever was fabricated to verify the scalability. Figure 4.21 shows a picture of the cantilever. It is made of low stress Si_3N_4 thin film with

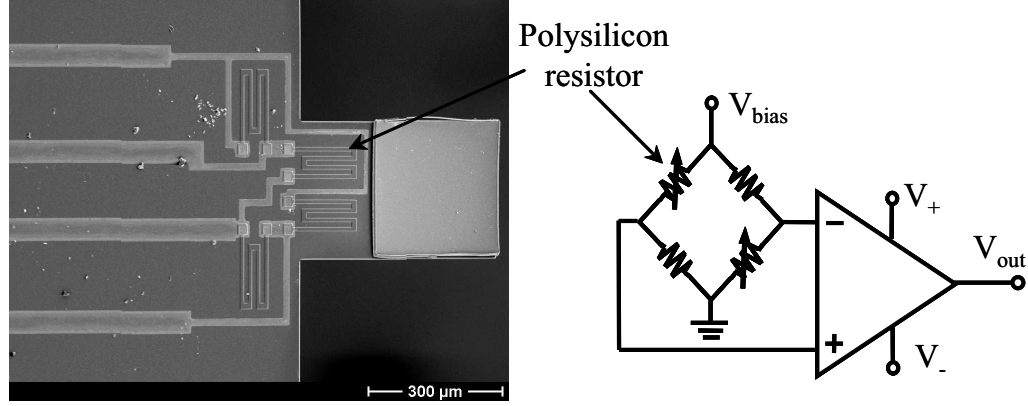


Figure 4.21: Shown is a picture of a Si_3N_4 micro cantilever. Its dimensions are $500\ \mu m \times 300\ \mu m \times 1.7\ \mu m$. At the tip area of the cantilever a layer of $1\ \mu m$ Al is evaporated. Four polysilicon resistors form a Wheatstone bridge on the cantilever for monitoring the deflection. The measurement circuit is shown on the right side.

dimensions of $500\ \mu m \times 300\ \mu m \times 1.7\ \mu m$. To monitor the bending of the cantilever, four polysilicon resistors forming a strain gauge are integrated on the cantilever as shown in the picture. The four resistors are connected as a Wheatstone bridge and the signal is sent to an instrumentation amplifier. Figure 4.22 shows how the cantilever bends at an initial gap of $1\ \mu m$. The reciprocation period is 32 seconds. The bending measured by the strain gauge is shown as circle and by directly optical measurement is shown as cross. The curves are fitted with the model. The two measurements agree with each other.

4.12 Summary

Self reciprocation is realized with a copper cantilever. The experimental results verify the electromechanical model. The effect of initial distance on the performance of the cantilever is extensively investigated and different operation regimes

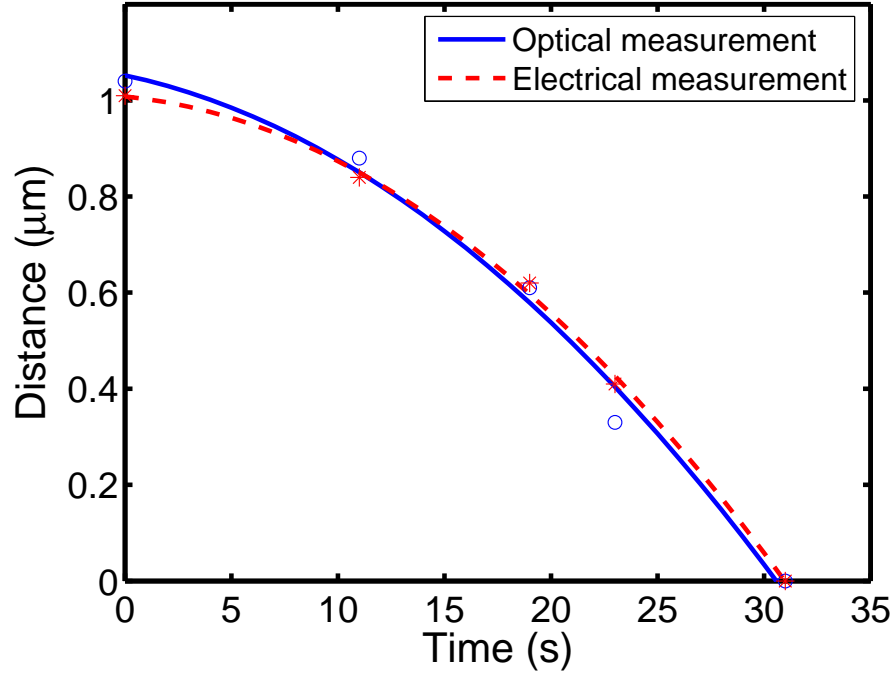


Figure 4.22: The distance versus time curve of the micro cantilever is shown. The deflection was measured by both the optical method and the output from the polysilicon resistors.

are recognized. As the initial distance increases, the cantilever operates from normal reciprocation regime to pull-in, then to air breakdown and finally to cessation. Current leakages due to view factor, secondary electrons and ionization current are identified and means to prevent them are discussed. Improvement of energy conversion efficiency is essential for the device performance. How to achieve higher efficiency is studied. The scalability to MEMS scale is found feasible based on the electromechanical model and verified with a micro cantilever.

Chapter 5

Radio Frequency Pulse Generation

The material of the cantilever is not necessarily limited to pure metal or other conductive materials. As long as there is a conductive layer to collect charges and to realize charge neutralization, other materials can be incorporated into the cantilever. When using a dielectric beam, besides self reciprocation, a radio frequency (RF) pulse is generated at the end of the reciprocation cycle. The realization of RF pulse generation provides the possibility for self-powered RF transmission, which may enable self-powered sensor networks.

5.1 Radioactively Powered RF Pulse Generation: Theory

Figure 5.1 illustrates the mechanism of RF pulse generation. A piezoelectric/dielectric PZT (lead zirconate titanate) beam is used as the cantilever. It has gold electrodes on both sides. The PZT beam itself is a capacitor C_1 . The electrode facing the radioactive source forms a capacitor, C_2 , together with the source. The parasitic capacitor C_3 formed by the source and the other electrode of the cantilever closes the loop. While the PZT cantilever collects electrons from the source, the PZT capacitor is charged up at the same time. Therefore a voltage is built up across the PZT capacitor. The self-reciprocation also applies to the PZT cantilever. At the end of the reciprocation cycle, the cantilever touches the source and the charges on the electrode facing the source suddenly disappear due to charge neutralization. This sudden change of charge distribution on one electrode of the PZT capacitor results in a voltage change across the PZT, and induces a displacement current. This excites the *dielectric* RF mode of the PZT plate and generates a RF pulse.

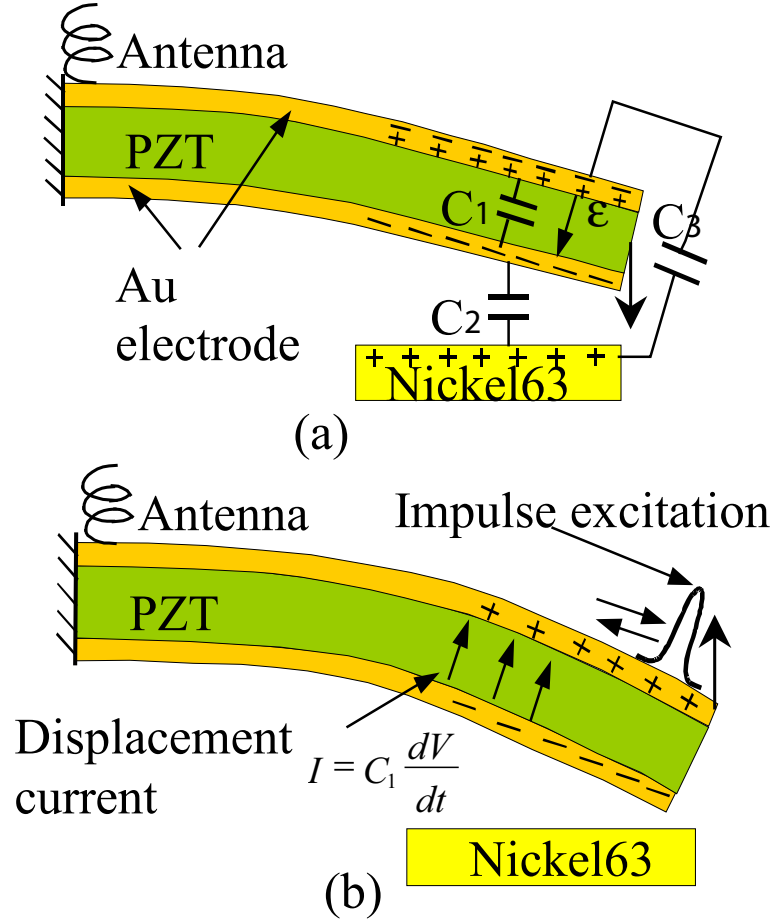


Figure 5.1: (a) The capacitance of the PZT cantilever builds up an electric field as the charges are built on the two electrodes. (b) The sudden shorting of the charge on one side results in a sudden release of the electric field and hence the voltage across the cantilever. This results in a displacement current that excites the dielectric RF mode of the PZT.

To detect the RF pulse, the PZT cantilever is connected to an oscilloscope with a RG58/U coaxial cable. Figure 5.2 shows the circuit connection. The frequency of the generated RF pulse can be roughly estimated by taking the PZT cantilever as a dielectric waveguide. The impedance looking to the right (the PZT) side of

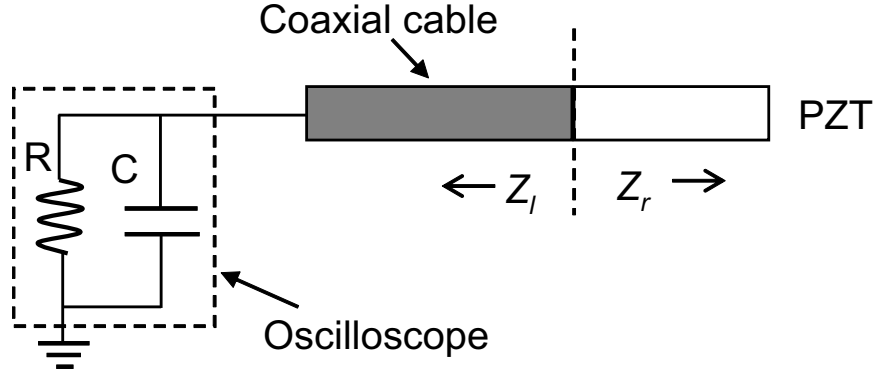


Figure 5.2: The PZT cantilever is connected to an oscilloscope for RF pulse detection with a coaxial cable.

the interface of the PZT cantilever and the coaxial cable is:

$$Z_r = \frac{Z_p \cos k_p l_p}{j \sin k_p l_p} \quad (5.1)$$

since the far end of the PZT cantilever presents an open-circuit boundary condition.

The impedance looking to the left (the oscilloscope) side is:

$$Z_l = Z_c \frac{\frac{1}{j\omega C} \cos k_c l_c - j Z_c \sin k_c l_c}{Z_c \cos k_c l_c - \frac{1}{\omega C} \sin k_p l_p} \quad (5.2)$$

where Z_p, Z_c are the characteristic impedance of the PZT cantilever and the coaxial cable, respectively; k_p, k_c are the wave numbers, l_p, l_c are the PZT and the coaxial cable lengths, and ω is the angular frequency of the propagated wave. C is the input capacitance of the oscilloscope that is 13 pF . At the frequency of the RF signals detected ($> 20 \text{ MHz}$), the input resistance R ($1 \text{ M}\Omega$) of the oscilloscope is ignored when compared to the impedance of the input capacitance. The propagated wave should have a frequency that makes Z_r and Z_l the same. Therefore, combining Equations 5.1, 5.2 results in:

$$Z_c \tan\left(\frac{\omega l_p}{V_p}\right) + Z_c^2 \omega C \tan\left(\frac{\omega l_c}{V_c}\right) \tan\left(\frac{\omega l_p}{V_p}\right) = Z_c Z_p \omega C - Z_p \tan\left(\frac{\omega l_c}{V_c}\right) \quad (5.3)$$

where the relation $k = \omega/V$ with V the phase velocity is used. The characteristic impedance Z_c of RG58/U coaxial cable is 53.5Ω . The characteristic impedance of the PZT cantilever can be calculated as [56]:

$$Z_p = \frac{a}{b} \sqrt{\frac{\mu}{\epsilon}} \quad (5.4)$$

with a the thickness of the PZT cantilever and b the width. $\mu = \mu_0$ is the permeability and ϵ is the permittivity, which is $1200\epsilon_0$ for the PZT at room temperature. Equation 5.3 can be solved graphically to obtain the frequency of the RF signal.

5.2 RF Pulse Generation: Experiment

The experimental setup as shown in Figure 5.3 is very similar to the one for the copper cantilever. The only difference is that two wires are soldered to the electrodes of the PZT cantilever, which are then connected to an oscilloscope with a coaxial cable. The dimensions of the PZT cantilever $2 \text{ cm} \times 3 \text{ mm} \times 100 \mu\text{m}$.

At the end of a reciprocation cycle, a RF pulse is generated and captured by the oscilloscope. Figure 5.4 shows a typical pulse when a 2 feet long coaxial cable is used. The frequency spectrum of the signal is shown in Figure 5.5. Apparently

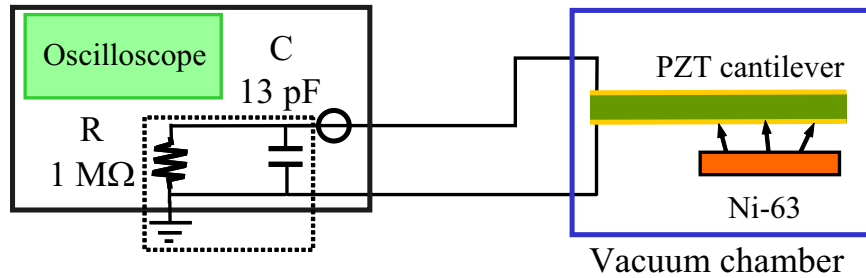


Figure 5.3: The experimental setup for detecting the RF pulse generated by a radioisotope-powered PZT cantilever is shown.

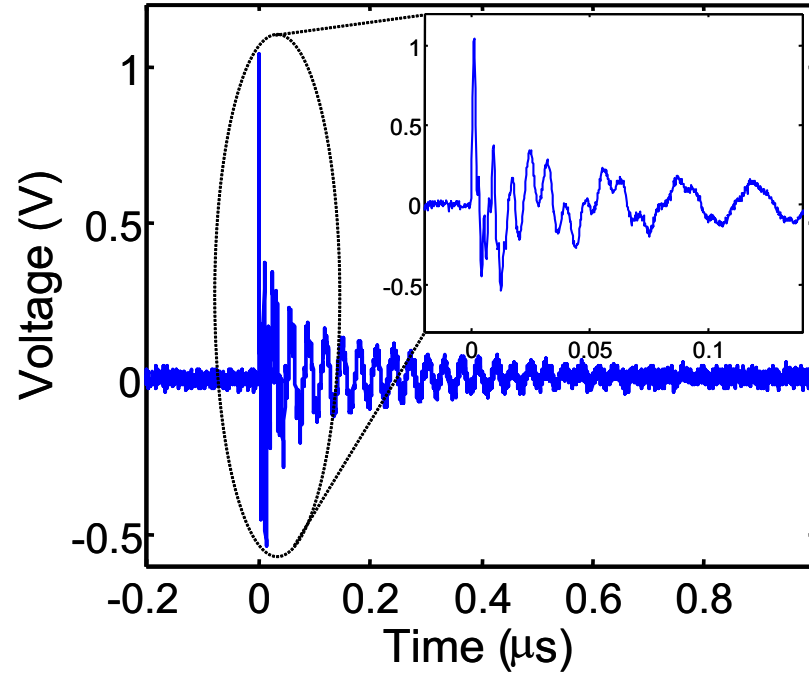


Figure 5.4: The RF pulse obtained with a 2 feet long cable is shown. The closeup shows the initial pulse.

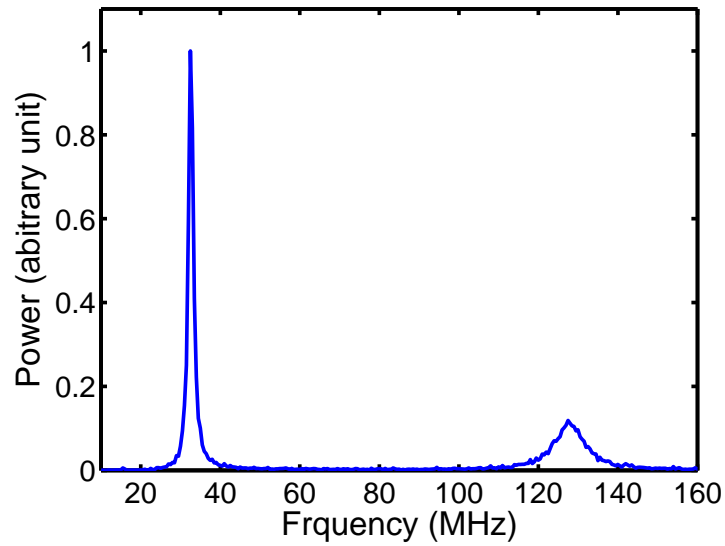


Figure 5.5: Shown is the frequency spectrum of the pulse in Figure 5.4. There are two frequency components, one is at 32.5 MHz , the other one is at 127.5 MHz .

there are two main frequency components. One is at 32.5 MHz . This frequency is the frequency of the oscillation signal which is readily seen in Figure 5.4. The other frequency of 127.5 MHz is not that obvious but the closeup in Figure 5.4 which shows the initial pulse proves the existence of this higher frequency. This initial frequency is from the waveguide mode excitation while the oscillation frequency of 32.5 MHz comes the electrical resonance of the system, including the cantilever, the coaxial cable and the oscilloscope.

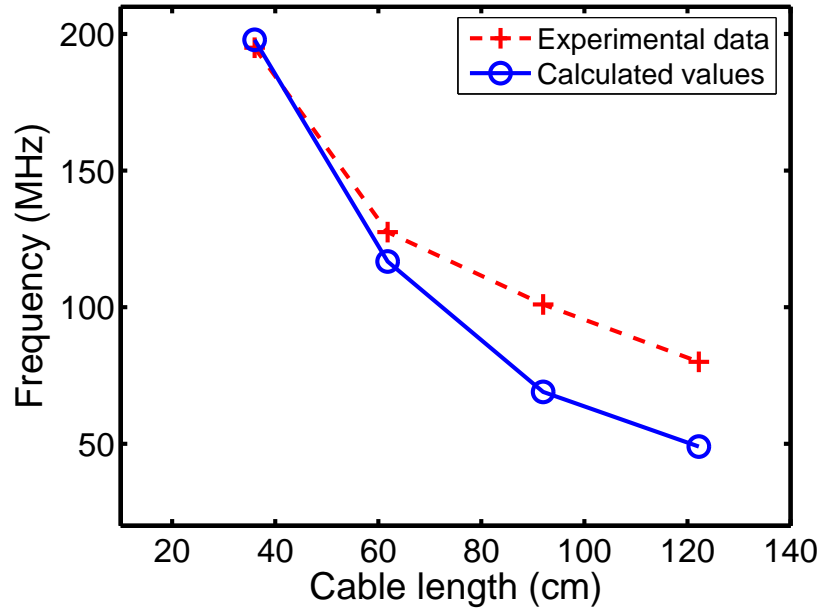


Figure 5.6: The pulse frequency varies as the cable length changes.

Equation 5.3 predicts that with cables of different lengths different frequencies will be generated. This is confirmed by the experimental results where four coaxial cables with the lengths from 1 foot to 4 feet are used. All the detected signals look similar to the waveform shown in Figure 5.4 that has an oscillation waveform with an initial pulse of a different frequency. Figure 5.6 shows the measured initial frequencies as compared to the predicted waveguide excitation frequencies

by Equation 5.3. The predicted and measured frequencies agree well.

The electrical system composed of the PZT cantilever, the coaxial cable and the oscilloscope has its own resonance frequency. This resonance frequency shifts if coaxial cables of different lengths are connected with the cantilever. Figure 5.7 shows the measurement setup of the resonance frequency. A HP4194 impedance analyzer is used and a 13 pF capacitor is employed to simulate the oscilloscope. The resonance frequency is high enough for ignorance of the 1 $M\Omega$ input resistance of the oscilloscope. The measurement results plotted in Figure 5.8 show that the resonance frequency, where the peak is, changes with the cable length. Hence, it is expected to see a different oscillation frequency with a cable of different length. This is confirmed by the waveforms generated with the four cables. The oscillation frequencies measured from the waveforms are plotted together with the resonance frequencies measured by the impedance analyzer in Figure 5.9. A good match between the two measurements is observed.

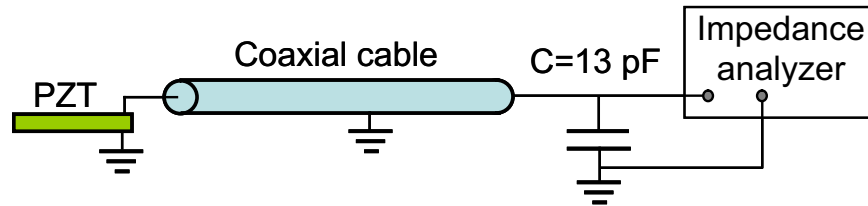


Figure 5.7: Shown is the setup to measured the resonance frequency of the system composed of the PZT cantilever, the coaxial cable and a capacitor which simulates the oscilloscope.

The emitted RF pulse can also be detected remotely. The experiment setup is illustrated in Figure 5.10. A small coil (8 turns, ϕ 1 mm , 70 nH) is soldered to the PZT cantilever as an antenna. Another hand-wound coil (100 turns, ϕ 6 mm)

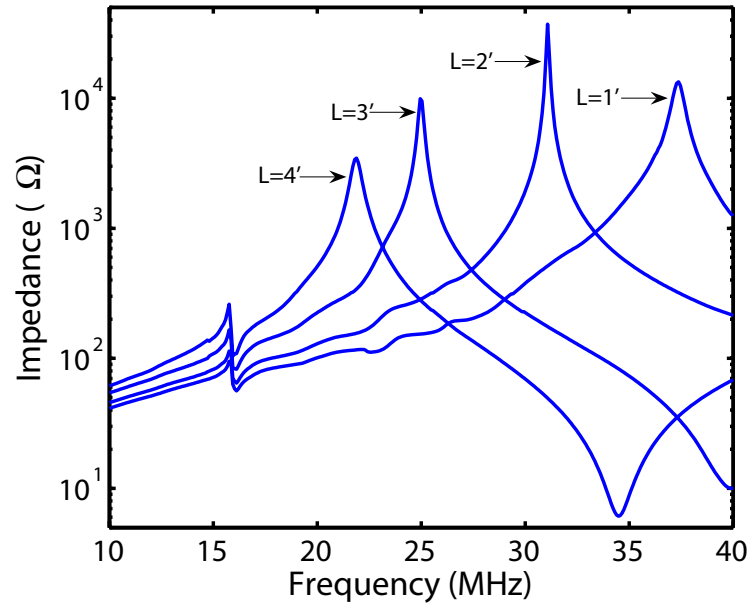


Figure 5.8: The resonance frequency of the system changes with the cable length, which is indicated by L .

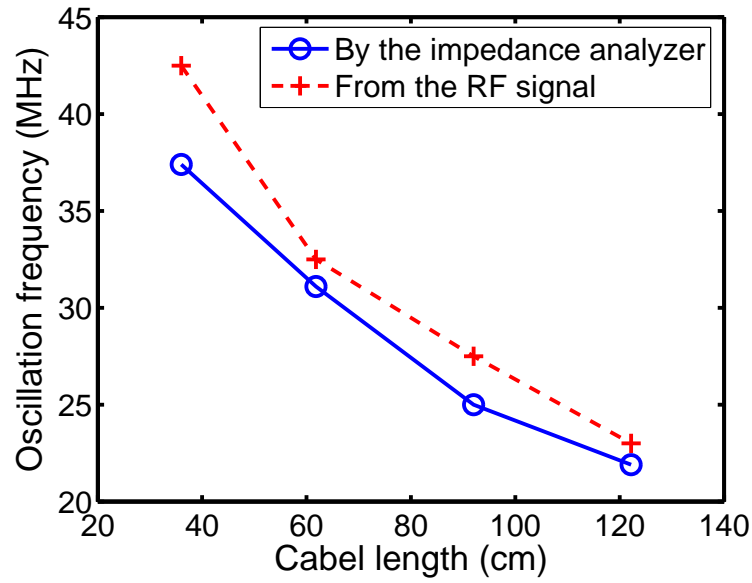


Figure 5.9: The oscillation frequency of the RF pulse also varies as the coaxial cable length changes.

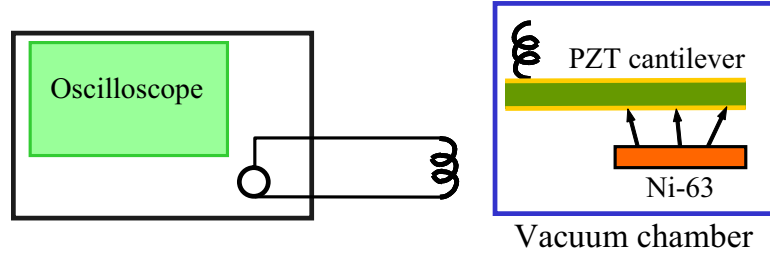


Figure 5.10: The experimental setup for remotely detecting the RF pulse is shown. A small coil (8 turns, ϕ 1 mm, 70 nH) is soldered to the PZT cantilever as an antenna. Another coil (100 turns, ϕ 6 mm, 25 μ H) is connected to the oscilloscope for detection.

with an inductance of 25 μ H, placed outside the vacuum chamber about 0.1 m away from the PZT cantilever, is connected to an oscilloscope to pick up the RF signal. When the PZT touches the source at the end of each reciprocation cycle and jumps back, a signal is detected. Figure 5.11 shows one typical waveform received and the signal frequency is 117.5 MHz. If the cantilever is taken as a quarter wavelength waveguide, since one end is open-circuited and the other end is connected to the antenna for transmission, the resonance frequency is

$$f = \frac{v}{\lambda} = \frac{c/\sqrt{\epsilon_r}}{4L} \quad (5.5)$$

with c the vacuum light speed, $\epsilon_r = 1200$ the relative permittivity and $L = 2$ cm the length of the cantilever. The calculated frequency is 108.3 MHz, which is close to the received signal frequency.

The power received by the oscilloscope can be estimated by

$$P = \frac{CV^2/2}{T_p} \quad (5.6)$$

where C is the oscilloscope capacitance, V is the voltage across it and T_p is the pulse width. For the pulse shown in Figure 5.11 V is 30 mV, T_p is 8.5 ns and C

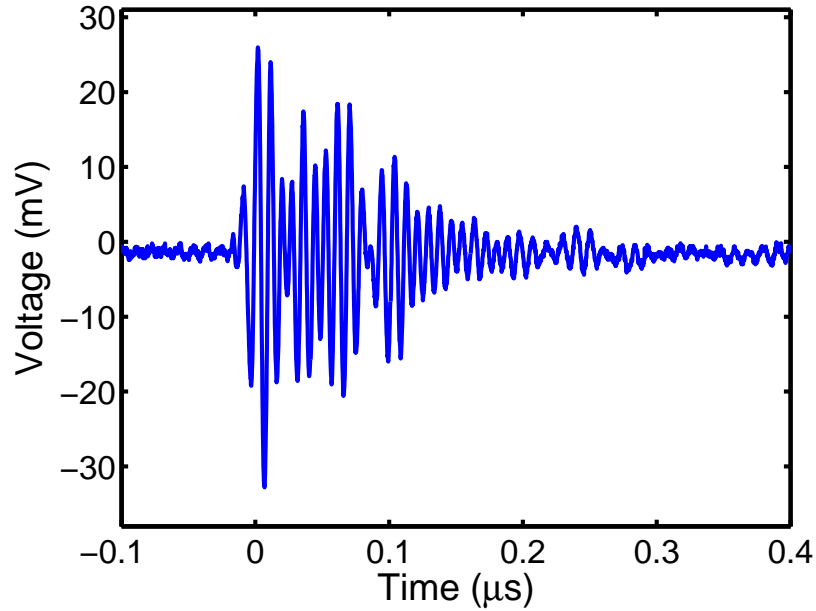


Figure 5.11: A typical RF pulse remotely detected is shown. The signal frequency is 117.5 MHz and the peak-to-peak voltage is 59 mV .

is 13 pF , so the estimated power is 0.69 μW . The power from the radioisotope source is 30 nW , which is estimated as

$$P_s = NE_e \quad (5.7)$$

where N is the activity which is 0.3 mCi for the cantilever and E_e is the average electron energy which is 17 keV . Therefore the cantilever achieves a power amplification of 23 times. Since only the received power by the oscilloscope is counted, the actual power emitted from the cantilever could be much higher. The PZT cantilever, like the cantilever discussed before, integrates the energy from the source over time and releases it in a short time interval to achieve high instantaneous power.

5.3 Polymer Dielectric RF Pulse Generation

To verify that other dielectric materials can also be used to generate RF pulse and also to clarify that the piezoelectric property of the PZT is not involved in the RF pulse generation, ethyl cyanoacrylate (“super glue”) is used as the dielectric material. Two thin copper pieces of the dimensions of $6.5\text{ cm} \times 3.2\text{ mm} \times 50\text{ }\mu\text{m}$ are glued together with the super glue. The super glue thickness is about $160\text{ }\mu\text{m}$ measured optically. The same experiment setup shown in Figure 5.3 is used. As expected a RF pulse is generated and the frequency also changes with the coaxial cable length. Figure 5.12 shows a typical waveform with a 2 feet long cable. Figure 5.13 shows the frequency variance as the cable length changes. The predictions by Equation 5.3 are plotted together and once again they are close to the experimental results.

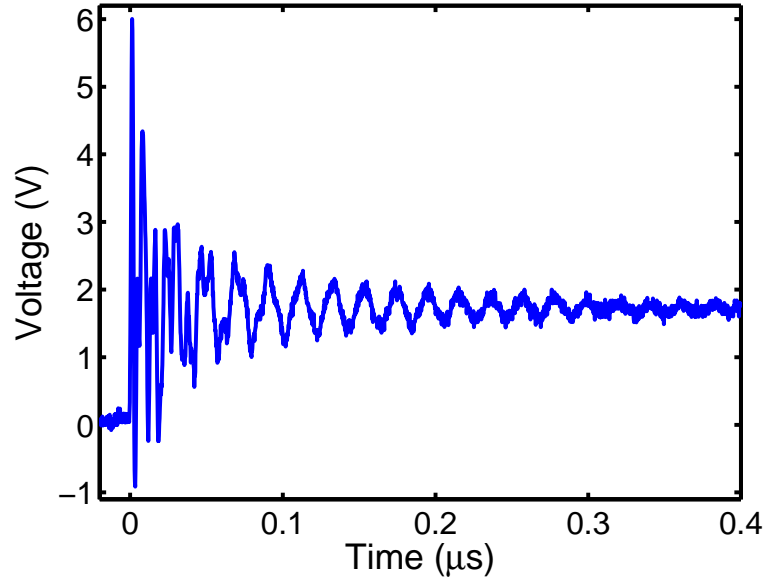


Figure 5.12: A typical RF pulse generated by the ethyl cyanoacrylate cantilever. The initial pulse frequency is 133 MHz and the peak-to-peak voltage is 6.9 V .

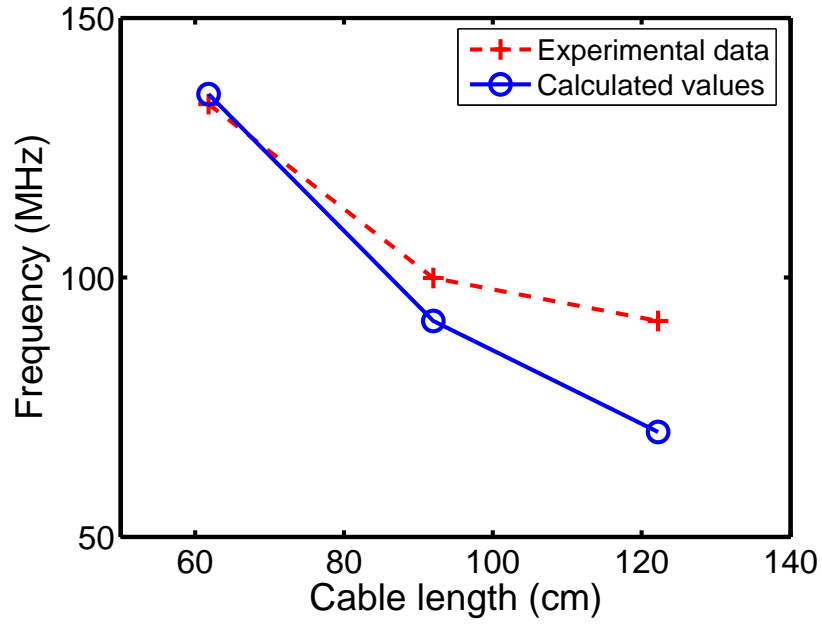


Figure 5.13: The frequency of the RF pulse generated with the ethyl cyanoacrylate cantilever also varies with the coaxial cable length.

5.4 Summary

Radio frequency pulse is generated with a radioisotope-powered PZT cantilever. A simple dielectric waveguide excitation model is used to estimate the signal frequency, which agrees well with the experimental measurement. Ethyl cyanoacrylate is used as the dielectric material to confirm the RF pulse generation and clarify that the piezoelectric property of the PZT is not involved in pulse generation. Besides detection of the RF pulse by directly connecting the PZT cantilever to an oscilloscope, the pulse can also be detected remotely using a RF picking coil.

Chapter 6

Radioactive Piezoelectric Micro Power Generation

The kinetic energy of the emitted charged particles from radioisotopes is converted into mechanical energy with the self-reciprocating cantilever. Although the mechanical movement of the cantilever can be directly used for actuation, converting the kinetic energy into electricity will enable more applications. By utilizing a piezoelectric unimorph the mechanical energy stored in the cantilever can be further converted to electricity. The piezoelectric unimorph supplies the electric load with directly usable voltage while shielding it from the high voltage generated due to direct charging. In this sense, the unimorph works like a transformer.

6.1 Principle of Operation

Figure 6.1 shows a schematic of the radioactive piezoelectric micro power generator. It consists of two parts: a cantilever, made of metal, silicon or any other material with a conductive collector bonded to the free end, and a piezoelectric PZT piece. The PZT is bonded to the non-free end of the cantilever so that it experiences the maximum mechanical stress. The cantilever part is essentially the same as the self-reciprocating cantilever and functions the same way. The collector at the tip of the cantilever collects charges from the radioactive thin film source. At the end of a reciprocation cycle, the cantilever is released from the electrostatic force due to charge neutralization. Since the charge neutralization happens very quickly, the release of the cantilever is a sudden process. The sudden release excites the

mechanical impulse response of the cantilever. The PZT actuated by the vibrations generates AC signals, which can be used to drive a load or further rectified for DC power.

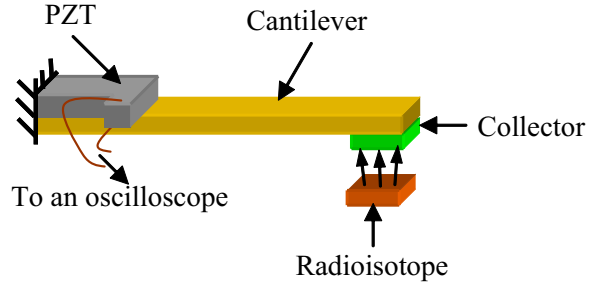


Figure 6.1: A schematic of the PZT unimorph driven by a radioisotope is shown. The two electrodes of the PZT piece are connected to an oscilloscope to measure the output.

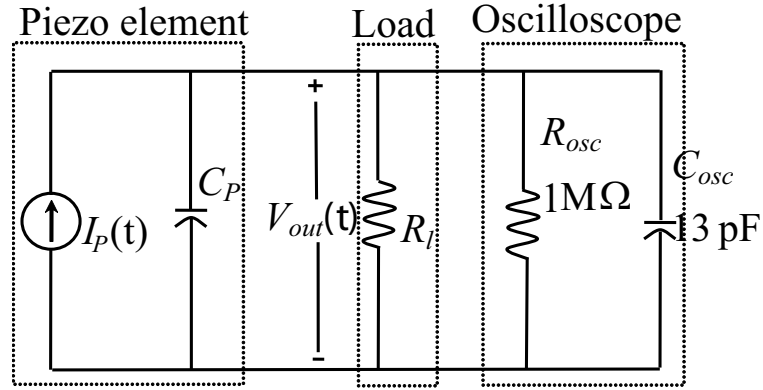


Figure 6.2: The circuit configuration for the characterization of the micro power generator.

6.2 Nuclear to Electrical Conversion Efficiency

The equivalent circuit of the electricity generation part is shown in Figure 6.2. To focus on the characteristics of the power generation, the load is a simple resistor. There are two energy conversion processes involved. One is the conversion of the radiated kinetic energy from the radioactive source into the electromechanical energy stored in the cantilever. The other one is the conversion of the stored electromechanical energy into the electricity by the PZT unimorph. The electromechanical energy stored in the cantilever just before discharge is mainly the mechanical energy due to the bending of the cantilever. Although the PZT is under stress, since it connects to a load and itself also has internal leakage path, the electrical energy stored in the PZT part is minimal. The electromechanical energy available for conversion therefore is:

$$E_{em} = E_m + E_q = \frac{1}{2}kd_0^2 + \frac{Q_p^2}{2C_p} \cong \frac{1}{2}kd_0^2 \quad (6.1)$$

The extracted electrical energy per reciprocation cycle, E_{ext} , across the load resistor R , is calculated as

$$E_{ext} = \int_0^{T_{vib}} \frac{V_{out}^2(t)}{R} dt \quad (6.2)$$

where $V_{out}(t)$ is the output voltage across the load resistor and T_{vib} is the duration for which the vibrations are sustained. Let η_r be the conversion efficiency of the stored electromechanical energy to the radiated kinetic energy and η_{me} the conversion efficiency of the extracted electrical energy to the stored energy.

$$\eta_r = \frac{E_{em}}{E_r} \quad (6.3)$$

$$\eta_{me} = \frac{E_{ext}}{E_{em}} \quad (6.4)$$

The efficiency of the energy conversion η is

$$\eta = \eta_r \eta_{me} = \frac{E_{em}}{E_r} \frac{E_{ext}}{E_{em}} = \frac{E_{ext}}{E_r} \quad (6.5)$$

Modelling the resonant system as a single degree freedom system [57], it can be shown that η_{me} can be maximized to

$$\eta_{me} = \frac{k_{me}}{k_{me} + 2cC_p 2\pi f} \quad (6.6)$$

by using an optimum value of load resistance given by

$$R_{opt} = \frac{1}{2\pi f C_p} \quad (6.7)$$

k_{me} is the mechanical to electrical coupling coefficient depending on the geometry of the cantilever system and the characteristics of the piezoelectric element. C_p is the dielectric capacitance of the piezoelectric element. c is the mechanical damping coefficient and f is the resonance frequency of the cantilever given by [58]

$$f = \frac{\lambda_i^2}{2\pi} \sqrt{\frac{k}{0.23m + m_s}} \quad (6.8)$$

where $\lambda_i = 1.875$ for the fundamental bending mode, m is the mass of the cantilever, m_s is the mass of the collector if exists. The collector mass provides an additional degree of freedom in lowering the resonance frequency to achieve better conversion efficiency without changing the stiffness (k) of the cantilever, which would affect the efficiency. Inspecting Equation 6.6, it can be seen that η_{me} approaches unity in the absence of mechanical damping

$$\eta_{memax} = \eta_{me}|_{c \rightarrow 0} = 1 \quad (6.9)$$

As has been discussed in Chapter 3, Equation 3.24 shows the maximum possible value for η_r is 65%. Therefore, the maximum possible conversion efficiency is

$$\eta_{max} = \eta_{rmax} \eta_{memax} = 0.65 \times 1 \times 100\% = 65\% \quad (6.10)$$

6.3 Devices and Results

Prototype devices have been fabricated to verify the energy conversion principle and to test for the power generation characteristics. The cantilever is made from 100 μm thick silicon wafer. The length and width of the cantilever are defined through laser-cut process with solid-state pulsed ultraviolet laser (model Avia 355-1500 from Coherent) [59]. A 125 μm thick PZT-5H (from Piezo Systems Inc.) is also laser-cut into the size of 5 mm \times 6 mm as the piezoelectric element and bonded with the silicon beam by super glue. At the other end of the cantilever, two layers of 125 μm thick copper sheet with desired size are adhesively bonded to act as both the charge collector and a mass to lower the resonance frequency. The same 1 cm^2 , nominal activity 4 mCi source from IPL is used. A large device with the dimensions of 5 cm \times 5 mm \times 100 μm and a small device of 20 mm \times 2 mm \times 100 μm are fabricated and tested. The collector for the large device is 10 mm \times 5 mm in size and for the small device is 10 mm \times 7.5 mm. The smaller device demonstrates the feasibility of packaging the device in a ceramic package.

A picture of the experiment setup is shown in Figure 6.3. It is very similar to the cantilever reciprocation experiment with the only difference that two wires are soldered to the PZT element to connect to the load. The source is mounted on a linear stage to control the initial distance between the source and the collector of the cantilever. The whole setup is put inside the same vacuum chamber as used in the cantilever reciprocation experiment. The chamber has a glass top and a microscope outside the chamber connected to a CCD camera is used to monitor the movement of the device.

The spring constant (k) of the cantilever is measured by deflecting the beam tip and measuring the generated blocking force using a Chatillon force meter mounted

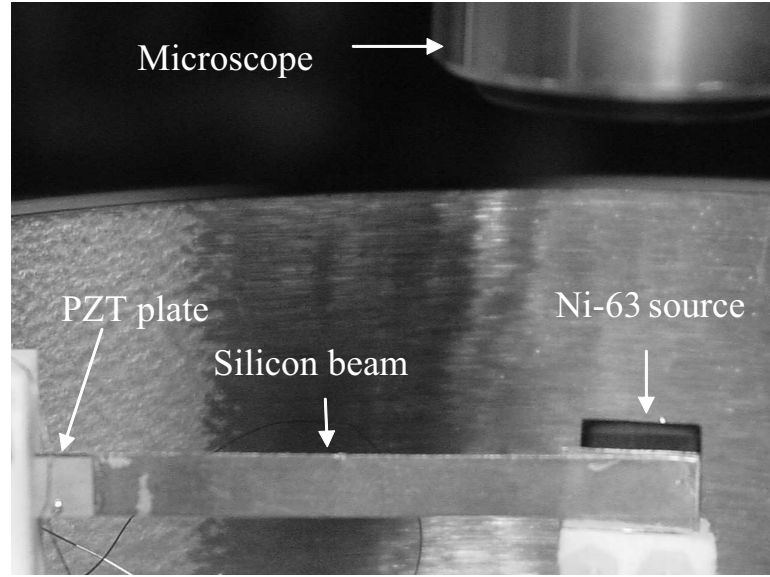


Figure 6.3: A picture of the experimental setup is shown. The cantilever is clamped by two ceramic pieces. The Ni-63 source is mounted on a linear stage for initial gap control. Two wires soldered to the PZT piece provide electrical connection for signal detection. The whole setup is put inside a vacuum chamber with a glass top. A microscope connected to a CCD camera is placed outside the chamber to monitor the device movement.

on a Sutter Instruments Co. MP-285 micro positioner. The measured values of the spring constants are 2.34 N/m and 19.3 N/m for the larger and the smaller beam respectively.

Tests for characterizing the micro power generator are done by positioning the radioisotope source at an initial gap from the collector and monitoring the system through the charge-discharge/release-oscillations cycle. As expected at the end of each reciprocation cycle, the cantilever vibrates and electricity is generated. Figure 6.4 plots the output voltage signal from the piezoelectric element of the larger cantilever at an initial gap of 2 mm . A closeup at 2 s after the initial signal

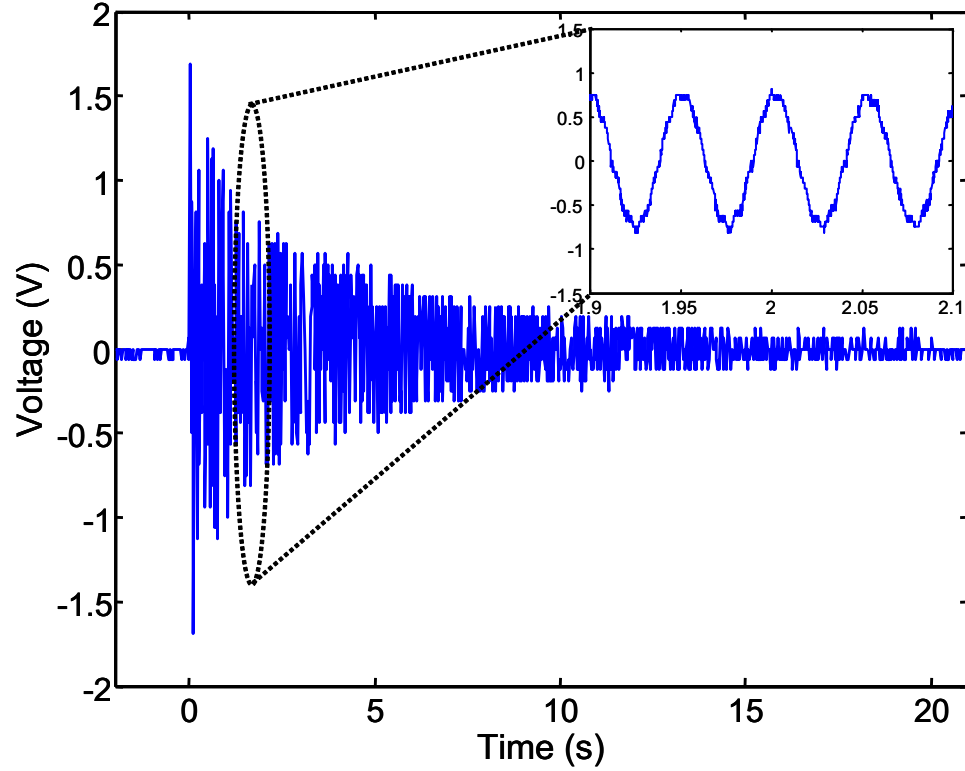


Figure 6.4: Measured output waveform of the micro power generator across $1\text{ M}\Omega$ resistive load is plotted. A closeup at 2 s shows the sinusoidal nature of the AC signal. The maximum peak-to-peak voltage is 3.4 V and the signal frequency is 19.6 Hz .

is shown together to unveil the sinusoidal nature of the AC signal. The frequency of the output is 19.6 Hz , which is also the cantilever vibration frequency.

The reciprocation period measured as a function of the initial gap is plotted in Figure 6.5. The electromechanical model fits well with the experimental data. Unfortunately, air breakdown happens when the initial gap becomes larger than 2 mm . As discussed in Chapter 4 when the cantilever experiences air breakdown the efficiency drops dramatically and the output also decreases. Therefore no further experiments were done for even larger initial gaps.

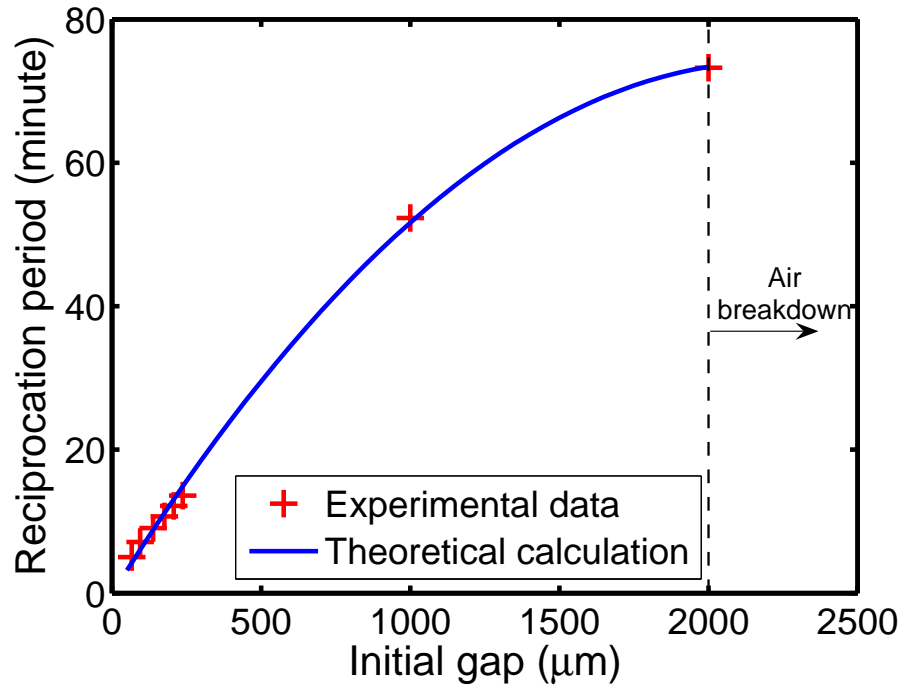


Figure 6.5: The reciprocation period varies as the initial gap changes. The curve is fitted with the electromechanical model. When the initial gap becomes larger than 2 *mm* air breakdown happens.

From the captured output voltage waveform, the modal damping ratio ζ , and the quality factor Q , can be calculated using

$$\zeta = \frac{1}{(t_2 - t_1)2\pi f} \ln\left(\frac{V_{t1}}{V_{t2}}\right) = \frac{1}{2Q} \quad (6.11)$$

where V_{t1} and V_{t2} are the voltage outputs at two instants t_1 and t_2 respectively, and f is the frequency of the oscillation. Figure 6.6 plots the Q -factor of the device for different load resistances. The total extracted electrical energy for different loads at a fixed initial distance of 1 *mm* is plotted together. As expected, both the Q -factor and the energy output peak at R_l of 1 $M\Omega$. From Equation 6.7, and knowing that the capacitance of the PZT element is 8 nF , the optimum value of

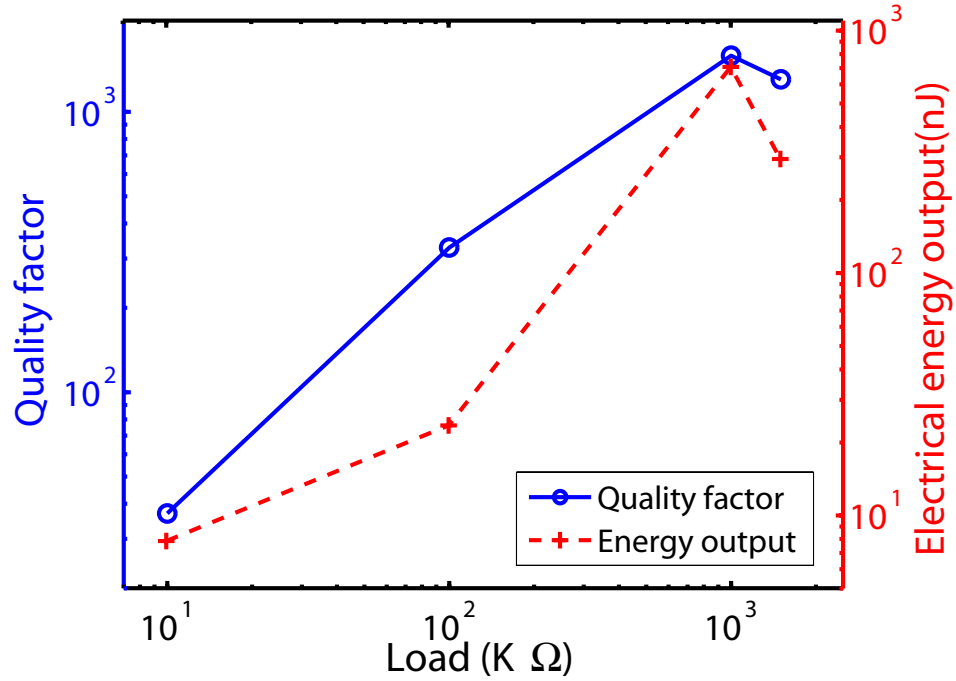


Figure 6.6: The quality factor and the electrical energy output for different load resistances with the same cantilever at a fixed initial gap of 1 *mm* are plotted. As expected, the optimum load resistance is 1 *MΩ*.

R_l is

$$R_{opt} = \frac{1}{2\pi f C_P} = \frac{1}{2\pi \times 19.6 \times 9 \times 10^{-9}} = 1.02 M\Omega \quad (6.12)$$

which is compatible with the experimental result.

The total energy conversion efficiency η and the extracted electrical energy E_{ext} for different values of initial gap with the same load resistance of 1 *MΩ* are plotted in Figure 6.7. As the initial gap increases, both the output energy and efficiency increase. These are expected since both the energy output and the efficiency of the cantilever increase as the initial gap increases, as have been discussed in Chapter 4.

Table 6.1 summarizes the results obtained from the testing of the two devices. Both are connected with optimized load, 1 *MΩ* for the large one and 520 *kΩ* for

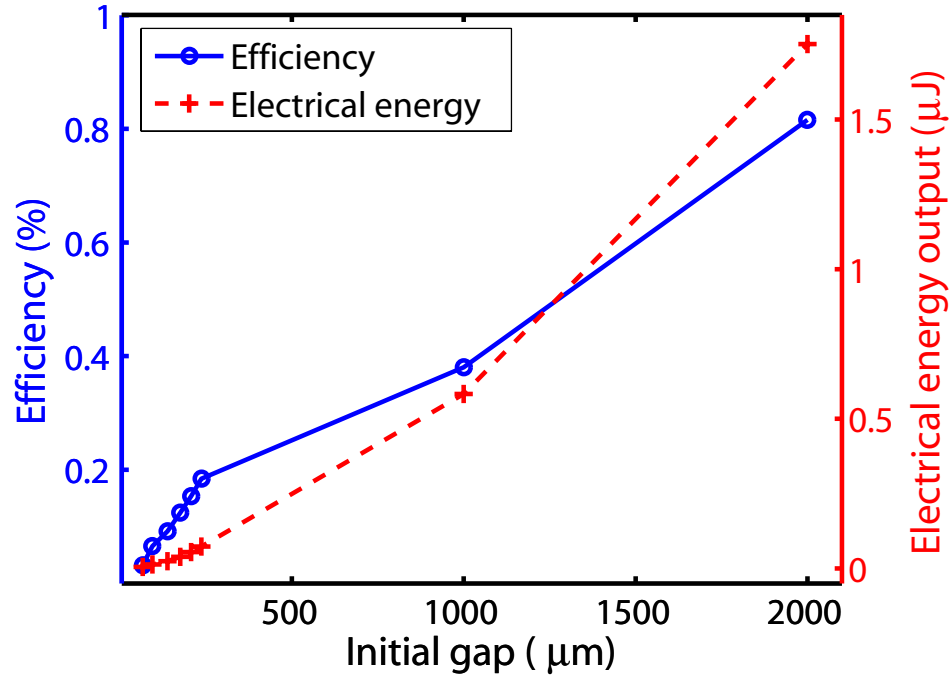


Figure 6.7: As the initial gap increases, both the extracted electrical energy and the total energy conversion efficiency increase.

the small one. The larger device is capable of reaching higher efficiency at a larger gap while the small device gives lower efficiency at a smaller maximum operational gap before air breakdown. Generally, devices with lower stiffness placed at larger gap separations are more efficient.

Table 6.2 compares two devices with the same cantilever and PZT piece but different collectors. One has a collector made of 2 layers of copper piece with a size of $12\text{ mm} \times 7\text{ mm} \times 125\text{ }\mu\text{m}$ while the other one has 4 layers. The load resistance is $1\text{ M}\Omega$ for both devices. As Equation 6.6 predicts the one with a heavier collector has a higher efficiency since its resonance frequency is lower.

Table 6.1: Summary of the test results of the large and the small devices. The large device offers better performance.

Device	d_0	T	Vibration time	Peak voltage	E_{ext}	E_r	η
	(μm)	(<i>minute</i>)	(<i>second</i>)	(V)	(μJ)	(μJ)	(%)
Large	2000	73	20	1.7	1.75	214	0.82
Small	750	146	2	4.2	1.42	640	0.22

Table 6.2: List is the comparison of two devices whose only difference is the mass of the collector. The initial distance is 3 *mm*. The one with a heavier collector has a lower resonance frequency and a higher efficiency.

Collector mass	Resonance frequency	T	Vibration time	E_{ext}	η
	(Hz)	(<i>minute</i>)	(<i>second</i>)	(μJ)	(%)
Large	15.8	137	20	4.44	0.79
Small	38	132	8	2.93	0.54

6.4 Summary

Electricity is generated with a self-reciprocating piezoelectric unimorph powered by a radioisotope. The unimorph vibrates at the end of the reciprocation because of the mechanical impulse excitation, which results from the sudden charge neutralization. The vibrations generate AC output across the PZT element which can be directly used or further rectified to obtain DC output. Two energy conversion processes have been identified. One is from the kinetic energy of the emitted elec-

trons to the electromechanical energy stored in the unimorph and the other one is from the stored energy to the electricity. Therefore, improvement of the energy conversion efficiency of the unimorph involves improving the efficiencies of both processes. Two unimorphs with different dimensions are fabricated and tested.

Chapter 7

Conclusions

In this dissertation, a radioisotope-powered self reciprocating cantilever is presented for micro power generation. The direct charge collection to mechanical actuation is a novel way of harvesting nuclear energy. The cantilever-source structure provides a single platform for mechanical actuation, radio frequency pulse generation and electrical power generation.

7.1 Self-reciprocating Cantilever

A cantilever electrostatically actuated by radioisotope-emitted electrons has been demonstrated. A satisfactory electromechanical model that can be used to optimize the cantilever has been developed. To meet the requirement of either signal modulation or power conversion applications, one can design the cantilever system by choosing different radioisotopes, different materials and dimensions. Minimizing the leakages due to radiation configuration factor, secondary electrons and ionization is important for improving energy conversion efficiency. Scaling the size down to micro scale is feasible, which might enable miniature self-powered autonomous systems. The long half-life of the radioactive source enables the cantilever to be used as an electromechanical transducer for applications requiring long time operation. Furthermore, temperature insensitivity of the charged particle emission might enable extreme high or low temperature operation, which is not possible with chemical batteries.

Radio frequency pulse generation is realized with a dielectric cantilever. The RF pulse comes from the dielectric waveguide mode excitation of the cantilever.

Although the distance of remote detection is small with current experimental setup, larger distance detection is expected with power output improvement with optimized device design and a better receiver. The important fact is that it enables self-powered RF communication. This can be potentially used for wireless sensor nodes where information can be sent out in a self-powered way.

The nuclear energy from a radioisotope is converted into electricity with the piezoelectric micro power generator. There are two conversion processes involved. One is the conversion from the kinetic energy carried by emitted electrons to the electromechanical energy stored in the self-reciprocating cantilever; the other one is this stored electromechanical energy to the electricity with the help a PZT element. The micro power generator provides directly usable voltage and current to the load while shielding it from the high voltage generated from the radioactive source. Optimization of the device includes optimization of the cantilever and optimization of the PZT element.

Combining the mechanical actuation from a self-reciprocating cantilever, the RF pulse generation with a dielectric beam and the electrical output from a piezoelectric micro power generator, a self-powered autonomous system integrating actuation, sensing and wireless communication could be possible. The devices presented therefore have strong potential for wireless sensor nodes where self-powered systems are greatly appreciated. The long time operation enabled by the long half-life of the radioisotope offers a unique advantage over other technologies.

7.2 Future Research

The goal of the radioactive micro power generation is to meet a given energy and power requirement with minimum radioisotope usage. Therefore improvement of

energy conversion efficiency will be the center of efforts. To achieve high efficiency, minimization of leakages is critical. Further investigation of different collector materials to find out the best one for electron collection would be an immediate research topic. Research on minimizing ionization current is very important as a large portion of the leakage comes from it. However for practical applications simply improving the vacuum may not be a choice and other methods are necessary. Therefore it is expected to be difficult to reduce ionization current. Searching for a gas which generates less ionization current can be a starting point. The radiation configuration factor plays an important role at large gaps. Optimized geometric design of the cantilever will also need to be explored.

Currently the peak electrical power is in the range of a few tens of microwatts and lasts a few seconds. If the power level can be improved to a few hundreds of micro watts or even a few milliwatts, many low power electronics can then be powered, and many functions can be realized. So improving the power output is paramount. One way would be to increase the amount of radioisotopes used while keeping the safety precautions easily implemented. Since the number of available electrons from a radioisotope is area dependant rather than volume dependant, investigation of increasing the surface-to-volume ratio for the radioactive source will benefit a compact size system. Another way would be to use different radioisotopes. Tritium has a higher specific activity than Ni-63, while it emits electrons with a smaller average energy. Using tritium as the source may help increase both power output and efficiency. Promethium-147 which has a higher specific activity and higher average electron energy than Ni-63 is also a candidate.

Besides the cantilever design, the PZT element design of the piezoelectric micro power generator also needs to be explored. Research will be on increasing the

mechanical to electrical conversion efficiency. This involves material selection, geometry design, investigation of bonding and mounting technology. The issue of material fatigue could be a concern, especially for long term operation.

Further development of the electromechanical model of the cantilever to include leakages will help to gain more thorough understanding of the cantilever characteristics. The main challenge is to model the ionization current.

For the research of RF pulse generation, a more detailed model of the electrical waveguide system would be necessary in order to design the system to achieve a well defined frequency output. How to increase the signal power and operation time is another task. Further investigation should also look into encoding the desired information in the RF pulse.

Eventually self-powered autonomous systems enabled by the self-reciprocating cantilever are expected to be realized.

Appendix A

Continuous-slowing-down

Approximation Range

Most of the information presented here is from Reference [49]. The tables in Reference [49] list the continuous-slowing-down approximation (CSDA) ranges in many materials for electrons with different initial energies. With the CSDA range, the range of an electron in the material can be calculated as

$$Range = \frac{CSDA\ range}{Density\ of\ the\ material} \quad (A.1)$$

Continuous-slowing-down approximation is a method used to estimate the range of a charged particle inside a given medium. As a charged particle travels inside a medium, it keeps losing its energy until finally it stops. However this loss of energy is not a uniform process. In CSDA, energy loss fluctuations are neglected and charged particles are assumed to lose energy continuously along their tracks, with a mean energy loss per unit pathlength given by the stopping power. The CSDA range, with a unit of g/cm^2 , is evaluated from the expression

$$r_0(E_0 \rightarrow E_f) = \rho \int_{E_f}^{E_0} [S_{col}(E) + S_{rad}(E)]^{-1} dE \quad (A.2)$$

r_0 represents the average pathlength traveled by a charged particle as it slows down from an initial energy, E_0 , to a final energy, E_f . The choice of E_f should in principle be adapted to the purpose for which the range is used.

$S_{col}(E)$ is the *collision stopping power* and $S_{rad}(E)$ is the *radiative stopping power*. The stopping power is the average rate at which the charged particles lose energy at any point along their tracks. For electrons and positrons it is customary

to separate the total stopping power into two components: the collision stopping power (S_{col}) and the radiative stopping power (S_{rad}). S_{col} is the average energy loss per unit pathlength due to inelastic Coulomb collisions with bound atomic electrons of the medium resulting in ionization and excitation. S_{rad} is the average energy loss per unit pathlength due to the emission of bremsstrahlung in the electric field of the atomic nucleus and of the atomic electrons. The reasons to separate the total stopping power into these two components are: first, the methods used for the evaluation of the two components are quite different; second, the energy going into the ionization and excitation of atoms is absorbed in the medium rather close to the particle track, whereas most of the energy lost in the form of bremsstrahlung travels far from the track before being absorbed.

Even though electron stopping powers and ranges are widely used, they are rarely measured and must be obtained from stopping power theory. As mentioned in Reference [49], all the previous (before 1984) tables of stopping power and the one in Reference [49] use the Bethe theory [60, 61, 62] to evaluate collision stopping powers for electrons at energies above 10 *keV*. The energy of 10 *keV* is a commonly accepted lower limit for the applicability of the theory. One important quantity in the stopping power formula, not contained in Bethe's original theory, is the density-effect correction. The tables in Reference [49] use the method of Sternheimer [63] for evaluation of the density-effect correction. The radiative stopping power for electrons is calculated with theoretical bremsstrahlung cross sections.

The stopping powers needed for the evaluation of r_0 in Equation A.2 are available from the Bethe theory only down to some intermediate energy E_i , and the part of the integral from $E = E_i$ to T_f must be obtained by an approximation. Fortunately this residual range is relatively small so that a simple approximation

is sufficient. Reference [49] follows Nelms [64] in assuming that the integrand $[S_{col}(E) + S_{rad}(E)]^{-1}$ in Equation A.2 is zero at $E = 0$ and can be interpolated linearly to its value at $E = E_i$. The range is then given by

$$r_0(E_0 \rightarrow E_f) = r_0(E_0 \rightarrow E_i) + \rho[S_{col}(E_i) + S_{rad}(E_i)]^{-1} \int_{E_f}^{E_i} (E/E_i) dE \quad (\text{A.3})$$

where the first term is calculated using Equation A.2, and the second term is the residual range. The range tables in Reference [49] give results obtained with $E_i = 1 \text{ keV}$ and $E_f = 0$.

Appendix B

Radiation Configuration Factor for Two Parallel Rectangles

The equation used to calculate the radiation configuration factor for two parallel rectangles is presented for convenience. The equation is from Ref. [52], which provides a very complete catalog of analytical relations and graphs for radiation configuration factors.

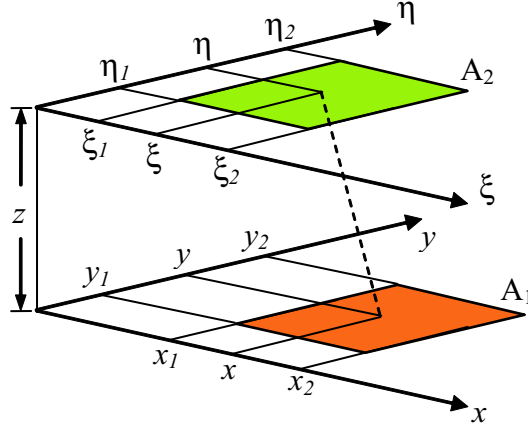


Figure B.1: Shown is the configuration of two parallel rectangles.

As shown in Figure B.1, two rectangles are in parallel planes where all rectangle boundaries are parallel or perpendicular to x or ξ axes. The symbols to be used in the equation are defined as:

$$X = x/z$$

$$Y = y/z$$

$$N = \eta/z$$

$$S = \xi/z$$

$$\alpha_{li} = S_l - X_i$$

$$\beta_{kj} = N_k - Y_j$$

where z is the distance between two parallel planes. The equation for the radiation configuration factor is

$$F_{12} = \frac{1}{(X_2 - X_1)(Y_2 - Y_1)} \sum_{l=1}^2 \sum_{k=1}^2 \sum_{j=1}^2 \sum_{i=1}^2 \left[(-1)^{i+j+k+l} G(\alpha_{li}, \beta_{kj}) \right] \quad (\text{B.1})$$

where

$$\begin{aligned} G(\alpha_{li}, \beta_{kj}) = & \frac{1}{2\pi} \left\{ \alpha_{li}(1 + \beta_{kj}^2)^{1/2} \tan^{-1} \left[\frac{\alpha_{li}}{(1 + \beta_{kj}^2)^{1/2}} \right] - \beta_{kj} \tan^{-1}(\beta_{kj}) \right. \\ & + (1 + \alpha_{li}^2)^{1/2} \beta_{kj} \tan^{-1} \left[\frac{\beta_{kj}}{(1 + \alpha_{li}^2)^{1/2}} \right] - \alpha_{li}^2 \ln(\alpha_{li}) \\ & \left. + \frac{1}{2} \ln(1 + \beta_{kj}^2) - \frac{1}{2} \ln(1 + \alpha_{li}^2 + \beta_{kj}^2) \right\} \end{aligned}$$

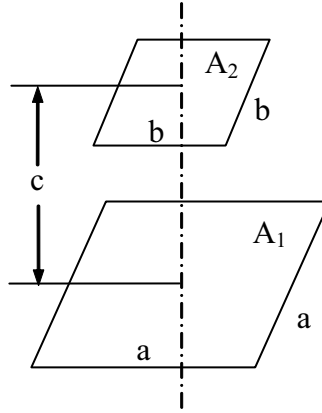


Figure B.2: Shown is the configuration of two coaxial parallel squares.

For two coaxial parallel squares as shown in Figure B.2, which is a special case of two parallel rectangles, a simpler equation can be used:

$$F_{12} = \frac{1}{\pi A^2} \left\{ \ln \frac{[A^2(1 + B^2) + 2]^2}{(Y^2 + 2)(X^2 + 2)} \right\}$$

$$\begin{aligned}
& +(Y^2 + 4)^{1/2} \left[Y \tan^{-1} \frac{Y}{(Y^2 + 4)^{1/2}} - X \tan^{-1} \frac{X}{(Y^2 + 4)^{1/2}} \right] \\
& +(X^2 + 4)^{1/2} \left[X \tan^{-1} \frac{X}{(X^2 + 4)^{1/2}} - Y \tan^{-1} \frac{Y}{(X^2 + 4)^{1/2}} \right] \Big\} \quad (\text{B.2})
\end{aligned}$$

where $A = a/c$, $B = b/a$, $X = A(1 + B)$ and $Y = A(1 - B)$.

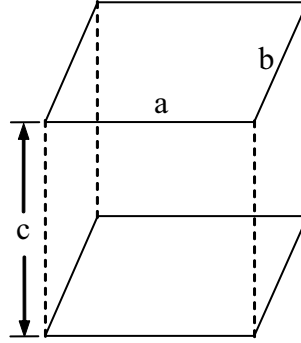


Figure B.3: Shown is the configuration of two identical rectangles directly opposing to each other.

For another special case where two identical rectangles are directly opposing to each other as shown in Figure B.3, the radiation configuration factor can be calculated as:

$$\begin{aligned}
F_{12} = & \frac{2}{\pi XY} \left\{ \ln \left[\frac{(1 + X^2)(1 + Y^2)}{1 + X^2 + Y^2} \right]^{1/2} \right. \\
& + X(1 + Y^2)^{1/2} \tan^{-1} \frac{X}{(1 + Y^2)^{1/2}} \\
& \left. + Y(1 + X^2)^{1/2} \tan^{-1} \frac{Y}{(1 + X^2)^{1/2}} - X \tan^{-1} X - Y \tan^{-1} Y \right\} \quad (\text{B.3})
\end{aligned}$$

where $X = a/c$ and $Y = b/c$.

BIBLIOGRAPHY

- [1] D. Linden and T. B. Reddy, *Handbook of Batteries*, McGraw-Hill, 3rd ed., 2002.
- [2] N. Dudney and B. Neudecker, “Solid State Thin-film Lithium Battery Systems”, *Current Opinion in Solid State and Materials Science*, vol. 4(5), pp. 479–482, Oct. 1999.
- [3] J. L. Souquet and M. Duclot, “Thin Film Lithium Batteries”, *Solid State Ionics*, vol. 148(3-4), pp. 375–379, Jun. 2002.
- [4] J. Bates, N. Dudney, B. Neudecker, A. Ueda, and C. Evans, “Thin-film Lithium and Lithium-ion Batteries”, *Solid State Ionics*, vol. 135(1-4), pp. 33–45, Nov. 2000.
- [5] N. Dudney, “Solid-state Thin-film Rechargeable Batteries”, *Materials Science and Engineering B*, vol. 116(3), pp. 245–249, Feb. 2005.
- [6] C. K. Dyer, “Fuel Cells and Portable Electronics”, *Digest of Technical Papers, 2004 IEEE Symposium on VLSI Circuits*, pp. 124–127, Jun. 2004.
- [7] S. Roundy, D. Steingart, L. Frechette, P. Wright, and J. Rabaey, “Power Sources for Wireless Sensor Networks”, *Proceedings of the First European Workshop on Wireless Sensor Networks, EWSN 2004*, pp. 1–17, Jan. 2004.
- [8] I. EG&G Technical Services and S. A. I. Corporation, *Fuel Cell Handbook*, U.S. Dept. of Energy, National Energy Technology Laboratory, 6th ed., 2002.
- [9] J. D. Holladay, E. O. Jones, M. Phelps, and J. Hu, “High-efficiency Microscale Power Using a Fuel Processor and Fuel Cell”, *Proceedings of the SPIE, MEMS Components and Applications for Industry, Automobiles, Aerospace, and Communication*, vol. 4559, pp. 148–156, 2001.
- [10] A. V. Pattekar and M. V. Kothare, “A Microreactor for Hydrogen Production in Micro Fuel Cell Applications”, *Journal of Microelectromechanical Systems*, vol. 13(1), pp. 7–18, Feb. 2004.
- [11] T. J. Yen, N. Fang, X. Zhang, G. Q. Lu, and C. Y. Wang, “A Micro Methanol Fuel Cell Operating at Near Room Temperature”, *Applied Physics Letters*, vol. 83(19), pp. 4056–4058, Nov. 2003.
- [12] J. Wainright, R. Savinell, C. Liu, and M. Litt, “Microfabricated Fuel Cells”, *Electrochimica Acta*, vol. 48, pp. 2869–2877, 2003.
- [13] R. Hahn, S. Wagner, A. Schmitz, and H. Reichl, “Development of a Planar Micro Fuel Cell with Thin Film and Micro Patterning Technologies”, *Journal of Power Sources*, vol. 131, pp. 73–78, 2004.

- [14] A. Blum, T. Duvdevani, M. Philosoph, N. Rudoy, and E. Peled, "Water-neutral Micro Direct-methanol Fuel Cell (DMFC) for Portable Applications", *Journal of Power Sources*, vol. 117, pp. 22–25, 2003.
- [15] C. Rice, S. Ha, R. I. Masel, P. Waszczuk, A. Wieckowski, and T. Barnard, "Direct Formic Acid Fuel Cells", *Journal of Power Sources*, vol. 111, pp. 83–89, 2002.
- [16] X. Chen, N. J. Wu, L. Smith, and A. Ignatiev, "Thin-film Heterostructure Solid Oxide Fuel Cells", *Applied Physics Letters*, vol. 84(14), pp. 2700–2702, Apr. 2004.
- [17] A. H. Epstein and S. D. Senturia, "Macro Power from Micro Machinery", *Science*, vol. 276, p. 1211, May 1997.
- [18] A. Mehar, X. Zhang, A. A. Ayón, I. A. Waitz, M. A. Schmit, and C. M. Spadaccini, "A Six-Wafer Combustion System for a Silicon Micro Gas Turbine Engine", *Journal of Microelectromechanical systems*, vol. 9(4), pp. 517–526, Dec. 2000.
- [19] M. A. Schmidt, "Portable MEMS Power Sources", *Digest of Technical Papers, 2003 IEEE International Solid-State Circuits Conference*, vol. 1, pp. 394–395, 2003.
- [20] K. Fu, A. Knobloch, F. Martinez, D. Walther, C. Fernandez-Pello, A. Pisano, D. Liepmann, K. Miyaska, and K. Maruta, "Design and Experimental Results of Small-Scale Rotary Engines", *Micro-Electro-Mechanical Systems (MEMS), 2001 ASME International Mechanical Engineering Congress and Exposition*, pp. 867–873, Nov. 2001.
- [21] A. C. Fernandez-Pello, A. Pisano, K. Fu, D. Walther, A. Knobloch, F. Martinez, M. Senesky, C. Stoldt, R. Maboudian, S. Sanders, and D. Liepmann, "MEMS Rotary Engine Power System", *Transactions of the Institute of Electrical Engineers of Japan, Part E*, vol. 123-E(9), pp. 326–330, Sep. 2003.
- [22] T. Toriyama, S. Sugiyama, and K. Hashimoto, "Design of a Resonant Micro Reciprocating Engine for Power Generation", *Digest of Technical Papers, Transducers '03, The 12th International Conference on Solid-State Sensors, Actuators and Microsystems*, vol. 2, pp. 1303–1306, Jun. 2003.
- [23] S. Whalen, M. Thompson, D. Bahr, C. Richards, and R. Richards, "Design, Fabrication and Testing of the P^3 Micro Heat Engine", *Sensors and Actuators A*, vol. 104, pp. 290–298, 2003.
- [24] S. B. Schaevitz, A. J. Franz, K. F. Jensen, and M. A. Schmidt, "A Combustion-Based MEMS Thermoelectric Power Generator", *Digest of Technical Papers, Transducers '01, The 11th International Conference on Solid-State Sensors, Actuators and Microsystems*, vol. 1, pp. 30–33, Jun. 2001.

- [25] C. Zhang, K. Najafi, L. P. Bernal, and P. D. Washabaugh, "An Integrated Combustor-Thermoelectric Micro Power Generator", *Digest of Technical Papers, Transducers '01, The 11th International Conference on Solid-State Sensors, Actuators and Microsystems*, vol. 1, pp. 34–37, Jun. 2001.
- [26] C. Zhang, K. Najafi, L. P. Bernal, and P. D. Washabaugh, "Micro Combustion-Thermionic Power Generation: Feasibility, Design and Initial Results", *Digest of Technical Papers, Transducers '03, The 12th International Conference on Solid-State Sensors, Actuators and Microsystems*, vol. 1, pp. 40–44, Jun. 2003.
- [27] W. M. Yang, S. K. Chou, C. Shu, Z. W. Li, and H. Xue, "Research on Micro-Thermophotovoltaic Power Generators", *Solar Energy Materials & Solar Cells*, vol. 80, pp. 95–104, 2003.
- [28] W. M. Yang, S. K. Chou, C. Shu, Z. W. Li, and H. Xue, "A Prototype Microthermophotovoltaic Power Generator", *Applied Physics Letter*, vol. 84(19), pp. 3864–3866, 2004.
- [29] A. C. Fernandez-Pello, "Micropower Generation Using Combustion: Issues and Approaches", *Proceedings of the Combustion Institute*, vol. 29, pp. 883–899, 2002.
- [30] C. M. Spadaccini, A. Mehra, J. Lee, X. Zhang, S. Lukachko, and I. A. Waitz, "High Power Density Silicon Combustion Systems for Micro Gas Turbine Engines", *Journal of Engineering for Gas Turbines and Power*, vol. 125, pp. 709–719, Jul. 2003.
- [31] B. Atwood, B. Warneke, and K. S. J. Pister, "Preliminary Circuits for Smart Dust", *2000 Southwest Symposium on Mixed-Signal Design*, pp. 87–92, IEEE, Piscataway, NJ, USA, 2000.
- [32] M. Yamaguchi, T. Takamoto, A. Khan, M. Imaizumi, S. Matsuda, and N. J. Ekins-Daukes, "Super-high-efficiency Multi-junction Solar Cells", *Progress in Photovoltaics: Research and Applications*, vol. 13(2), pp. 125–132, Mar. 2005.
- [33] M. Mizuno and D. G. Chetwynd, "Investigation of a Resonance Microgenerator", *Journal of Micromechanics and Microengineering*, vol. 13, pp. 209–216, 2003.
- [34] S. Meninger, J. O. Mur-Miranda, R. Amirtharajah, A. P. Chandrakasan, and J. H. Lang, "Vibration-to-Electric Energy Conversion", *IEEE Transactions on Very Large Scale Integrating (VLSI) Systems*, vol. 9(1), pp. 64–76, Feb. 2001.
- [35] C. B. Williams and R. B. Yates, "Analysis of a Micro-Electric Generator for Microsystems", *Sensors and Actuators A*, vol. 52, pp. 8–11, 1996.

- [36] H. Kulah and K. Najafi, "An Electromagnetic Micro Power Generator for Low-Frequency Environmental Vibrations", *17th IEEE International Conference on Micro Electro Mechanical Systems, MEMS 2004 Technical Digest*, pp. 237–240, Maastricht, Netherlands, 2004.
- [37] K. B. Lam, E. Johnson, and L. Lin, "A Bio-Solar Cell Powered by Sub-Cellular Plant Photosystems", *17th IEEE International Conference on Micro Electro Mechanical Systems, MEMS 2004 Technical Digest*, pp. 237–240, Maastricht, Netherlands, 2004.
- [38] G. Harder, *Pocket Guide for Radiological Management*, Perma-Fix Environmental Services, 1999.
- [39] W. R. Corliss and D. G. Harvey, *Radioisotopic Power Generation*, Prentice-Hall, Inc., Englewood Cliffs, New Jersey, 1964.
- [40] M. G. Bowler, *Nuclear Physics*, chap. 3-5, Pergamon Press, 1973.
- [41] B. Gross and P. V. Murphy, "Currents from Gammas Make Detectors and Batteries", *Nucleonics*, vol. 19, p. 86, 1961.
- [42] J. H. Coleman, "Radioisotopic High-Potential, Low-Current Sources", *Nucleonics*, vol. 11(12), pp. 42–45, Dec. 1953.
- [43] E.G.Linder and S. Christian, "The Use of Radioactive Material for the Generation of High Voltage", *Journal of Applied Physics*, vol. 23(11), pp. 1213–1216, Nov. 1952.
- [44] J. Braun, L. Fermvik, and Å. Stenback, "Theory and Performance of a Tritium Battery for the Microwatt Range", *Journal of Physics, E*, vol. 6, pp. 727–731, Mar. 1973.
- [45] P.Pappaport, J. J. Loferski, and E. G. Linder, "The Electron-Voltaic Effect in Germanium and Silicon p-n Junctions", *Nucleonics*, vol. 11(12), pp. 100–128, Mar. 1955.
- [46] P.E.Ohmart, "A Method of Producing an Electric Current from Radioactivity", *Journal of Applied Physics*, vol. 22, pp. 1504–1505, 1973.
- [47] H. G. J. Moseley and J. Harling, "The Attainment of High Potentials by the Use of Radium", *Proceedings of Royal Society A*, vol. 88, p. 471, 1913.
- [48] A. Thomas, "Nuclear Batteries: Types and Possible Uses", *Nucleonics*, vol. 13(11), pp. 129–133, Nov. 1955.
- [49] I. C. on Radiation Units and Measurements, *Stopping Powers for Electrons and Positrons*, Library of Congress Cataloging in Publication Data, 1984.

- [50] U. of Wisconsin-Madison Safety Department, *Radiation Safety for Radiation Workers*, p. 10, University of Wisconsin System, 1999.
- [51] J. I. Seeger and B. E. Boser, “Charge Control of Parallel-Plate, Electrostatic Actuators and the Tip-In Instability”, *Journal of Microelectromechanical Systems*, vol. 12(5), pp. 656–671, Oct. 2003.
- [52] J. R. Howell, *A Catalog of Radiation Configuration Factors*, pp. 2–3, McGraw-Hill Book Company, New York, 1982.
- [53] H. Bruining, *Physics and Applications of Secondary Electron Emission*, Pergamon Press, 1954.
- [54] <http://physics.nist.gov/PhysRefData/Ionization/index.html>, *Electron Impact Cross Sections for Ionization and Excitation*, National Institute of Standards and Technology, 2005.
- [55] A. V. Hippel, *Conduction and Breakdown of Gases*, in *Molecular Science and Molecular Engineering*, chap. 3, p. 45, The Technology Press of MIT and John Wiley & Sons, Inc., 1959.
- [56] S. Ramo, J. R. Whinnery, and T. V. Duzer, *Fields and Waves in Communication Electronics*, chap. 5, pp. 210–69, John Wiley & Sons, 2nd ed., 1984.
- [57] F. Lu, H. P. Lee, and S. P. Lim, “Modeling and Analysis of Micro Piezoelectric Power Generators for Micro-electromechanical-systems Applications”, *Smart Materials Structure*, vol. 13, pp. 57–63, 2004.
- [58] W. C. Young, *Roark’s Formulas for Stress and Strain*, McGraw Hill, 1989.
- [59] R. Duggirala and A. Lal, “A Pyroelectric-Piezoelectric Valve for Integrated Microfluidics”, *Digest of Technical Papers, Transducers’03, The 12th International Conference on Solid-State Sensors, Actuators and Microsystems*, vol. 2, pp. 1554–1557, 2003.
- [60] H. Bethe, “Zur Theories des Durchgangs schneller Korpuskularstrahlen durch Materie”, *Annals of Physics*, vol. 5, p. 325, 1930.
- [61] H. Bethe, “Bremsformel für Elektronen relativistischer Geschwindigkeit”, *Zeitschrift für Physik*, vol. 76, p. 293, 1932.
- [62] H. Bethe, “BQuantenmechanik der Ein-und Zwei-Elektronenprobleme”, *Handbuch de Physik*, vol. 24, p. 273, 1933.
- [63] R. M. Sternheimer, “The Density Effect for the Ionization Loss in Various Materials”, *Physical Review*, vol. 88, p. 851, 1952.
- [64] A. T. Nelms, “Energy Loss and Range of Electrons and Positrons”, *National Bureau of Standards Circular 577*, 1956.